**FOREIGN
BROADCAST
INFORMATION
SERVICE**

JPRS Report

Science & Technology

Japan

19980630 114

SCIENCE & TECHNOLOGY

JAPAN

CONTENTS

ADVANCED MATERIALS

LASERS, SENSORS, OPTICS

Sintering of Polycrystalline AlN by Self-Propagating Reaction

[Authors: Kou Min, Takeshi Shiono, Toshihiko Nishida, and Tomozo Nishikawa, Kyoto Institute of Technology]

[Text] Introduction: As a material possessing excellent electric properties and high thermal conductivity, AlN is becoming popular. However, since AlN is a difficult ceramic to sinter, temperatures higher than 1700°C are required to fabricate sintered products of AlN. It is important to lower this sintering temperature for AlN to become widely used. At present, additives are used in such attempts. In this work, we used self-propagating reaction sintering (SPRS), in which the synthesis and sintering of AlN occurred simultaneously using the reaction heat generated when a metallic Al powder forms a nitride. Using this method, we attempted to fire sintered AlN products at low temperatures, evaluate these products, and to evaluate the SPRS method.

Experiment: As the raw material powder, we used a mixture of 30--70 weight percent AlN powder with commercial, high-purity Al powder. These two powders were mixed for 20 hours in a dry ball mill. This raw material powder was molded under the required pressure, its temperature was allowed to rise to 800°C in a N_2 gas flow, and the reaction took place for 1--4 hours while the product was fired. To study the effects of molding pressure on the properties of sintered products, molding was performed under a pressure of 300--1900 kgf/cm^2. To evaluate the sintered products, their density and Vickers hardness were measured, and the rate of conversion from Al to AlN as functions of the molding pressure and Al composition was determined by x-ray diffraction.

Results: The rate of conversion from the metallic Al to AlN decreased as the molding pressure increased. However, when the Al content was under 35 weight percent, the sintered products had an almost pure AlN composition even at high molding pressures. In Fig. 1, we show the relative density of the AlN sintered products, which had 100 percent conversion rates, for different compositions. For every composition used, the relative density of sintered products increased as the molding pressure rose. This increase in density was rapid when the molding pressure was low, and slow when the molding pressure was high. At each molding pressure level, no clear relationship was found

this sol by drawing. These gel fibers did not dissolve in solvents and maintained their shape even after firing, indicating the existence of the —Al-O- bond. The change in XRD caused by firing is shown in Fig. 1. Transitions from the amorphous phase to the gamma- and alpha-Al_2O_3 phases were visible.

We obtained similar gel fibers when we used ethyl acetoacetate as a modifier, but their firing behavior was very different, switching from the amorphous phase to the alpha-Al_2O_3 phase near 900°C.

Fig. 1. Changes in XRD resulting from firing.
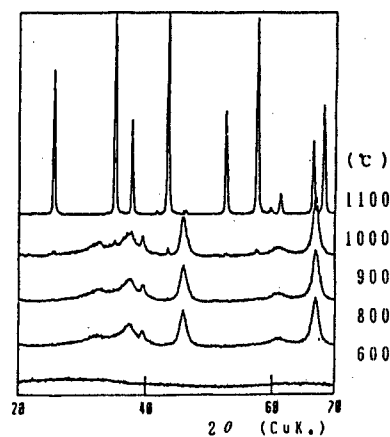
References

1. S. Sakka, 4th Intnl. Sol-Gel Workshop (1987).
2. D. C. Bradley et al., "Metal Alkoxides," (Academic Press, 1978), pp. 149--298.

Preparation of Viscous Sol from Aluminum Alkoxide

[Authors: Hideyuki Ikoma, Masahiro Sekine, and Yoshitaka Nomiya, Colloid
Research Institute]

[Text] 1. Introduction: Sol-gel methods that use metal alkoxides as raw
materials have several advantages, ease of shaping products being one of them.
Many examples utilizing these advantages have been reported[1] on Si-based
products, where a viscous sol is spun to fabricate SiO_2-based fibers. On the
other hand, microparticles are precipitated when other metal alkoxides are
hydrolyzed, and few examples of utilizing the advantage in shaping have been
reported. In our study, we prepared a viscous sol that enabled us to draw
fibers by hydrolyzing products that resulted from the reaction between
aluminum alkoxide and active hydrogen.[2] We examined the possibility of
fabricating alumina fibers.

2. Experiment: We reacted $Al(OBu^s)_3$ with various compounds that contain
active hydrogen (modifiers) in s-BuOH at room temperature for the required
duration, and we hydrolyzed the products using either an H_2O/s-BuOH solution
or moisture in the air. As we removed the solvent by distillation, we
obtained a transparent viscous solution. A glass rod from this solution was
used to draw alumina precursor fibers. This sintering process was also
examined using DTA and XRD.

3. Results and Discussion: To obtain a precursor fiber using a sol-gel
method, it is necessary to prepare a sol that (1) obeys the Newtonian flow
with an appropriate viscosity,[1] and (2) maintains the fiber shape immediately
after drawing by forming a gel. Acetic acid and ethylene glycol were
difficult to use as modifiers because their reaction products had low
solubility. Also, when monoethanolamine or acetylacetone was used, hydrolysis
was unstable, white precipitates formed, and we were unable to prepare a
viscous sol. The first condition mentioned above was satisfied when one mole
of $Al(OBu^s)_3$ was used with one mole of triethanolamine; we could then draw
fibers. However, gelling after drawing was too slow to obtain gel fibers. We
obtained a transparent and viscous sol when we distilled the solvent away from
a mixture of one mole of $Al(OBu^s)_3$ and 1/3 mole of triethanolamine and
hydrolyzed this mixture with one mole of water. We fabricated gel fibers from

between the relative density and Al composition. The diameters of the crystalline particles of the sintered products were approximately 1--3 microns; the diameters grew smaller at higher molding pressures.

Fig. 1. Relationship between the relative density and the molding pressure.

4
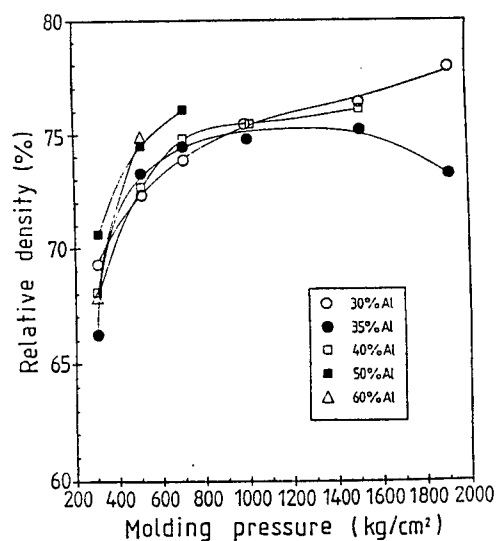
Fabrication of Superconducting YBCO Fibers by Sol-Gel Method

[Authors: Tetsu Umeda, Hiromitsu Kozuka and Sumio Sakka, Institute for Chemical Research, Kyoto University]

[Text] 1. <u>Introduction</u>: Many methods, such as drawing a wire at high temperatures from powder packed in a metal pipe, are being proposed to fabricate wires from the high-temperature superconducting material $YBa_2Cu_3O_x$. In this study, we used a sol-gel method and fired superconducting fibers after they were spun as gel fibers, utilizing the fact that fibers can be drawn from a sol (see Fig. 1). Then, the microstructure and superconducting properties of these fibers were confirmed.

2. <u>Experiment</u> Yttrium acetate, $Y(CH_3COO)_3 \cdot 4H_2O$; barium acetate, $Ba(CH_3COO)_2$; and copper acetate, $Cu(CH_3COO)_2$, were measured by a balance in a 1:2:3 molar ratio, and then dissolved in water to obtain a concentration of 3.8 weight percent equivalent of $YBa_2Cu_3O_7$. The pH value of the solution was adjusted by adding ammonia water. This aqueous solution was left in a dryer at 60°C to raise its viscosity and gel fibers were spun from a sol just before it gelled. These fibers were then fired to form ceramic fibers. Microstructures of the gel and ceramic fibers were observed using an SEM, their precipitation crystals were identified using x rays, their compositions were analyzed using ICP, and their electric conductivity was measured using the four-terminal method.

3. <u>Results</u>: While the gel fibers had smooth surfaces, [the existence of] microcrystalline particles on the ceramic fibers was confirmed. When the gel fibers were fired, they bubbled near 200°C and caused cavities in the ceramic fibers (Fig. 2). Using ICP analysis (Y:Ba:Cu = 1.0:2.1:2.9) and x-ray diffraction, we confirmed that the crystals were rhombic crystals of $YBa_2Cu_3O_x$. The electric resistance measured by the direct-current, four-terminal method is shown in Fig. 3. The T_c (onset) was 94 K and the T_c (end) was 62.2 K. The bulks formed by the sol-gel method have critical temperatures in the 90 K level, which implies that [the critical temperatures of] the fibers can be improved. In the future, we will need to suppress the bubbling that causes cavities in order to increase the mechanical strength [of the fibers]; it will also be desirable to examine the control of atmospheres

during firing in order to raise the critical temperature.
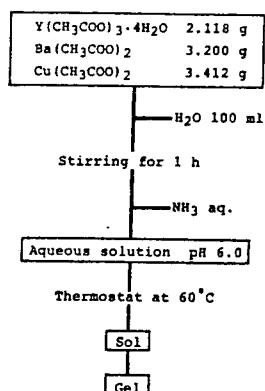
Fig. 1. Method to form a gel.

Fig. 2. SEM image of a fired fiber.
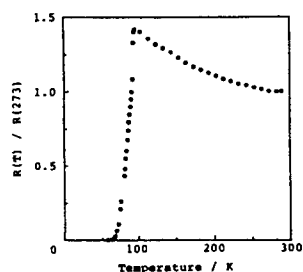
Fig. 3. Temperature-resistance curve
of fired fibers.

Beta-Si_3N_4 Whiskers, Their Composite Materials

43067063d Tokyo FY88 NIPPON SERAMIKKUSU KYOKAI NENKAI in Japanese 25-27 May 88 p 154

[Authors: Takumi Wakamoto, Tetsuo Nakayasu, Katsuro Masunaga, and Yasuhiko Kohtoku, Ube Industries, Ltd.]

[Text] I. Introduction: Silicon nitride whiskers are expected to serve as metallic or ceramic composite materials that can be used at high temperatures because they are strong and highly elastic. In this study, we synthesized beta-Si_3N_4 whiskers from amorphous silicon nitride by crystallization. Then, these whiskers were used to fabricate fiber reinforced composites (FRC). The composites' mechanical properties and their effects were studied.

II. Experimental Methods: II-1. Synthesis of beta-Si_3N_4 whiskers. A small amount of Y_2O_3 was added to amorphous silicon nitride powder, which was obtained by thermally decomposing silicon diimide {$Si(NH_2)$}, and thoroughly mixed in a ball mill. This powder mixture was crystallized in a nitrogen atmosphere at 1600--1750°C obtain beta-silicon nitride.

II-2. Fabrication of FRC. The whiskers obtained in II-1 were added to beta-SiAlON (z=2) powder derived from amorphous silicon nitride and then mixed with ethanol in a ball mill. The amount of whiskers added was varied from 0 to 50 weight percent. The resulting powder mixture was sintered by hot pressing at 1750°C for one hour at a pressure of 250 kg/cm^2. The density, three-point bending strengths (at room temperature and 1200°C), hardness, and fracture toughness (determined using the IM method) of the sintered product were measured. An optical microscope and an SEM were used to observe the structure of the sintered product.

III. Results and Discussion: All synthesized whiskers were white or yellow-white in color, forming straight crystals 10--40 microns long and 0.5--1.5 microns in diameter according to the SEM image shown in Fig. 1. Only a peak for beta-Si_3N_4 was detected in x-ray diffraction.

A photograph of the lapped surface of an FRC test sample taken using optical microscopy is presented in Fig. 2. Whiskers imbedded in a matrix are easy to confirm in this figure. By measuring the mechanical properties of this FRC, we found that bending strengths (at room temperature and 1200°C) and hardness

did not change much. On the other hand, we confirmed that the FRC's fracture toughness increased as the whisker content increased (Fig. 3).
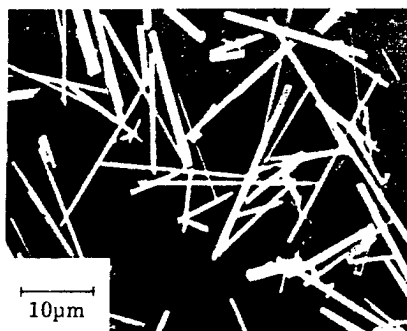
Fig. 1. SEM photograph of beta-silicon nitride whiskers.

Fig. 2. Lapped surface of an FRC.
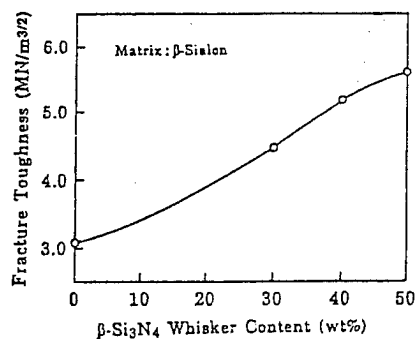
Fig. 3. Relationship between fracture toughness and beta-Si_3N_4 content.

Synthesis of alpha-SiAlON Powder

[Authors: Tetsuo Nakayasu, Takesi Yamao, and Yasuhiko Kohtoku, Ube
Industries, Ltd.]

[Text] I. <u>Introduction</u>: Alpha-SiAlON, a popular high-temperature structural
material, is represented by the general formula $M_x(Si,Al)_{12}(O,N)_{16}$ (where $0 <$
$x \leq 2$, M is either Li, Mg, Ca, or a metallic lanthanide element other than La
and Ce). In order to obtain a uniform microstructure, which strengthens a
sintered product, alpha-SiAlON powder is synthesized from a material in the
alpha-SiAlON phase. Then the powder is sintered. In this study, we discuss
our work on alpha-SiAlON powder synthesized by pyrolysis of imide.

II. <u>Experimental Method</u>: An amorphous silicon nitride powder was obtained
from a pyrolysis of silicon di-imide $\{Si(NH)_2\}$ synthesized through a liquid
phase boundary reaction between $SiCl_4$ and liquid NH_3. The resulting powder
was then mixed in a vibrating mill for one hour in a nitrogen atmosphere with
the Al metal; a metal oxide formed as an interstitial solid solution between
the lattice of alpha-SiAlON crystals listed in Table 1. This powder mixture
was placed in a carbon crucible, set in a high-frequency induction furnace,
and fired at 1200--1600°C in a nitrogen atmosphere to produce a sintered
powder. The composition of the powder produced was analysed. In addition,
the product was observed using SEM. Its BET ratio surface area was measured,
crystalline phase was determined by x-ray analysis, and its crystallinity was
measured.

III. <u>Results and Discussion</u>: The properties of the product fired at 1600°C
are listed in Table 1. From the composition analysis and the determination of
the crystalline phase by x-ray analysis, we are almost certain that we
produced a SiAlON powder with the desired composition. However, we believe
that the product did not possess a perfect alpha-SiAlON single phase; we
believe that some alpha-Si_3N_4 phase remained because the high-angle tail of
the x-ray diffraction peak was slightly spread out.

We present in Fig. 1 the relationship between the firing temperature, which
ranged from 1200°C to 1600°C, and the specific surface area and crystallinity
of Li-based alpha-SiAlON. The specific surface area rapidly decreased between

1200°C and 1400°C, in good agreement with the graph of the crystallinity determined by x-ray diffraction. SEM observation of the synthesized powder also indicated that crystallization was almost complete at 1400°C.

In Fig. 2, an SEM photograph of a Li-based alpha-SiAlON powder fired at 1600°C is shown. The powder consisted of hexagonal single crystals with relatively uniform particle diameters of about 1 micron.

These powder products sintered well and were easily densified by sintering under a constant pressure.
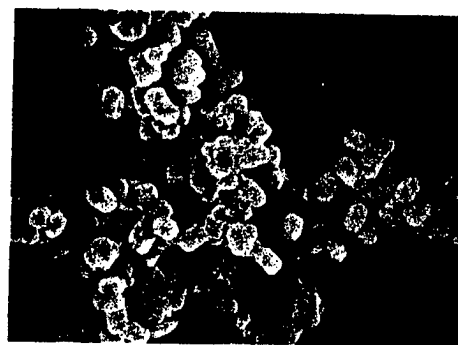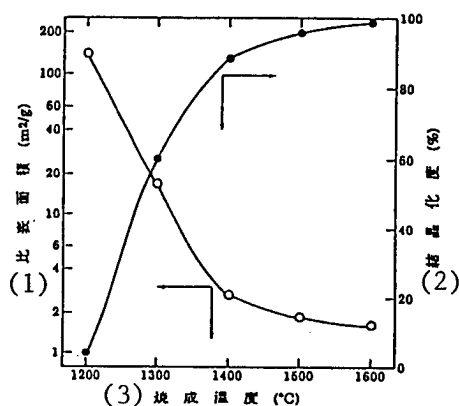
Fig. 1. Relationship between firing temperature, specific area, and crystallinity.

Fig. 2. SEM photograph of Li-based alpha-SiAlON powder.

Key: 1. Specific area.
2. Crystallinity.
3. Firing temperature.

Table 1. Properties of alpha-SiAlON powder.

Run. No.	(1)原料粉末(g)			(2)目的組成	(3)生成物組成	(4)生成相 (XRD)	S.S.A. (m²/g)
	Amor.SN	Metal Al	Oxiside				
1	180.6	14.9	Li$_2$O 5.5	Li$_{1.0}$(Si$_{10.7}$Al$_{1.5}$)(O$_{0.5}$N$_{15.5}$)	Li$_{0.9}$(Si$_{10.7}$Al$_{1.3}$)(O$_{0.6}$N$_{15.4}$)	(5)α'相(>90%)	1.9
2	56.1	5.6	MgO 2.4	Mg$_{0.5}$(Si$_{10.0}$Al$_{2.0}$)(O$_{1.0}$N$_{15.0}$)	Mg$_{0.4}$(Si$_{9.8}$Al$_{2.2}$)(O$_{0.9}$N$_{15.1}$)	α'相(>90%)	1.5
2	39.8	4.1	Y$_2$O$_3$ 3.8	Y$_{0.4}$(Si$_{10.2}$Al$_{1.8}$)(O$_{0.6}$N$_{15.4}$)	Y$_{0.4}$(Si$_{10.0}$Al$_{2.0}$)(O$_{0.8}$N$_{15.2}$)	α'相(>90%)	3.0

Key: 1. Raw material powder   2. Composition desired
3. Composition obtained   4. Phase obtained
5. Phase

10

Fiber Drawing in Gelation Process of Sodium Silicate Solution

[Authors: Hidenobu Itoh and Akio Tada, Kitami Institute of Technology]

[Text] <u>Introduction</u>: Recently, sol-gel methods that use metal alkoxides as raw materials have become popular for fabricating silica fibers at low temperatures. However, examples of using water glass (sodium silicate solution) as the raw material are rare. Using water glass poses some problems, such as removing the alkalis contained in water glass, but water glass has the advantage of being inexpensive. We examined fiber drawing ability and methods to remove alkalis during gelation processes initiated by adding gelling reagents to water glass.

<u>Experiment</u>: **Preparation of raw material solution and fiber drawing ability.** Number 2 water glass, gelling reagents (ethylene chlorohydrine, methyl acetate, ethyl acetate), and distilled water were mixed in various ratios and stirred either at room temperature or while being heated (40--50°C) until fibers could be drawn. Fiber drawing ability was qualitatively measured by quickly pulling up a glass rod after its tip was dipped into the raw material solution. **Alkali removal processing.** Fibers drawn by the procedure described above were soaked in various acid solutions.

<u>Results</u> and <u>Discussion</u>: **Effects of gelling reagents.** Although sulfuric acid and other acids are commonly used as gelling reagents in forming silica gels from water glass, we used reagents that generate acid from hydrolysis in order to make the gelation proceed slowly. While ethylene chlorohydrine is a well-known, uniform precipitation reagent in catalytic preparation, it causes gelation as soon as it is mixed with a solution, and one cannot obtain a solution from which fibers can be drawn. Raw material solutions with good fiber drawing ability could be prepared using methyl acetate and ethyl acetate. With the former, the resulting solution separated into two phases, and the liquid at the bottom allowed fiber drawing. However, fibers could be drawn only for a short duration. In the case of the latter, a few hours after a raw material solution was formed, the entire solution allowed fiber drawing for about one hour. We could easily draw gel fibers 10--20 microns [in diameter]. (The amount of gelling reagent added was 1.8 times the amount of Na in the water glass.) The pH of the solution when fiber drawing was

11

possible was about 9. Alkali removal processing. The gel fibers thus
obtained easily dissolved in water, but they became markedly waterproof after
acid processing. When we compared the effects of treating them in an alcohol
solution of acetic acid, aqueous solution of hydrochloric acid, or an aqueous
solution of sulfuric acid, we found that the first two solutions produced
brittle fibers while the sulfuric acid processing produced fine, strong gel
fibers (Fig. A). Structure of gel fibers. An x-ray diffraction pattern of a
sample fired at 1000°C is shown in Fig. B. Although a diffraction peak of
partially crystallized silica is visible in Fig. B, but this diffraction
pattern is almost the same as that for silica gel. No diffraction peaks
attributable to sodium silicate were found. Sodium was hardly recognized in
an EPMA analysis applied to the elemental composition of the surface,
indicating that the alkali was thoroughly removed. The results presented here
suggest the possibility of fabricating silica gel glass fibers from water
glass using our method. While it is already known that one can draw fibers
from water glass directly,[1] we found that the Na residue after the drawn
fibers were processed for alkali removal tended to be larger than the residue
obtained by our method.
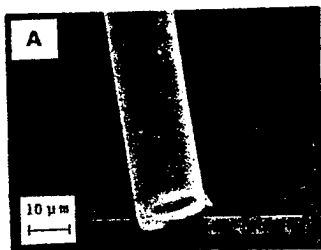
Fig. A. SEM photograph of a gel
fiber.
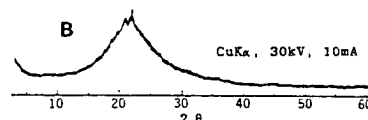
Fig. B. X-ray diffraction pattern of a
fiber fired at 1000°C after alkali
removal processing (6N·HNO_3, 18 hours).

Reference

1. Sumio Sakka, "Garasu Hishoshitsuno Kagaku [The Science of Amorphousness of
   Glass]," (Uchida Rokakuho, 1985), p. 155.

Preparation of MgO-B$_2$O$_3$-SiO$_2$ Coating Films by a Sol-Gel Method

[Authors: Noboru Tohge, Naoyuki Asano and Tsutomu Minami, Department of Applied Chemistry, University of Osaka Prefecture]

[Text] I: If one applies a sol-gel method using metal alkoxides as raw materials, it is possible to fabricate a glass which is difficult to form by suddenly cooling a molten solution. In this study, we examined the conditions needed to fabricate glass films of MaO-B$_2$O$_3$-SiO$_2$ that contain MgO in order to improve the water resistance of borosilicate glass films, which are expected to be useful as electric insulation films.

II: Procedures to prepare coating films are shown in Fig. 1. Si(OEt)$_4$ and B(O-nBu)$_3$ were used as the raw materials for SiO$_2$ and B$_2$O$_3$ respectively, and (MgOEt)$_2$ or MgCl$_2$ were used as the raw materials for MgO. Solvent EtOH and H$_2$O for hydrolysis were used in the ratio EtOH/Si(OEt) = 5 and H$_2$O/Si(OEt)$_4$ = 4; HCl was used as a catalyst. Using the dipping method in a dry atmosphere, coating was applied onto a glass substrate and the final thermal processing was performed at 500°C.

III: We found that the amount of HCl added affected the quality of the glass films very much. Figure 2 illustrates the relationship between the amount of HCl added and the light transmittance of the 5MgO-15B$_2$O$_3$-80SiO$_2$ glass film at a wavelength of 400 nm. In the case of Mg(OEt)$_2$, the glass film dissolves in EtOH only when HCl/Mg(OEt)$_2 \geq$ 2; it then forms uniform transparent glass films. Even for MgCl$_2$, which dissolves in EtOH, the HCl content must satisfy HCl/MgCl$_2 \geq$ 2 to obtain transparent glass films. From these observations, we believe that HCl plays a more important role (for instance, peptisation) than a mere catalyst for hydrolysis.

Based on these results, we examined the [composition] range under which glass films were formed while the ratio HCl/Mg(OEt)$_2$ > 2 was maintained. We indicate in Fig. 3 the composition range where transparent films are formed even after a sample is thermally processed for 15 minutes at 500°C. With this method, we can fabricate borosilicate glass films that contain as much as 10 mole percent of MgO. On the other hand, even the films that are opaque at this temperature are found to be amorphous from x-ray analyses. We believe

that this opaqueness is caused mainly by split phases.

As is explained above, we found that $MgO-B_2O-SiO_2$ glass films can be fabricated by using a relatively large amount of HCl.
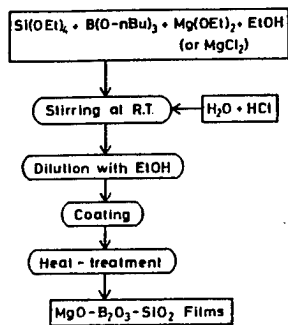
Fig.1 Preparation procedure of MgO-B_2O_3-SiO_2 coating films.
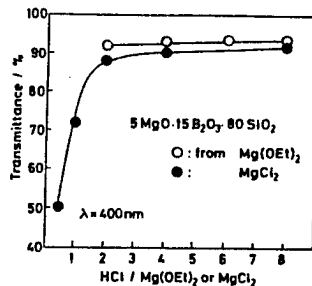
Fig.2 Transmittance vs. the amount of HCl for $5MgO\cdot15B_2O_3\cdot80SiO_2$ films.
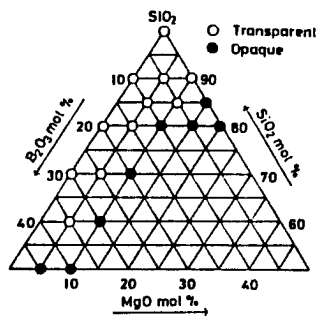
Fig.3 Compositional region where the transparent films are formed.

14

Extrusion of Fine Ceramic Powder with Water Binder

[Authors: Takeo Nakagawa,* Lihong Zhang,* Hiroyuki Noguchi,* and Kiyoshi Suzuki,** Institute of Industrial Science, University of Tokyo,* and Nippon Institute of Technology**]

[Text] 1. Introduction: In order to facilitate the removal of binders from molded products of fine ceramics, we are studying molding methods that use water as a binder. We have already verified that adequate mobility is obtained with a small amount of water binder by introducing low-frequency vibrations to a punch when products are formed in metal molds, thus enabling us to form products with complicated shapes.[1] In this study, we tried to extrude ceramic wires using water as a binder.

2. Experimental Apparatus: We used an electric hydraulic, servo-valve type vibrating press with a capacity of 4.5-ton static pressure and 3-ton dynamic pressure in our extrusion experiment. The die and punch are made of a sintered hard alloy, and [the punch] has a diameter of 20 mm. The extrusion dies (nozzles) are made of diamond with holes 0.1, 0.3, and 0.5 mm in diameter. Alumina, silicon nitride, and silicon carbide ceramic powder samples were used (Table 1). The binder was an aqueous solution containing PVA.

3. Experimental Results: The amount of PVA added to the water binder was kept to the minimum amount necessary to prevent the powder and water from separating during the extrusion. We used 6 weight percent for silicon carbide, which consisted of fine particles with small diameters, and 10 weight percent for alumina and silicon nitride. The results of our ceramic powder extrusion are shown in Table 2. Filled circles represent the cases in which no wires were extruded even when the punch was loaded with the maximum pressure of 4.5 tons (surface pressure of P_{max} = 1433 kgf/cm^2), and the open triangles stand for the cases in which fibers were fabricated only in the beginning. Open circles represent the cases in which fibers were produced, while open double circles represent the cases in which the fibers seemed to have particularly good surface characteristics. By adding the proper amount of the binder, we were able to extrude very fine ceramic fibers 0.1 mm in diameter (Fig. 1).

The amount of water binder needed to extrude fibers from a 0.1-mm nozzle was 41 volume percent (18 weight percent) for silicon carbide, 50 volume percent (20 weight percent) for alumina, and 47 volume percent (22 weight percent) for silicon nitride. Also, as we increased the nozzle hole diameter, we needed to add less water for extrusion.

4. <u>Conclusion</u>: We have verified that ceramic fibers can be extruded by adding a small amount of PVA (1.0--2.2 weight percent) when water is used as a binder.

References

1. Nakagawa, Zhang, et al., Abstracts of 1987 Fall Conference on Powder Metallurgy, p. 80.

Table 1. Specifications of fine ceramic powder samples.

種類 (1)	品番他 (2)	粒度分布 (3) (4)			比表面積 m²/g (4)	真密度 g/cm³ (5)
炭化珪素 0.15μm*	201A200204 (三井東圧) (7)	-2.3/100	-1.0/87	-0.5/62 μm wt%	3.9	3.22
アルミナ (8)	UA-5055 (昭和電工) (9)	-3.0/100	-1.0/86	-0.5/64 μm wt%	5.1	3.97
窒化珪素 (10)	SN-9S (11) (電気化学)	-16/100	-5.0/57	-1.0/42 μm vol%	7.0	3.18

(6)

*TEMによる平均粒径 (12)

Key: 1. Type
3. Particle distribution
5. True density
7. Mitsui Toatsu Chemicals
9. Showa Denko
11. Denki Kagaku Kogyo

2. Stock number
4. Specific surface area
6. Silicon carbide
8. Alumina
10. Silicon nitride
12. Average particle diameter determined by TEM

Table 2. Experimental results of extrusion of various ceramic powders.

Key: 1. Amount of water binder added
2. Silicon carbide
3. Alumina
4. Silicon nitride
5. Nozzle hole diameter

水ダバインダ添加量 (1)		炭化珪素 (2)					アルミナ (3)			窒化珪素 (4)		
vol.%		38	40	41	45	48	43	47	50	41	44	47
wt.%		16	17	18	20	22	16	18	20	18	20	22
(PVA:wt.%)		0.96	1.02	1.08	1.20	1.32	1.6	1.8	2.0	1.8	2.0	2.2
(5) ノズル穴径	0.1mm	●	△	◎	○	○	●	△	○	●	△	○
	0.3	●	○	◎	○	○	●	○	○	●	△	○
	0.5	●	○	◎	○	○	●	○	○	●	△	○

16

Fig. 1. Ceramic fibers extruded by the water binder method.

Key: (a) Silicon carbide fibers
0.1 mm in diameter
(b) Silicon carbide fibers
0.3 mm in diameter
(c) Alumina fibers 0.3 mm
in diameter

(a) φ0.1mm炭化珪素繊維

(b) φ0.3mm炭化珪素繊維

(c) φ0.3mmアルミナ繊維

17
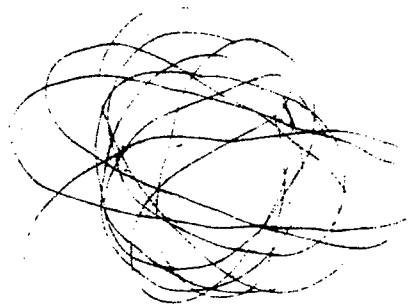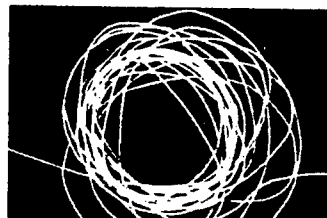
X-Ray Stress Measurement of Aluminum Oxide by Gaussian Curve Method

[Text] 1. Introduction

Fine ceramics excelling in corrosion resistance, thermal resistance, wear resistance, and electrical insulating property have been widely used industrially in recent years. Residual stress generated when sintering ceramics and when conducting machinings such as grinding, etc., greatly affect the strength of ceramics. The stress measurement method by X-ray diffraction has the advantage of nondestructively measuring the residual stress in thin polycrystal material layers of 10 to several 10 μm and it is considered an effective method for measuring the residual stress of ceramics. Much research has been conducted recently on residual stress measurement of ceramics by using the X-ray method.[1-8]

The diffraction line profile by a single-wavelength X-ray can be approximated by the Gaussian function.[9] The X-ray stress measurement method by the Gaussian curve method is the method that makes the principal axis of the Gaussian function approximating the diffraction line peak the diffraction line peak position.[10,11] This method in comparison to other methods has the characteristic of promptly measuring the stress value with good reproducibility.[12-15] Since there are many cases when the diffraction line of ceramics appears with diffraction lines of $K\alpha_1$ and $K\alpha_2$ separated, the Gaussian curve method is also capable of accurately measuring the peak position for such materials as well as by using the $K\alpha_1$ diffraction line.[7,8]

By the way, in order to measure the stress value with good accuracy by X-ray diffraction, it is necessary to measure the stress constant by X-ray for converting the strain measured by X-ray to a stress value. Since the values measured by X-ray vary widely by the statistical variation[16] inherent to X-ray counts, it is important to obtain the standard deviation expressing the variation size of measured values generated by this statistical variation and study the reproducibility of measured values. Fortunately, this standard deviation is analytically available from a single measured

value for measured values by the regular counting method.[10,12-18] It has been made clear in the previous report[14] that the standard deviation of stress values thus obtained by the Gaussian curve method coincides well with the standard deviation of stress values obtained by measuring 65 times repeatedly.

The X-ray stress measurement of silicon nitride[8] and silicon carbide[7] by the Gaussian curve method has been made clear in our previous report. In this research, we have taken up alumina which is the most widely industrially used among fine ceramics, measured by X-ray the stress and elastic constants by using the Gaussian curve method, analytically obtained the standard deviation of these various constants by means of the statistical variation inherent to X-ray counts by using the formula indicated in the previous report,[18] and have made clear the reliability of measured values.

2. Experiment Method

The material used in this experiment is the atmospheric sintered α-alumina (α-Al$_2$O$_3$) of 99 percent purity. The specimen was ground to 630 μm with a #230-particle-size diamond grindstone after its cutting with a diamond cutter. Moreover, about 30 μm lapping was conducted on the surface by a diamond grindstone with the particle size of 2 μm for removing the processed layer on the surface. The shape of the used specimen is shown in Figure 1. This specimen was attached to the four-point bending device shown in Figure 2 and the bending stress applied in the center part of the specimen was measured in the longitudinal direction of the specimen by X-ray. An orthogonal biaxial strain gauge with a gauge length of 2 mm was attached to the rear center part of this specimen as shown in Figure 2 and the strain generating on the specimen was measured. Moreover, a measuring ring has been provided on this bending device as shown in Figure 2 and the stress placed on this specimen was obtained by this ring.
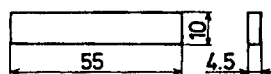
Figure 1. Specimen

The stress measurement by X-ray was conducted under the conditions shown in Table 1 by attaching a parallel beam optical system slit to the programmable automated X-ray diffraction developed by us and using the parallel gradient method. The diffraction line peak position was decided by the Gaussian curve method by using the ψ fixed method maintaining the direction of the diffraction plane normal in fixed condition.

It is necessary to select a diffraction line with a diffraction angle as high as possible for obtaining a stress value with good accuracy by X-ray. Therefore, the diffraction line of the specimen was measured by using the Co, Cr, and CuKα radiations but since an isolated diffraction line having a sufficient strength in the diffraction angle of more than 150° was not available by the Cr and CuKα radiations, the (229) plane with the diffraction angle of 154° was measured by using the CoKα radiation in this research. Four points of 0°, 26°, 39°, and 50° were selected for the
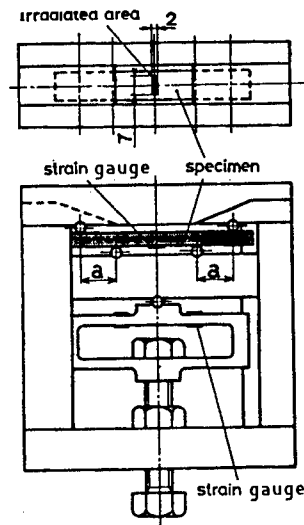
Figure 2. Bending Device

Table 1. Conditions of X-Ray Stress Measurement

Characteristic X-rays	CoKα
Diffraction plane	(229)
Filter	Ferrite foil
Tube voltage, kV	40
Tube current, mA	25
Divergence angle of slit, deg	0.5
Irradiated area, mm^2	2 x 7
Angular interval, deg	0.05
Preset time, sec	10
ψ angles, deg	0, 26, 39, and 50

ψ angle formed between the diffraction plane normal and specimen plane normal so that $\sin^2\psi$ became approximately of the same interval. Moreover, the background (GB) counts of the diffraction line were obtained for all ψ angles by connecting the two points for diffraction angles x = 152° and X = 157° with a straight line.[10]

3. Results of Experiment

3.1 Measurement of Elastic Constant by Strain Gauges

Figure 3 shows the relation between the compressive load applied by using a tensile tester (Shimadzu autography) and the mean strain value of the four strain gauges attached to the load ring for obtaining the calibration curve of the bending device shown in Figure 2. Figure 3 has shown that the strain of the load ring increases in proportion to the load and the load placed on the bending device is available from the strain generated on the load ring when this straight line is used.

20
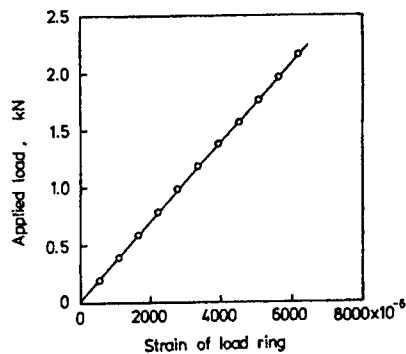
Figure 3.   Load-Strain Diagram for
            Bending Device
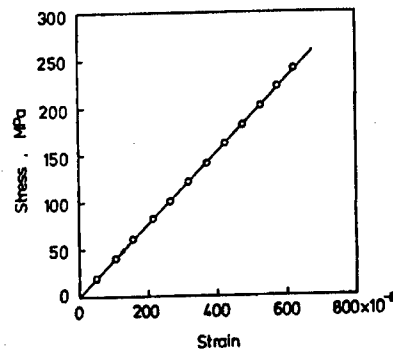
Figure 4.   Stress-Strain Diagram for
            Specimen

Figure 4 shows the relation between the strain and stress in the longitudinal direction of the specimen measured from the strain gauge attached on the back surface of the specimen when an alumina specimen has been attached to the bending device shown in Figure 2. The stress has been obtained as follows. That is, the stress generating at the center part of the specimen surface becomes Pa/Z when one-half of the load applied on the bending device shown in Figure 2 is made P and the section modulus is made Z. Load P has been obtained from the straight line of Figure 3. Young's modulus E of this specimen was 384.4 GPa from Figure 4.

The relation between the longitudinal strain ε and lateral strain ε' of the specimen obtained from the biaxial strain gauges attached to the specimen for obtaining the Poisson's ratio of the specimen is shown in Figure 5. The Poisson's ratio γ obtained from the slope of the straight line applied to various points shown in Figure 5 by using the least squares method was 0.241.
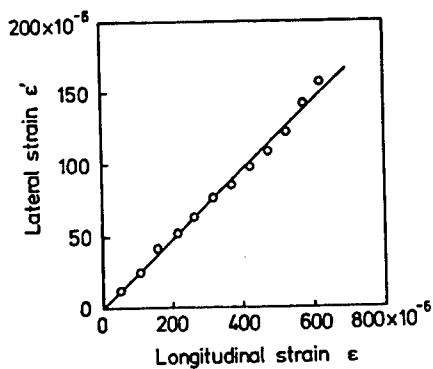
Figure 5.   Change in Lateral Strain
            for Specimen
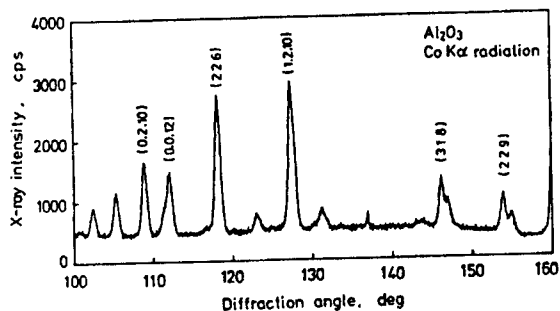
Figure 6.   Diffraction Line for
            Aluminum Oxide

3.2 Gaussian Function Approximation of $K\alpha_1$ Diffraction Line

Figure 6 shows the diffraction line for the alumina specimen obtained by continuously recording the X-ray counts, i.e., the X-ray strength (cps) measured at the preset time of 1 second on the X-Y plotter by using the

automated X-ray diffractometer. The (1.2.10) plane with a high strength was used in the alumina experiment[6] previously conducted but the highest angle side (229) plane diffraction line was used this time for raising the accuracy of stress measurement.

Figure 7 shows the diffraction line in which the actual measured values of X-ray counts have been corrected by the background (BG) counts and LPA factor. The curve shown in Figure 7 is the Gaussian function[19] obtained by the least squares method by using the points of more than 55 percent of the maximum value of the diffraction line of $K\alpha_1$ radiation and it is known from Figure 7 that the diffraction line peak by $K\alpha_1$ single wavelength can be approximated well by the Gaussian function.
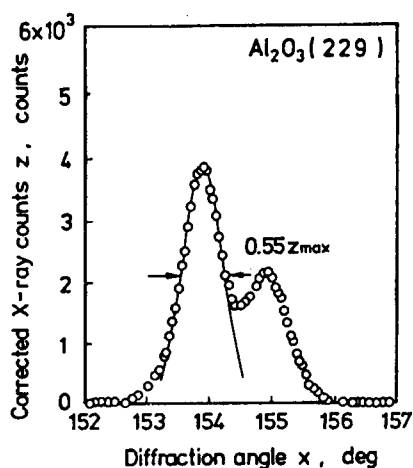
Figure 7. Gaussian Function Fitted to $K\alpha_1$ Diffraction Profile Corrected for Background
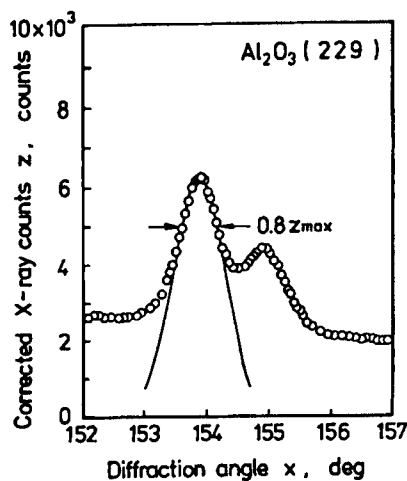
Figure 8. Gaussian Function Fitted to $K\alpha_1$ Profile Which Is Not Corrected for Background

Figure 8 shows the diffraction line of X-ray counts that has omitted the BG correction and has been corrected by the LPA factor only. Moreover, the curve shown in Figure 8 is the Gaussian function[19] obtained by the least squares method by using points of more than 80 percent of the maximum value of the diffraction line of $K\alpha_1$ radiation. Figure 8 as seen here has shown that the diffraction line peak can be approximated by the Gaussian function even when omitting the BG correction. From results of Figures 7 and 8, points of more than 55 percent of the maximum X-ray counts (Z_{max}) were used when BG correction was made and points of more than 80 percent of Z_{max} were used when BG correction was omitted in the computation of the diffraction line peak position.

3.3 Effect of Background Correction on Stress Value

Table 2 shows the results of a specimen applied with various bending stresses measured by the Gaussian curve method by using the bending device shown in Figure 2 for checking the effect of background correction on stress value. After measurement of the stress constant K, the value shown in Table 3 was used for stress computation. Moreover, the 95 percent confidence

limits of stress $S\pm1.96\ \sigma_s$ was obtained from the standard deviation[10,18] of stress value S expressing the size of variation generated by the statistical variation inherent to X-ray counts and is shown in Table 2.

Table 2. Effect of Background Correction on Stress Value

Applied stress τ (MPa)	95% Confidence limits of stress $S\pm1.96\ \sigma_s$ (MPa)	
	Not corrected for background	Corrected for background
0	36 ± 12	25 ± 10
48	91 ± 12	82 ± 10
94	134 ± 12	120 ± 10
141	171 ± 11	162 ± 10
188	227 ± 11	217 ± 11
237	277 ± 12	265 ± 12

Table 3. 95% Confidence Limits of X-Ray Elastic Constants and Stress Constant

Compliance	$(1 + \nu)/E$, $(10^3$ GPa$)^{-1}$	2.85 ± 0.17
	ν/E, $(10^4$ GPa$)^{-1}$	5.19 ± 0.57
Young's modulus E, (GPa)		429 ± 24
Poisson's ratio ν		0.22 ± 0.02
Stress constant K, (MPa/deg)		-704 ± 42

As known from Table 2, a difference greater than the dispersion range shown by the confidence limits of stress is not recognized between the BG corrected stress value and the BG uncorrected stress value. Moreover, a great difference is not recognized by BG correction in the standard deviation σ_s of the stress value or 95 percent confidence intervals for stress $S\pm1.96\ \sigma_s$. However, the reason why the difference of the stress value corrected for background and the stress value not corrected for background was slightly larger this time in the alumina (229) plane in comparison to that of the previously obtained steel,[18] silicon nitride,[8] and silicon carbide[7] was because the linear slope of BG was larger than that of the previous case. Since BG correction as seen here does not greatly affect the stress value, only results omitting BG correction will be shown hereinafter.

3.4 X-Ray Elastic Constants and Stress Constants

Figure 9 shows the $\sin^2\psi$ diagram of a specimen applied with various bending stresses by the bending device shown in Figure 2. The 95 percent confidence intervals of stress $\pm1.96\ \sigma_p$ of the peak position was obtained from the standard deviation σ_p of the peak position that had been analytically obtained from the formula shown in the previous reports[10,18] and only the maximum and minimum values are shown in this diagram. It is shown from Figure 9 that the $\sin^2\psi$ diagram for all applied stresses also shows a fairly superior linearity.

Figure 10 shows the result of plotting slope M of $sin^2\psi$ diagram in Figure 9 against bending stress τ. The 95 percent confidence intervals $\pm1.96 \ \sigma_M$ obtained from the standard deviation σ_M of M computed from the formula shown in the previous report[18] is also shown in this diagram. Moreover, Figure 11 shows the relation between intercept N of $sin^2\psi$ diagram in Figure 9 and applied stress τ. The 95 percent confidence intervals $\pm1.96 \ \sigma_N$ analytically obtained from standard deviation[18] σ_N of N is also shown in this diagram. All points show a superior linearity in the dispersion range shown by confidence intervals in both Figures 10 and 11.
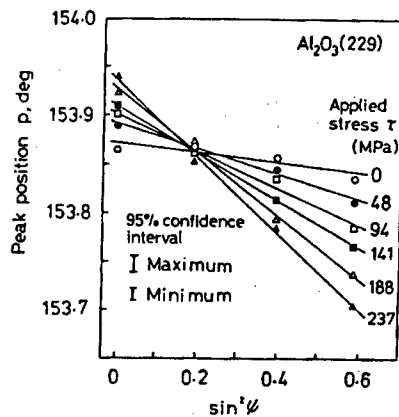
Figure 9. $Sin^2\psi$ Diagram for Various Applied Stresses
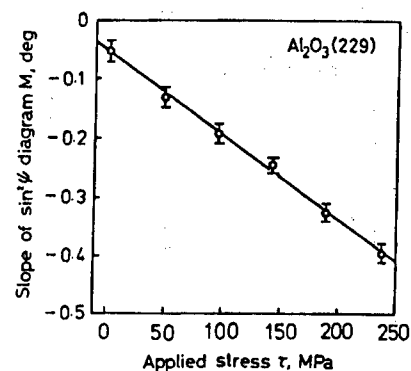
Figure 10. Slopes of $Sin^2\psi$ Diagram With Their 95 Percent Confidence Intervals for Various Applied Stresses
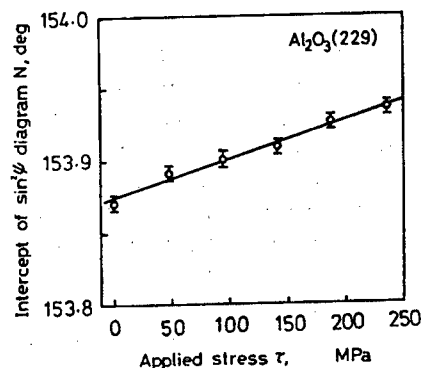
Figure 11. Intercepts of $Sin^2\psi$ Diagram With Their 95 Percent Confidence Intervals for Various Applied Stresses

The 95 percent confidence intervals of X-ray measured compliances, Young's modulus E, Poisson's ratio ν, and stress constant K are shown in Table 3. The standard deviation of these values were computed from the formula shown in the previous report.[18] The X-ray measured Young's modulus E shown in Table 3 is slightly larger than the mechanically measured value of 394 GPa but the Poisson's ratio ν almost coincides with the mechanically measured value of 0.24.

3.5 Residual Stress of Processed Layer

Figure 12 is the $\sin^2\psi$ diagram for ground surface and Figure 13 is the $\sin^2\psi$ diagram for lapped surface. These $\sin^2\psi$ diagrams have measured the surface of an alumina specimen ground and lapped by the method mentioned in Chapter 2 in the longitudinal direction (grinding direction) and measured the peak position in the positive and negative directions of ψ for checking the ψ slit phenomenon of the processed layer. The 95 percent confidence intervals of peak positions are shown in these diagrams. Practically no ψ splits were recognized in the lapped surface of Figure 13. In contrast to this, a slight ψ slit was recognized in the ground surface shown in Figure 12.
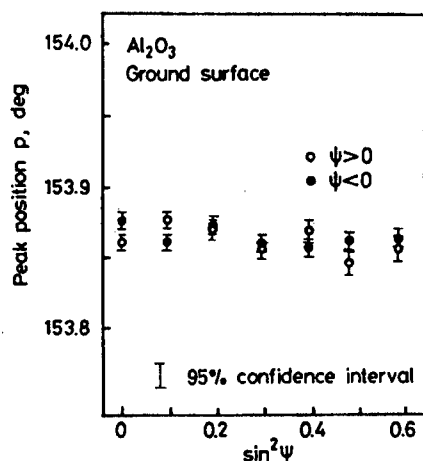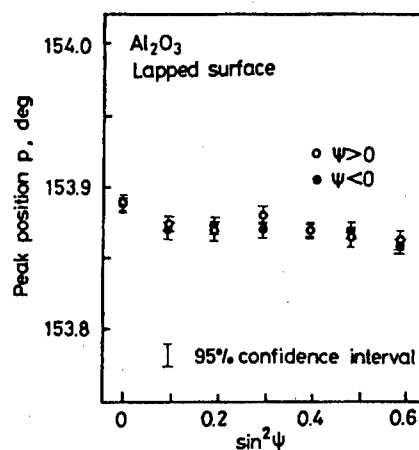
Figure 12.   Sin²ψ Diagram for Ground   Figure 13.   Sin²ψ Diagram for Lapped
Surface   Surface

Table 4 shows the measured results of residual stress in the ground and lapped surfaces. Moreover, the variation of effective penetration depth with $\sin^2\psi$ for CoKα radiation against alumina is shown in Figure 14. Results for CuKα and CrKα radiations have also been shown for reference in this diagram. As shown from Figure 14, the penetration depth of CoKα radiation against alumina lies midway between the penetration depths of CuKα radiation and CrKα radiation. It is known from Figure 14 that the effective penetration depth of alumina (229) plane by CoKα radiation used in this research is 15~25 μm. It is considered that the thickness of the processed layer by grinding is 10~30 μm and the thickness of the processed layer by lapping is less than 10 μm. Although it cannot be necessarily said that values in Table 4 have measured only the residual stress in the processed layer as the residual stress in this processed layer also reduces as it enters the specimen interior from the surface, it is known from Table 4 that the residual stress of alumina that has been ground and lapped under the conditions mentioned in Chapter 2 is quite small.

Table 4. 95 Percent Confidence Limits of Residual Stresses Induced by Grinding and Lapping

Surface finish	Direction of stress	95 percent confidence limits of stress (MPa)
Ground	Ground direction	18 ± 9
	Perpendicular to ground direction	-7 ± 10
Lapped	Ground direction	18 ± 9
	Perpendicular to ground direction	27 ± 10
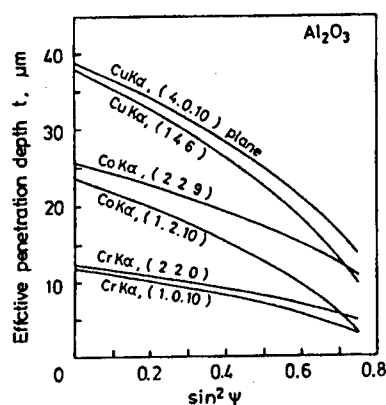
Figure 14. Variation of Effective Penetration Depth With Sin²ψ for Cu, Co, and CrKα Radiation

4. Conclusion

Together with measuring the stress and elastic constants of the α-alumina (229) surface by using the CoKα radiation under the Gaussian curve method, the standard deviation expressing the dispersion size of these measured values which is generated by the statistical variation inherent to X-ray counts has been analytically obtained by the method shown in the previous report[18] and the reproducibility of these measured values has been studied. The following are the main conclusions that have been available.

(1)   The diffraction line of (229) plane separates into the $K\alpha_1$ and $K\alpha_2$ diffraction lines but the $K\alpha_1$ diffraction line peak can be approximated well by the Gaussian function and alumina stress can be measured by using this.

(2)   The background (BG) correction can be omitted as it does not practically affect the stress value and standard deviation.

(3)   The 95 percent confidence intervals of X-ray stress and elastic constants of alumina are as shown in Table 3.

(4)   The 95 percent confidence intervals of X-ray measured Young's modulus E and Poisson's ratio ν of alumina were 429 ± 24 GPa and 0.22 ± 0.02, respectively.   In contrast to this, the mechanically measured E and ν were

26

384 GPa and 0.24, respectively, and although the Poisson's ratio almost coincided, the X-ray measured Young's modulus was slightly greater.

In conclusion, we express our deep gratitude to all members of the Nippon Tokushu Yogyo Co., Ltd., that have prepared for us the specimens used in this research.

References

1. Tanaka, et al., (3 persons), MATERIALS, Vol 36 No 407, 1987, p 792.

2. Ibid., p 817.

3. Kishimoto, et al., Ibid., p 810.

4. Ei, Fujiwara, and Fujimoto, Ibid., Vol 37 No 413, 1988, p 204.

5. Ibid., p 210.

6. Kurita, et al., (4 persons), MACHINE LOGIC, Vol 54 No 500A, 1988, p 854.

7. Ibid., (3 persons), MATERIALS, Scheduled for publication.

8. Kurita and Ono, Manuscripts of lecture theses for the 25th Symposium on X-ray Material Strength, THE SOCIETY OF MATERIALS SCIENCE, JAPAN.

9. H.P. Klug and L.E. Alexander, "X-ray Diffraction Procedures for Polycrystalline and Amorphous Materials," John Wiley, 1974, pp 291, 635.

10. M. Kurita, JOURNAL OF TESTING AND EVALUATION, Vol 9 No 5, 1981, p 285.

11. Ibid., "Role of Fracture Mechanics in Modern Technology," Elsevier Science Publishers, B.V., 1987, p 863.

12. Ibid., JOURNAL OF TESTING AND EVALUATION, Vol 9 No 2, 1981, p 133.

13. Ibid., Vol 10 No 2, 1982, p 38.

14. Ibid., Vol 11 No 2, 1983, p 143.

15. Kurita, Amano, and Sakamoto, MATERIALS, Vol 31 No 345, 1982, p 609.

16. Kurita, MACHINE LOGIC, Vol 43 No 368, 1977, p 1358.

17. Ibid., Scheduled for publication.

18. Ibid., Manuscripts of lecture theses for the 25th Symposium on X-Ray Material Strength, 1988, THE SOCIETY OF MATERIALS SCIENCE, JAPAN.

19. Ibid., MACHINE LOGIC, Scheduled for publication.

X-Ray Stress Measurement or Silicon Nitride by Gaussian Curve Method

[Article by Masanori Kurita, Nakaoka University of Technology and Nobuyuki Ono,
Citizen Watch Co., Ltd.; from the 25th Symposium on X-Ray Studies on
Mechanical Behavior of Materials held 21-22 July 1988]

[Text] 1. Introduction

With ceramics becoming widely used for special purpose materials and
structural materials in recent years, it has been made clear that residual
stress induced when preparing the machining ceramics exerts a great effect
on the strength of ceramics and the establishment of a residual stress
measurement method is strongly demanded. Complying with such an industrial
demand, research was recently conducted on residual stress measurement of
ceramics by the X-ray method capable of nondestructively measuring the
residual stress of polycrystals.[1-7] By the way, it is first of all necessary
to decide the stress constant by X-ray measurement for measuring the stress
value with good accuracy by the X-ray method.[8-12] Moreover, since the X-ray
measured values widely vary by the statistical variation[13] inherent to the
X-ray strength, it is important to obtain the standard deviation expressing
the varying size of measured values caused by this statistical variation.
Fortunately, the standard deviation of the diffraction line peak position,
stress value[14-18] and half value breadth are analytically available from a
single measurement in the measurement conducted by the regular counting
method. Moreover, the method of obtaining standard deviation of the X-ray
elastic constant has been shown in the previous report.[20]

The diffraction line profile by a single wavelength X-ray can be
theoretically approximated by the Gaussian function.[21]. The X-ray stress
measuring method by means of the Gaussian curve method is a method of making
the principal axis of the Gaussian function that has approximated the
diffraction line peak the diffraction line peak position.[15-22] Among the
various X-ray stress measuring methods[14-18] by the regular computing method,
the Gaussian curve method has the special characteristic of promptly
measuring the stress value with good reproducibility and it is considered
to be an effective practical use method. In the measurement values[15] of
residual stress by our Gaussian curve method using steel material, it is not
only necessary to correct the diffraction line background in this method as

done in the measurement of the half value breadth method but the measurement utilizing the diffraction line by $K\alpha_1$ single wavelength is also possible for materials in which the diffraction lines by $K\alpha_1$ and $K\alpha_2$ radiations separately appear.[6,7] Therefore, a highly accurate measurement can also be expected when using the Gaussian curve method for materials like ceramics where it is difficult to accurately obtain the background of the diffraction line due to diffraction lines by $K\alpha_1$ and $K\alpha_2$ radiations appearing separately and diffraction lines from many diffraction planes mutually appearing close together.

This research as the basic research on X-ray stress measurement of ceramics by the Gaussian curve method has taken up silicon nitride, which is being widely used as a structural material in recent years, and together with studying the diffraction line peak determination method by this method, has measured the X-ray stress and elastic constants, has analytically obtained the standard deviation by the statistical variation inherent to X-ray counts by the method shown in the previous report[20] and has made clear the reliability of these measured values.

2. Experiment Method

The material used was a silicon nitride (Si_3N_4) produced by hot pressing and the specimen was 10.0 x 55.0 x 5.0 mm. This specimen after cutting with a diamond cutter was ground to about 50 μm with a #200-particle size diamond grindstone. Then, measuring surfaces of various X-ray constants were ground in order to about 100 μm by diamond grindstones of #400, #600, and #1000 particle sizes and it was lastly subjected to lapping of some 1 μm by using the #1500-particle size diamond grindstone. The ground direction was in the longitudinal direction of the specimen. After this, a uniform moment was applied to the specimen by using the four-point bending device shown in Figure 1 and the stress at the center part of the specimen with a 10.0 x 55.0 mm surface was measured in the longitudinal direction by X-ray. At the same time, strain generating on the specimen was measured by a strain gauge of 5 mm gauge length attached on the back side of the specimen. Moreover, a measuring ring shown in Figure 1 had been attached to this bending device and the load applied to the specimen was measured by this ring. Four strain gauges have been attached on this measuring ring and as a result of checking in advance the relationship between the load applied on this measuring ring and the reading of strain gauges by using a tensile tester, a superior linear relation was available between the two and the load applied to the specimen was available by using this calibration straight line.

The X-ray stress measurement was conducted under the measurement conditions shown in Table 1 by attaching a parallel beam optical system slit to the programmable automated X-ray diffractometer[6] developed by us and using the Gaussian curve method.[15,22] The ψ fixing method maintaining the direction of the diffraction plane normal in fixed conditions was used for the diffraction line and stress was measured by the parallel gradient method. Moreover, two types of radiations, $CuK\alpha$ radiation and $CrK\alpha$ radiation were used for the X-rays and (323) and (212) planes of silicon nitride were respectively measured for comparing the stress measurement results according to different diffraction planes. The preset time (measuring time of X-ray

counts) shown in Table 1 has been selected so that the maximum counts from these two diffraction planes became approximately the same. Furthermore, the X-ray data used in deciding the peak position of a single diffraction line buy the Gaussian curve method indicated about 15 points.
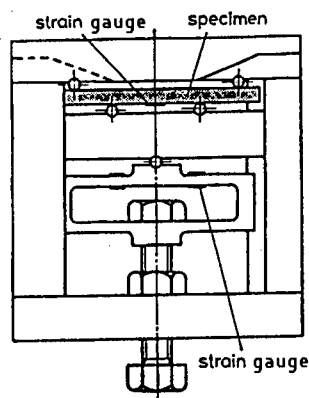
Figure 1. Bending Device

Table 1. Conditions of X-Ray Stress Measurement

Characteristic X-rays	CuKα	CrKα
Diffraction plane	(323)	(212)
Filter	Ni foil	V foil
Preset time	7 s	16 s
Tube voltage	40 kV	
Tube current	25 mA	
Divergence angle of slit	0.5 deg	
Irradiated area	$2 \times 7 \ mm^2$	
Step width	0.04 deg	

3. Experiment Results

3.1 Gaussian Curve Approximation of Diffraction Line

Figure 2 shows the diffraction line of the silicon nitride (323) plane measured by CrKα radiation and value z having X-ray counts corrected for background and LPA factors is shown in the axis of ordinates. As known from Figure 2, the diffraction line of (323) plane by $K\alpha_1$ and $K\alpha_2$ radiations has appeared separately. The curve shown in the diagram is the Gaussian function[23] obtained by the least squares method by using various points of more than 60 percent of z_{max} (maximum value of z) of $K\alpha_1$ radiation with high strength. On the right side of the $K\alpha_1$ diffraction line, the various fitted points are affected by the $K\alpha_2$ diffraction line and they separate from the Gaussian function when the X-ray strength becomes low, however, various points on the left side of the $K\alpha_2$ diffraction line ride considerably well on the Gaussian curve. As seen here, it is known that the diffraction line by the single wavelength X-ray can be approximated well by the Gaussian function in the same manner as the results of soft steel and alumina which we have already made clear.[6]
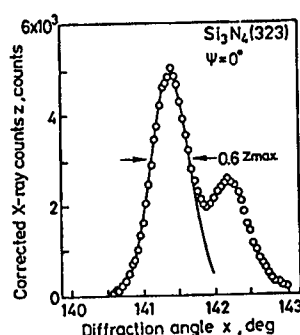
Figure 2. Gaussian Function Fitted
           to $K\alpha_1$ Diffraction Pro-
           file for (323) Plane
           Corrected for Background
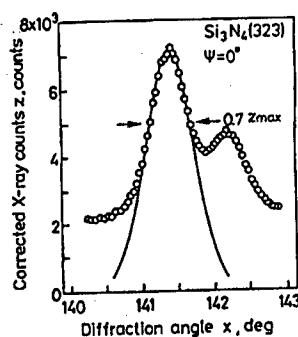
Figure 3. Gaussian Function Fitted
           to $K\alpha_1$ Profile for (323)
           Plane Which Is Not
           Corrected for Background

Figure 3 shows the diffraction line of the (323) plane shown by value z
which has corrected the actual measured value y of X-ray counts by LPA
factors only and omitting the background correction. The curve of this
diagram is the Gaussian function obtained by the least squares method by
using various points of more than 0.7 z_{max}. The diffraction line peak as
seen here can be approximated with the Gaussian function even when omitting
the background correction. From the results of Figures 2 and 3, various
points of more than 0.6 z_{max} were used for background correction and various
points of more than 0.7 z_{max} were used for those without background
correction for computing the diffraction line peak position. These various
points correspond to points of almost the same diffraction angle range.
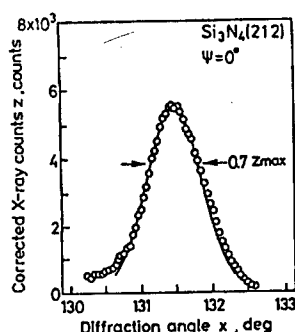
Figure 4. Gaussian Function Fitted
           to $K\alpha_1$ Doublet for (212)
           Plane Corrected for
           Background
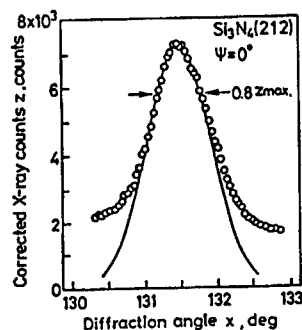
Figure 5. Gaussian Function Fitted
           to $K\alpha$ Doublet for (212)
           Plane Which Is Not
           Corrected for Background

Figure 4 shows the diffraction line of (212) plane measured by CrK radiation
and it is a doublet in which the $K\alpha_1$ and $K\alpha_2$ diffraction lines have
overlapped. The X-ray counts of Figure 4 have been corrected by the BG
strength and LPA factors. The diffraction line by $K\alpha$ doublet is generally
asymmetric and it is known from Figure 4 that the diffraction line peak
neighborhood can be approximated well by the Gaussian function just as in
the case of steel material.[14,24]

31

Figure 5 is the same as Figure 4 but X-ray counts have been corrected by the LPA factors only, omitting the background correction. The curve of the diagram is the Gaussian function obtained by using the various points of more than 0.8 z_{max}. As known from Figure 5, the diffraction line peak can be approximated by the Gaussian function in the same manner as the result of Figure 4. From the results of the (212) plane of Figures 4 and 5, the diffraction line peak position was determined by using various points of more than 0.7 z_{max} when background correction was made and by using various points of more than 0.8 z_{max} when background correction was omitted.

Figure 6 takes the (323) plane by CuKα radiation as the example and shows the measurement of the diffraction line peak position by using the automated X-ray diffractometer developed by us.
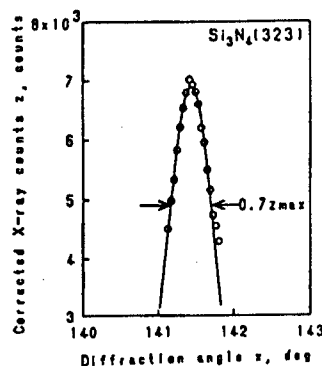
Figure 6. Peak Position Determination by the Gaussian Curve
Method With an Automated X-Ray Diffractometer

3.2 Effect of Background Correction on Stress Value

Table 2 shows the results when comparing the stress value computed from the value corrected by LPA factors after deducting the background (BG) counts from the actual measured value of X-ray counts and the stress value computed from counts corrected by LPA factors only by omitting this background correction. Moreover, the 95 percent confidence intervals for stress $\pm 1.96 \ \sigma_s$ have been obtained from the standard deviation σ_s of the stress values computed from formula (12) and they have been shown in Table 2.

Table 2. Effect of Background Correction, $S \pm 19.6 \ \sigma_s$ (MPa)

Applied stress, τ (MPa)	95% confidence limits of stress, $S \pm 1.96\sigma_S$ (MPa)			
	(323) plane		(212) plane	
	Not corrected for background	Corrected for background	Not corrected for background	Corrected for background
0	-6 ± 7	-6 ± 8	9 ± 19	4 ± 20
60	60 ± 7	63 ± 8	68 ± 18	73 ± 18
120	121 ± 7	119 ± 8	124 ± 19	125 ± 18
180	178 ± 7	179 ± 8	192 ± 19	192 ± 18
238	240 ± 7	240 ± 8	241 ± 19	249 ± 18
299	292 ± 7	289 ± 8	310 ± 22	303 ± 19

Table 2 shows that the stress values corrected for background and stress values not corrected for background coincide within the variation range shown by the confidence intervals for stress in both (323) and (212) planes. Moreover, there is no great difference seen in the confidence intervals of both stress values. Therefore, background correction does not affect the

stress values by the Gaussian curve method and can be omitted just as in the case of steel material[15] already made clear even when using silicon nitride. This not only has the advantage that measuring time is reducible by omitting background correction but it is considered to be an important conclusion on practical use as there are many cases when BG is not accurately obtainable for materials like ceramics in which many diffraction lines appear close together. Since it has become clear that background correction does not affect the stress values as seen here, only measurement results that have omitted the background correction will be shown hereafter.

In contrast to the standard deviation σ_s of the X-ray measured (323) plane stress values being 3.4~4.2 MPa, the standard deviation of the (212) plane is 8.9~11.3 MPa, about three times greater than the former. This is because as shown in Figures 2 to 5 the diffraction line by the single $K\alpha_1$ wavelength of the (323) plane is sharper than the $K\alpha$ doublet of the (212) plane.

3.3 Measurement of X-Ray Stress Constant K

Figure 7 shows the $\sin^2\psi$ diagram that has measured the peak position p of the (323) plane after applying various bending stresses to the specimen by using the bending device shown in Figure 1. Since the 95 percent confidence intervals for stress $\pm 1.96\ \sigma_p$ of the peak position were small and could not be shown in the diagram, only the minimum and maximum values have been shown. The $\sin^2\psi$ diagram for all applied stresses shows a superior linearity as shown in Figure 7.
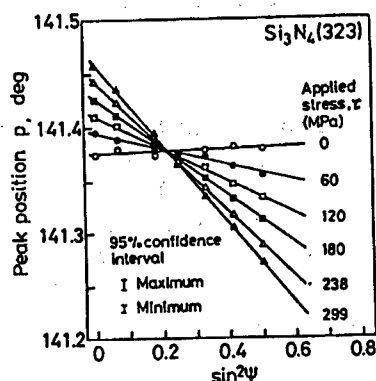
Figure 7. Sin$^2\psi$ Diagram of (323)
           Plane for Various Applied
           Stress Values
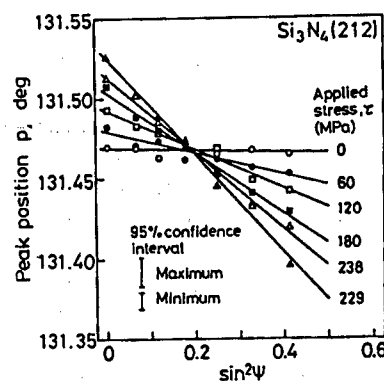
Figure 8. Sin$^2\psi$ Diagram of (212)
           Plane for Various Stress
           Values

The $\sin^2\psi$ diagram of the (212) plane measured by CrKα radiation has been shown in Figure 8 just as in Figure 7. The 95 percent confidence intervals of the peak position have been shown in Figure 8. The diffraction line of the (212) plane by CrKα radiation as known from Figures 4 and 5 is a doublet and since it is wider in comparison to the diffraction line of the (323) plane by CuKα_1 single wavelength as shown in Figures 2 and 3, the standard deviation σ_p of the peak position is greater than that of the (323) plane and thus, the 95 percent confidence intervals are also wider. However, as known from Figure 8, the diffraction line peak position of the (212) plane, also similar to the result of the (323) plane shown in Figure 7, is within the

variation range shown by confidence intervals and the $\sin^2\psi$ diagram shows a good linearity.

Figure 9 shows the relation between slope M of the $\sin^2\psi$ diagram and applied stress of diffraction line of the (323) plane obtained from Figure 7. The 95 percent confidence intervals for M are shown in this diagram. As known from Figure 9, slope M of the $\sin^2\psi$ diagram shows a good linear relation against applied stresses.
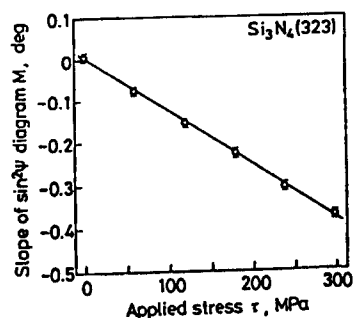
Figure 9. Slopes of $\sin^2\psi$ Diagram With Their 95 Percent Confidence Intervals for Various Applied Stresses
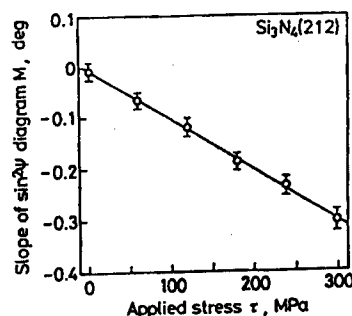
Figure 10. Slopes of $\sin^2\psi$ Diagram With Their 95 Percent Confidence Intervals for Various Applied Stresses
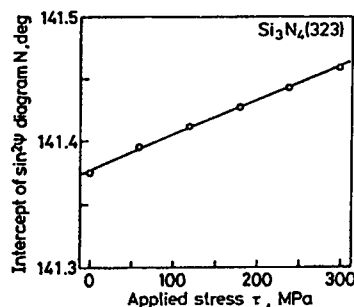
Figure 11. Intercepts of $\sin^2\psi$ Diagram With Their 95 Percent Confidence Intervals for Various Applied Stresses
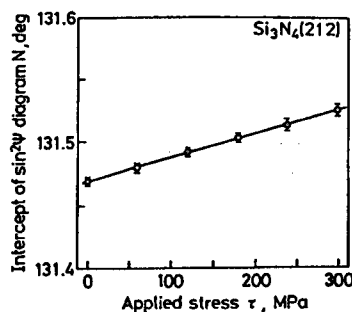
Figure 12. Intercepts of $\sin^2\psi$ Diagram With Their 95 Percent Confidence Intervals for Various Applied Stresses

Figure 10 shows the relation between slope M of $\sin^2\psi$ diagram and applied stresses of the (212) plane diffraction line shown in Figure 8. Just as in Figure 9, the 95 percent confidence intervals for various applied stresses are shown in this diagram. The relation between intercepts of the $\sin^2\psi$ diagram and applied stresses obtained from Figures 7 and 8, respectively, is shown in Figures 11 and 12. The 95 percent confidence intervals of intercept N are also shown in these diagrams. However, the circle diameter was adopted as the confidence interval size for the (323) plane of Figure 11.

Table 3. 95 Percent Confidence Limits of X-Ray Elastic Constants

		(323) plane	(212) plane
Compliances	$(1+\nu)/E$, $(10^3$ GPa$)^{-1}$	3.92 ± 0.11	3.28 ± 0.31
	ν/E, $(10^4$ GPa$)^{-1}$	8.47 ± 0.30	7.38 ± 0.66
Young's modulus E, (GPa)		325 ± 8.96	325 ± 27.4
Poisson's ratio ν		0.28 ± 0.01	0.24 ± 0.02
Stress constant K, (MPa/deg)		-779 ± 21	-1027 ± 83

The X-ray measured stress constants, compliances, and 95 percent confidence limits of X-ray elastic constants are shown in Table 3. Although the X-ray Poisson's ratio ν for the (323) and (212) planes slightly exceed the variation range shown by confidence intervals, there was no difference for the X-ray Young's modulus E. In other words, a conspicuous diffraction plane dependency against the X-ray elastic constants was not recognized in the (323) and (212) planes of silicon nitride. It is well known that there is a diffraction plane dependency between the (211) plane by CrKα radiation and (310) plane by CoKα radiation for steel material. Whether or not there is a diffraction plane dependency besides the diffraction planes mentioned above for ceramics such as silicon nitride, etc., remains a research topic for the future.

Moreover, in contrast to the relative error (standard deviation/measured value) of X-ray elastic constants E, ν, and X-ray stress constant K being 3.4~4.3 percent in the (212) plane showing the Kα doublet, all relative errors in the (323) plane using the diffraction line by single Kα$_1$ wavelength were 1.4 percent and about one-third that of the former. As seen here, measurement with a better reproducibility is possible by using the sharp diffraction line single Kα$_1$ wavelength than using the wide Kα doublet.

3.4 Residual Stress by Grinding and Lapping

Table 4 shows the results of measuring the residual stress of the surface that has been subjected to lapping after grinding under the conditions mentioned in Chapter 3. Moreover, $\sin^2\psi$ diagram of the ground surface layer has been shown as an example in Figures 13 and 14. As shown from Table 4, the compressive residual stress of 85 MPa was obtained in the ground and perpendicular directions in the measurement of the (212) plane by CrKα radiation. Upon computing the X-ray penetration depth into the specimen, it was 11 μm for the (212) plane by CrKα radiation in comparison to the effective penetration depth for the (323) plane in $\psi = 0°$ by CuKα radiation being 35 μm and the former was three times greater than the latter. As the group headed by Kishimoto[3] and the group headed by Tanaka[2] have already indicated, it can be considered that the reason why the residual stress value by CuKα and CrKα radiations differs as mentioned above is because measurement is possible to a deeper layer by CuKα radiation in comparison to measuring the ground surface layer by CrKα radiation with a shallow penetration depth.

Table 4. 95 Percent Confidence Limits $S \pm 19.6 \sigma_s$ of Residual Stress Induced by Grinding and Lapping

Surface finish	Direction of stress	(323) plane CuKα, (MPa)	(212) plane CrKα, (MPa)
Ground	Ground direction	7 ± 10	0 ± 22
	Perpendicular to ground direction	-3 ± 11	-85 ± 23
Lapped	Ground direction	3 ± 7	-2 ± 20
	Perpendicular to ground direction	7 ± 8	35 ± 21
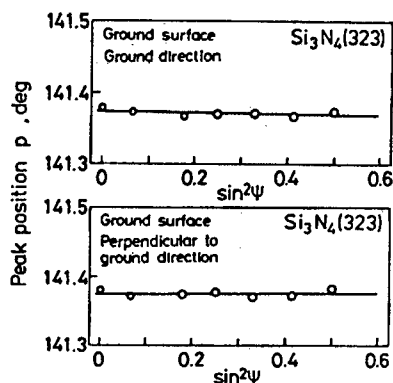
Figure 13. $\sin^2\psi$ Diagram for (323) Plane in Ground Surface Layer
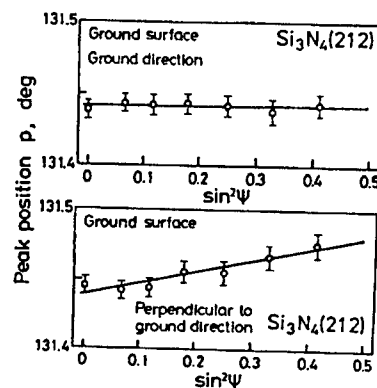
Figure 14. $\sin^2\psi$ Diagram for (212) Plane in Ground Surface Layer

As known from Table 4, a slight tensile residual stress was recognized in the ground direction and perpendicular to ground direction in the (212) plane measurement but the residual stress for others was practically zero in the lapping aspect.

Upon measuring the Gaussian curve parameter GCPa[25,26] capable of evaluating the spreading of the diffraction line under $\psi = 0$, it was 0.52° and 0.46°, respectively, in the ground and lapped surfaces of the (212) plane and that of the ground surface adopted a larger value in contrast to it, being 0.34° and 0.33°, respectively, in the ground and lapped surfaces for the (323) plane and of not much difference. This can also be considered due to the difference in the X-ray penetration depth as mentioned above. Evaluation of the ground surface layer of silicon nitride by using the diffraction line half value breadth has already been conducted by the group headed by Kishimoto,[3] however, we consider that the elastic strain of ceramics can be estimated even when using GCP in the same manner as the elastic strain measurement[24] by GCP conducted by us by using soft steel.

4. Conclusion

Together with measuring the X-ray stress and elastic constants of the (323) and (212) planes of silicon nitride, standard deviation expressing the variation size of these values generated by the statistical variation

36

inherent to the X-ray strength was obtained analytically and reliability of these measured values was studied for obtaining the basic data on X-ray stress measurement of ceramics by using the Gaussian curve method. The following are the main conclusions available.

(1) Background (BG) correction can be omitted as it practically does not affect the stress value and standard deviation.

(2) In contrast to the diffraction line of the (323) plane appearing separately by $K\alpha_1$ and $K\alpha_2$ radiations, the diffraction line of the (212) plane becomes a $K\alpha$ doublet. In comparison to the standard deviation σ_s of stress value of the (212) plane measured by X-ray being 8.9~11.3 MPa, the standard deviation σ_s of (323) plane is 3.4~4.2 MPa and about one-third that of the former. This is because the diffraction line by the single $K\alpha_1$ wavelength of the (323) plane is sharper than the $K\alpha$ doublet of the (212) plane.

(3) The X-ray elastic and stress constants of (323) and (212) planes and the confidence intervals of these values are as shown in Table 2. A diffraction plane dependency was not practically recognized in the X-ray elastic constants of these two diffraction planes.

(4) In contrast to relative errors (standard deviation/measured value) of X-ray elastic constants E, ν, and X-ray stress constants K being 3.4~4.3 percent in the (212) plane showing the $K\alpha$ doublet, all relative errors were 1.4 percent in the (323) plane using the sharp diffraction line by single $K\alpha$ wavelength and it became a small value of about one-third of that of the former.

(5) Since the diffraction line by single $K\alpha$ wavelength was not only sharper than the $K\alpha$ doublet but a wider range of the diffraction strength could be approximated by the Gaussian function as the symmetry was good, it is considered that measurements of higher accuracy are possible.

References

1.   Tanaka, et al., 3 persons, MATERIALS, Vol 36 No 407, 1987, p 792.

2.   Ibid., p 817.

3.   Kishimoto, et al., 3 persons, Ibid, p 810.

4.   Ei, Fujiwara, and Fujimoto, Ibid., Vol 37 No 413, 1988, p 204.

5.   Ibid., p 210.

6.   Kurita, et al., 4 persons, MACHINE LOGIC, Vol 54 No 500A, 1988, p 854.

7.   Ibid., 3 persons, MATERIALS, Scheduled for publication.

8.   E. Macherauch, EXP. MECH., Vol 6, 1966, p 140.

9. E. Macherauch and U. Wolfsteig, MATERIAL SCIENCE ENGINEERING, Vol 30, 1977, p 1.

10. "X-Ray Stress Measurement Method," 1981, 60, Yokendo, Edited by THE SOCIETY OF MATERIALS SCIENCE, JAPAN.

11. Taira, Arima, and Shiroyama, MATERIALS, Vol 12 No 123, 1963, p 865.

12. Taira, Hayashi, and Watase, Ibid., Vol 17 No 183, 1968, p 1151.

13. Kurita, MACHINE LOGIC, Vol 43 No 368, 1977, p 1358.

14. M. Kurita, JOURNAL OF TESTING AND EVALUATION, Vol 9 No 2, 1981, p 133.

15. Ibid., p 285.

16. Ibid., Vol 10 No 2, 1982, p 38.

17. Ibid., Vol 11 No 2, 1983, p 143.

18. Kurita, Amano, and Sakamoto, MATERIALS, Vol 31 No 345, 1982, p 609.

19. Kurita, MACHINE LOGIC, Scheduled for publication.

20. Kurita, Manuscripts of lecture theses for the 25th Symposium on X-Ray Material strength, 1988, THE SOCIETY OF MATERIALS SCIENCE, JAPAN.

21. H.P. Klug and L.E. Alexander, "X-Ray Diffraction Procedures for Polycrystalline and Amorphous Materials," John Wiley, 1974, pp 291, 635.

22. M. Kurita, "Role of Fracture Mechanics in Modern Technology," 1987, Elsevier Science Publishers B.V, p 863.

23. Kurita, MACHINE LOGIC, Scheduled for publication.

24. Kurita, et al., 3 persons, MACHINE LOGIC (A Edition), Vol 52 No 482, 1986, p 2429.

25. Kurita, PLASTICITY AND MACHINING, Vol 26 No 295, 1985, p 869.

26. M. Kurita, "Advance in X-Ray Analysis," Vol 31, Plenum Publishing, 1988, p 277.

X-Ray Measurement of Residual Stress Caused by Machining in Sintered Alumina Ceramics

[Article by Yoshio Miyoshi and Keiji Ogura, Faculty of Engineering Science, Osaka University, Toyonaka; from the 25th Symposium on X-Ray Studies on Mechanical Behavior of Materials held 21-22 July 1988]

[Text] 1. Introduction

Fine ceramics are materials excelling in heat resistance, corrosion resistance, and wear resistance and many products have been developed by taking full advantage of these characteristics. Since fine ceramics revealing strength, i.e., high strength in high temperatures in addition to these characteristics, have appeared in recent years, their use has been attempted on many machine parts, such as those for processing machines, forming machines and steel making, including engines such as gas turbines and diesel engines. Moreover, their uses are being further expanded by the progress of ceramics coating and junction technology on these.

However, since ceramics for machine parts are subjected to high densification by sintering, they are also subjected to great contraction in the sintering process. Moreover, some machining or other is conducted on ceramics to obtain dimensional precision to make them usable as machine parts. A residual stress is induced into ceramics by these processes. It has also been indicated that such a residual stress exerts a vital effect on crack generation and strength, such as fracture toughness value, etc. of these ceramics and although the application of various methods has been studied in residual stress measurement as well, there is still not an effective means for residual stress measurement of ceramics and the application of the X-ray stress measurement method is currently being tested as the most promising method.[1-13] However, differing from the case of steel material, the characteristic X-rays and diffraction planes to be used differ according to materials in the X-ray stress measurement of ceramics and since there are diffraction planes with the diffraction peak available and not available according to production methods even when using the same material, there are still many problems that should be studied.

Together with obtaining the X-ray elastic constants on atmospheric sintered alumina ceramics of different purity, residual stress measurement of machining, such as grinding and lapping, was conducted and results of studying on the purity effect for these will be reported here.

2. Experiment Method

2.1 Material Under Test and Specimen

The material under test is an atmospheric sintered square alumina ceramic with one side of 100 mm and the depth of 10 mm and there are three types of materials under test with a purity of 92.0 percent, 99.5 percent, and 99.99 percent. The specimen shown in Figure 1 is of a tanzaku shape having a rectangular section cut to approximate size from the material under test by a diamond cutter. Three types of specimens prepared to prescribed dimensions by providing grinding only and providing lapping after grinding were prepared. The grinding and lapping conditions are shown in Tables 1 and 2, respectively.
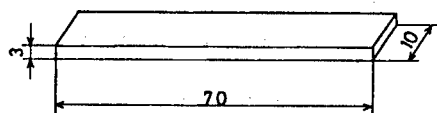
Figure 1. Shape and Dimension of Specimen

Table 1. Grinding Condition

Grindstone	SD 140
Rotational frequency	1,600 rpm
Feed speed	18~20 m/min
Grain depth of cut	6 μm/pass

Table 2. Lapping Condition

Grain	20 μm GC
Time	60 min

2.2 Determination of X-Ray Stress Measurement Conditions and Diffraction Angles

The X-ray stress measurement was conducted by the $\sin^2\psi$ method and measurement was made on the (220) plane by CrKα radiation for the characteristic X-ray which is regularly used in general steel materials. Moreover, other conditions have been arranged and are shown in Table 3. The diffraction angle 2 θ was determined by half value breadth and the X-ray incident angle ψ_0 was made of 11 points with intervals of 5° in the range from -10° to +40°.

Table 3. Details of the X-Ray Stress Measurement

Characteristic X-ray	CrKα
Diffraction plane	(220)
Tube voltage	30 kV
Tube current	10 mA
Filter	V
Divergent angle	0.32
Scanning speed	1 deg/min
Time constant	10 sec
Irradiated area	1 x 10 mm^2

2.3 Determination of Mechanical Elastic Constants

The mechanical elastic constants were obtained prior to determining the X-ray elastic constants. Measurement was conducted by using a specimen provided with grinding, attaching a strain gauge on the front and back sides of the specimen and by means of the four-point bending test. Moreover, the bulk density of various specimens was also measured.

2.4 Determination of X-Ray Elastic Constants

Since the strain measurement by X-ray obtains the strain from the change of the lattice plane space and computes the stress by multiplying the elastic constant to this, it is necessary to use that of the measuring lattice plane for the constant.

The computation formula of X-ray stress σ_x is given by the following formula.

$$\sigma_x = -\{E \cdot Cot\theta_0/2(1 + \nu)\} \cdot (\partial 2\theta/\partial Sin^2\Psi) = K \cdot M \qquad (1)$$

Here,
$$K = -\{E \cdot Cot\theta_0/2(1 + \nu)\}$$
$$M = \partial 2\theta/\partial Sin^2\Psi$$

Moreover, K is called the X-ray stress constant and M is the slope of the 2θ $sin^2\psi$ diagram.

Supposing that the X-ray stress σ_x is equal to the mechanical stress σ_M in formula (1), the following relation is available when substituting $\sigma_x = E_M \cdot \varepsilon_x$ (E_M is the mechanical Young's modulus, ε_x is the mechanical strain by the strain gauge) and differentiating both sides on ε_x.

$$K = E_M/ \partial M / \partial \varepsilon_x \qquad (2)$$

Therefore, the X-ray stress constant K applies various mechanical strains to the specimen, obtains the 2θ - $sin^2\psi$ diagram in the application stage and it can be determined from the relation between slope M and ε_x. Moreover, the X-ray elastic constant can be computed by the following formula from the K value and diffraction angle θ_0 of the distortionless state.

41

$$E/1 + \nu = -2K \cdot \mathrm{Tan}\theta_0 \qquad (3)$$

A ground specimen was used in this experiment and a mechanical strain was applied by the four-point bending device and the strain ε_x was changed in four stages between 0 and 400 x 10^{-6}. The strain ε_x was obtained from strain gauges attached on the front and back sides of the specimen. Moreover, the value of θ_0 = 7 computed by using the lattice constants (a = 4.759 Å, c = 12.99 Å) of alumina was used for the diffraction angle of the distortionless state.

3. Experiment Results and Discussion

3.1 Mechanical Elastic Constant

Figure 2 has shown an example of the stress-strain curve that has been obtained when obtaining the mechanical elastic constant on a specimen with 92 percent purity. It is known from the diagram that a good linear relation exists between the stress and strain in both processes of load application and load removal. This relation was also the same in specimens with other purities.
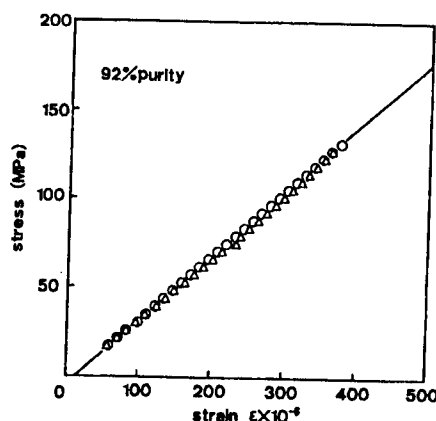
Figure 2. Stress-Strain Curve

Table 4 shows the mean value of mechanical Young's modulus E_M of alumina ceramics of various purities obtained beforehand on the strain application and strain removal procedures of the stress-strain curve. Although there is a tendency that E_M of alumina becomes greater as the purity becomes higher, E_M is of practically the same value as that of 99.5 percent purity even when the purity becomes 99.99 percent and Young's modulus does not always rise when it reaches special high purity. The mechanical properties of ceramics are of course dependent on purity but since they are also greatly dependent on porosity, the bulk density has been obtained and is shown in Table 4. The higher the purity, the higher the bulk density and that with a purity of 99.99 percent is likewise the highest. As seen here, the mechanical Young's modulus of alumina ceramics increases as the purity and bulk density become higher, however, it seems that this value approaches an approximately fixed value when the purity and bulk density become more than a certain value.

Table 4. Mechanical Elastic Constant and Density

Purity (percent)	Young's modulus E_M (GPa)	Density g/cm^3
92.00	357	3.63
99.50	390	3.90
99.99	389	3.97

3.2 X-Ray Elastic Constant

Figure 3 shows an example of the 2θ - $\sin^2\psi$ diagram of various strain applying stages obtained while applying a mechanical strain by the bending device on specimens with 92 and 99.5 percent purity prior to computing the X-ray elastic constant. It is known from Figure 3 that a good linear relation exists between 2θ and $\sin^2\psi$ in each load stage. A specimen with a ground surface was used in this experiment but ψ splits, etc., were not recognized and it was known than an X-ray stress measurement with an accuracy by no means inferior to metallic materials was possible by CRKα radiation in ceramics.

(a) 9 2 %
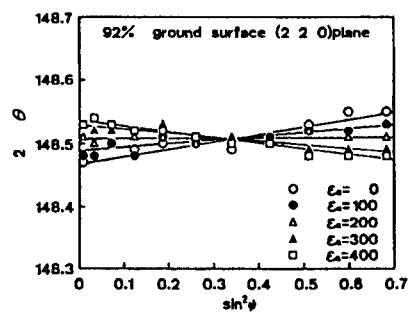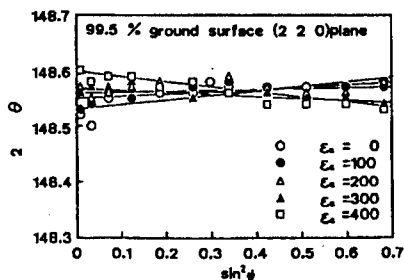
(b) 9 9.5 %

Figure 3. 2θ-$\sin^2\psi$ Diagram for Ground Surface
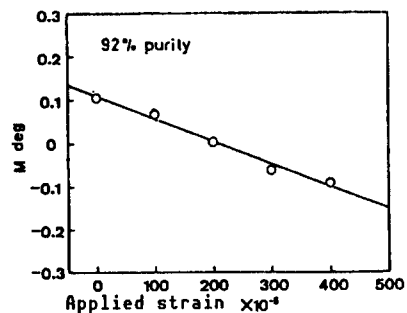
(a) 9 2 %
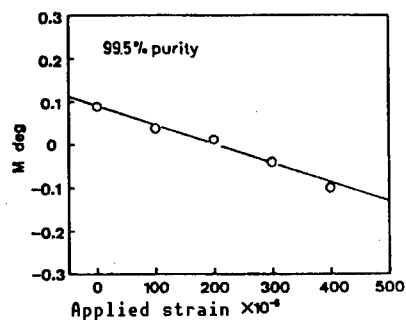
(b) 9 9.5 %

Figure 4. Relation Between Slope in 2θ-$\sin^2\psi$ Diagrams and Applied Strain

Figure 4 shows an example that has plotted slope M of the $\sin^2\psi$ diagram previously obtained against the mechanical strain ε_x for those with the

purity of 92 and 99.5 percent. Moreover, value M is the mean value of values obtained in measurements conducted three times. It is known from the diagram that a good linear relation exists between slope M and ε_x of $\sin^2\psi$ diagram. The relation between these was also the same for that of 99.99 percent purity.

Table 5 shows the X-ray elastic constants and X-ray stress constants computed from formulas (2) and (3) by using the mechanical Young's modulus E_M, slope $\partial_M/\partial\varepsilon_x$ of M-ε_x relation and diffraction angle θ_0 of distortionless state. These values, as in the mechanical Young's modulus, become larger with the rise of purity and increase of bulk density and they coincide well with the results obtained by the group headed by Tanaka.[11]

Table 5. X-Ray Elastic Constant and X-Ray Stress Constant

Purity (percent)	Elastic constant $E/(1 + \nu)$ (GPa)	Stress constant K (MPa/deg)
92.00	304	-743
99.50	349	-855
99.99	381	-933

3.3 Residual Stress by Machining

We tried measurement of the residual stress of the sintered surface condition as well as the machine processed surfaces, such as the cut, ground, and lapped surfaces of alumina ceramics, in this experiment and the $\sin^2\psi$ diagram obtained in this case for all purities is shown in Figure 5. It is known from this diagram that a good linear relation exists just as in the previously shown ground surface.

Table 6 shows the residual stress values of the sintered, cut, ground, and lapped surfaces according to purities computed by using the previously obtained X-ray stress constants. Moreover, the measuring direction of processed surfaces is in two directions: parallel direction (longitudinal direction:ground direction) of specimen and perpendicular direction of specimen.

The residual stress of the sintered surface shown in Table 6 is a compression in those with low purity but the compression reduces as the purity becomes higher and the residual stress changes to a tension. However, all of these absolute values have become smaller than those introduced by machining.

On the other hand, the residual stress of machined surfaces such as cutting, ground, and lapped surfaces are not dependent on purity and are all compressions and they also coincide with results up to now[3,9] and results of the ceramics.[4,6,7,12-14] However, the value of the cross section is the greatest; particularly in perpendicular direction. This is considered due to the cutout direction of the specimen coinciding with the perpendicular direction. Moreover, the residual stress by purity tends to become larger
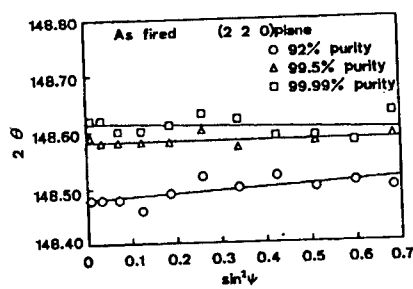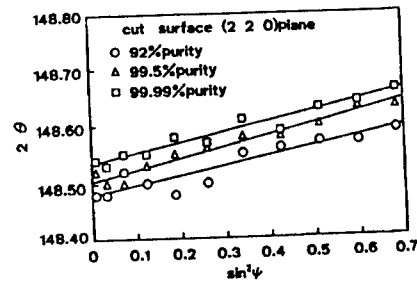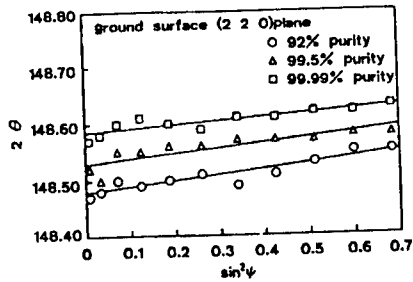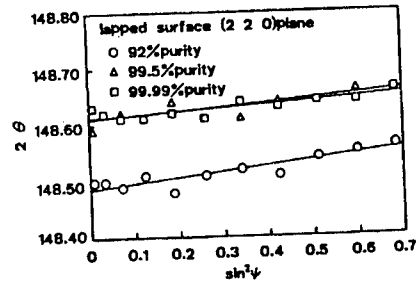
Figure 5. 2θ-$\sin^2\psi$ Diagram

Table 6. Relation Between Residual Stress and Surface Condition

Purity (%)	Surface condition	Residual stress (MPa)	
		Parallel direction	Perpendicular direction
9 2.0 0	As fired Cut Ground Lapped	- 3 8 ± 1 6 -1 2 1± 1 8 -7 7± 1 2 6 9± 1 3	.... -1 6 3± 1 6 9 8± 1 4 -8 4± 1 7
9 9.5 0	As fired Cut Ground Lapped	2± 1 0 -1 6 7± 1 3 -7 6± 1 8 -6 0± 1 8	.... -2 3 7± 2 1 -5 8± 1 2 -7 7± 2 9
9 9.9 9	As fired Cut Ground Lapped	1 7± 5 4 -1 6 9± 1 5 -5 6± 1 7 -5 0± 1 4	.... 1 9 1± 2 1 -6 5± 2 2 6 9± 1 9

in those with higher purity. As seen here, the residual stress of the cutting plane has reached the great value of 110~240 MPa, however, this residual stress reduces by about 50~75 percent when grinding has been provided on this surface and it seems that the difference caused by the directional property and purity of the value also reduces. Moreover, the residual stress further reduces when lapping is provided on this ground surface but this reduction value is small and there are also those that practically do not change. Although a residual stress of a large

compression is induced when cutting is provided on alumina as mentioned above, it has become clear that practically all of these residual stresses are freed and removed by grinding and lapping after cutting. However, since the residual stress values by machining will differ according to processing conditions and removal amount, it is really important to conduct actual measurements each time.

4. Conclusion

Together with conducting measurement of X-ray elastic constants and residual stress induced at firing and machining conditions on alumina ceramics with different purities, the effects of purity and bulk density against these measured values were studied. It resulted as follows in summarizing the results.

(1) X-ray stress measurement of alumina ceramics has become possible for the (220) plane by CrKα radiation and the practically same measurement accuracy as in steel material is expectable when multipoint incidence is used.

(2) The higher the purity and bulk density, the bigger the mechanical Young's modulus of alumina and it seems to achieve an almost fixed value when purity becomes more than a certain value.

(3) The higher the purity and bulk density, the greater the X-ray elastic constants of alumina.

(4) A compressive residual stress generates on alumina when machining is provided and this residual stress value is the greatest at cutting. However, this residual stress reduces by the grinding and lapping provided later.

In conclusion, we express our deep gratitude to the Nihon Cement Co., Ltd., that has offered us materials for the execution of this experiment and to Haruhiko Yamamoto rendering us his cooperation in this experiment.

References

1. F.F. Lange, et al., 2 persons, JOURNAL OF AMERICAN CERAMIC SOCIETY, Vol 66, 1983, p C16.

2. Ibid., ADVANCED X-RAY ANALYSIS, Vol 27, 1983, p 221.

3. Tanaka, et al., 2 persons, MATERIALS, Vol 35, 1986, p 749.

4. Ei, et al., 2 persons, Manuscripts of lecture theses for the 23d Symposium on X-Ray Material Strength, 1986, p 203.

5. Tanaka, et al., 3 persons, MATERIALS, Vol 36, 1987, p 792.

6. Kishimoto, et al., 3 persons, Ibid., p 810.

7. Tanaka, et al., 3 persons, Ibid., p 817.

8. Miyoshi and Ogura, THE SOCIETY OF MATERIALS SCIENCE, JAPAN, printed manuscripts for the 36th Session Scientific Lecture, 1987, p 202.

9. Ibid., Manuscripts of lecture theses for the 24th Symposium on X-Ray Material Strength, 1987, p 186.

10. Yoshioka, Ibid., p 191.

11. Tanaka, et al., 2 persons, Ibid., p 196.

12. Tanaka, et al., 3 persons, Ibid., p 208.

13. Tanaka, et al., 2 persons, Ibid., p 214.

14. Ei, et al., 2 persons, Ibid., p 219.

X-Ray Residual Stress Measurement of Zirconia-Alumina Composite Ceramics

[Article by Keisuke Tanaka, Department of Engineering Science, Kyoto University, Kyoto; Yuji Yamamoto and Noriaki Mine, Graduate School, Kyoto University, Kyoto; Kenji Suzuki, Faculty of Education, Niigata University, Niigata; Takayuki Kurimura, Mitsubishi Heavy Industries, Ltd,; Takasago and Heizaburoh Nakagawa, Japan Fine Ceramics Center, Nagoya; from the 25th Symposium on X-Ray Studies on Mechanical Behavior of Materials held 21-22 July 1988]

[Text] Residual stresses on the ground or lapped surface of zirconia-alumina composite materials were measured by the X-ray method. Diffraction from plane Al_2O_3 (146) by $CuK\alpha$ radiation and from plane Al_2O_3 (1.0.10) and ZrO_2 (133) by $CrK\alpha$ radiation were used for stress measurement. The stress constants and X-ray elastic constants were determined for the three diffraction planes. The X-ray elastic constants were calculated on the basis of the Kroener model and were compared with the experimental results. The effect of grinding and lapping conditions on the finished surface were discussed on the bases of the residual stress measured by X-ray diffraction.

1. Introduction

Ceramics are brittle material and it is expected that the thermal strain at sintering and residual stress induced by machining such as grinding, etc., greatly affect the material strength. The X-ray stress measurement method has attracted attention recently as an effective means for the nondestructive measurement method of residual stress and actual measurement results of alumina (Al_2O_3),[1,2] zirconia (ZrO_2),[3] silicon nitride (Si_3N_4),[4,5] and silicon carbide (SiC)[6] have been reported. Gaining an understanding on the actual state of these residual stresses is contributing to the improvement of production and processing methods, material evaluation, and reliability improvement of ceramics.

The zirconia-alumina composite ceramic ($ZrO_2/40wt\%Al_2O_3$) which is one of the representative composite ceramics with a high toughness has been taken up in this experiment and the X-ray elastic constants were determined by experiments. The $CrK\alpha$ and $CuK\alpha$ radiations were used for the characteristic X-rays. The diffraction planes used in the experiment were the zirconia

phase (133) plane and alumina phase (1.0.10) plane in CrKα radiation and the alumina phase (146) plane in CuKα radiation. The experiment results were compared with the theoretical computation by the Kroener method. Then, the X-ray stress measurement of various zirconia and alumina phases was conducted on materials that had been heavy ground and light ground by changing the cutting depth of the #200 diamond grindstone, materials that had been precisely ground by the #600 diamond grindstone, and materials provided with lapping.

2. Experiment Method

2.1 Material and Specimen

The material used in a composite ceramic which has atmospherically sintered the powder of zirconia (ZrO_2) containing 3 mole percentage of yttria and alumina (Al_2O_3), and Al_2O_3 is contained by 40 weight percentage. It reached 50 volume percentage, respectively, when computing the volume percentage by using the theoretical density 6.00 g/cm^3 of tetragonal zirconia and the theoretical density 3.99 g/cm^3 of trigonal alumina. Both the zirconia and alumina phases are of equi-axed grains of about less than 1 μm size and these grains are uniformly mixed.

The specimen is a square bar of 55 mm length having a rectangular section of 9.5 mm width and 4.0 mm height. Four types of specimens, two types that were ground in the longitudinal direction of the 9.5 x 55 mm^2 surface with the #200 diamond grindstone by changing the cutting depth, the type ground by the #600 diamond grindstone, and the type that had been lapped, were prepared for studying the relation between the surface processed condition and residual stress. Data of depth setting, normal force, tangential force, and surface roughness have been arranged in Table 1. Moreover, the mean center line roughness of those that were lapped was 0.009 μm. The chamfering of 0.2 μm has been provided in the longitudinal direction of the surface provided with surface processing.

Table 1. Grinding Conditions of Zirconia-Alumina Composite Ceramics

Grinding type	Grinding wheel	Depth setting Δ (μm)	Normal force F_n (N/mm)	Tangential force F_t (N/mm)	Surface roughness R_a (μm)	
					Parallel direction	Perpendicular direction
Heavy grinding	#200	25	18.5	4.8	0.318	0.708
Light grinding	#200	5	5.6	1.1	0.331	0.610
Fine grinding	#600	1	1.6	0.2	0.093	0.127

Mechanical elastic constants E_M were obtained from the linear reaction between load and stress by attaching strain gauges to the specimen and conducting a four-point bending (bending within longitudinal plane) test. The mean value of measurements made 12 times was 282 GPa and the Poisson's ratio was 0.266.

2.2 Destination of X-Ray Observation Conditions, Diffraction Plane, and Angle

The diffraction diffractometer (Shimadzu XD-3A) was used in place of the parallel beam method for stress measurement in the measurement of the X-ray profile. The X-ray conditions for stress measurement have been arranged in Table 2.

Table 2. X-Ray Conditions for Stress Measurement

Method		Parallel beam method		
Characteristic X-ray		$CuK\alpha$	$CrK\alpha_1$	$CrK\alpha$
Diffraction plane		Al_2O_3(1 4 6)	Al_2O_3(1.0.10)	ZrO_2(1 3 3)
Diffraction angle	(deg)	136.30	135.03	152.35
Filter		Ni	V	V
Tube voltage	(kV)	40	40	40
Tube current	(mA)	40	40	30
Divergent angle	(deg)	0.64	0.64	0.64
Irradiated area (mm^2 rectangle)		4 x 9.5	4 x 9.5	2 x 9.5
Scanning speed	(deg/min)	1	1	1
Preset time	(sec)	2	2	1

In this research, X-ray stress measurement was conducted by using $CuK\alpha$ radiation (146) plane and $CrK\alpha$ radiation (1.0.10) plane for the alumina phase and the $CrK\alpha$ radiation (133) plane for the zirconia phase. The depth direction distribution of the residual stress is known from the fact that the penetration depth against the (146) plane is deeper in comparison to the (133) and (1.0.10) planes as mentioned later. Moreover, since the X-ray penetration depth against the zirconia phase (133) plane and alumina phase (1.0.10) plane is almost the same, the phase stress at this depth can be evaluated.

Alumina is a trigonal and the lattice constants are a = 0.476 nm and c = 1.299 nm. Moreover, zirconia is a tetragonal and the lattice constants are 1 = 0.510 nm and c = 0.519 nm. The lattice constants of alumina are the values of JCPDS card No 10-173 and they coincided with the actual measured values. On the other hand, zirconia is of the actual measured values and it is the same as the case of HIP zirconia[3] containing 3 mole percentage of yttria. Moreover, the monoclinic was less than 1 percent when the lapped material was annealed in 1,200°C for 2 hours.

The diffraction angle for X-ray stress measurement was determined as the angle of the midpoint at the half-height of the profile,i.e., by the half value method for (133) and (146) planes and the diffraction width mid-point angle at the 90 percent height of the profile for the (1.0.10) plane. A 2θ-$\sin^2\psi$ diagram based on the ψ fixing method of 10 points notched at intervals of 5° from 0° to 45° has been drawn for the X-ray incident angle.

2.3 X-Ray Penetration Depth

When an X-ray hits against a material, a portion of the X-ray penetrates and a portion is absorbed.[9] It becomes as shown in the following formula when I_x is made the X-ray strength penetrating the material.

$$I_x = I_0 \exp(-\mu x) \tag{1}$$

Here, I_0 is called the strength and linear absorption coefficient of the incident X-ray. The value μ/p which has divided this μ by the material density is the mass absorption coefficient. The mass absorption coefficient of compounds and mixtures is available by conducting proportional allocation of the mass absorption coefficient of various components by mass.[7] When obtaining the mass absorption coefficient of ceramics in this research by using the atomic weight and mass absorption coefficient of O, Al, and Zr, it became 75 cm^2/g in CuKα radiation and 223 cm^2/g in CrKα radiation. Moreover, the theoretical density of this ceramic is 4.99 g/cm^3 and when obtaining the linear absorption coefficient μ from this value, it became 375 cm^{-1} in CuKα radiation and 1,115 cm^{-1}.

The specimen surface penetration depth of X-ray changes by the angle formed by the normal direction of specimen surface and the diffraction plane normal. The depth of diffraction line strength I of incident X-ray with the strength of I_0 becoming $I = I_0/e$ is defined as the penetration depth here. The X-ray penetration depth for $\sin^2\psi$ of various diffraction planes is shown in Figure 1. The penetration depth of CuKα radiation is about 7~12 μm and is about 5~8 μm deeper than that of CrKα radiation.
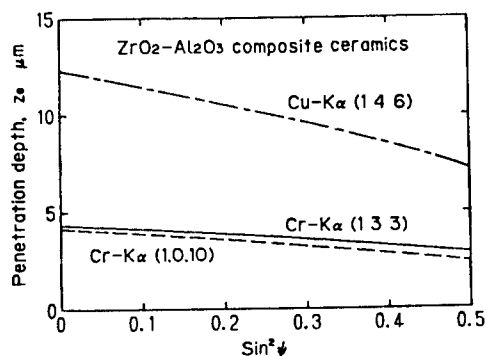
Figure 1. X-Ray Penetration Depth Versus $\sin^2\psi$

2.4 Measuring Method of X-Ray Elastic Constants

The four-point bending device was used for measurement of X-ray elastic constants. Strain gauges were attached to the specimen in this experiment and the 2θ-$\sin^2\psi$ diagram was obtained by the set various applied strains ε_a and stress constant K was determined by the change of slope M against applied strain ε_a. The relation between the stress σ_x in the material and applied strains ε_a that are the parameters of this research can be expressed as follows by using the mechanical elastic constants.

51

$$\sigma_x = E_M \ (\varepsilon_a + \varepsilon_r) \tag{2}$$

Here, ε_r is the residual elastic strain possessed by the measured material. Just as up to the preceding chapter, the relation among the stress constant K, slope M of $\sin^2\psi$ diagram, and stress σ_a is expressed by the following formula:

$$K = 1/(\partial M/\partial \sigma_x) = -E/2(1 + \nu) \cdot \cot\theta \tag{3}$$

The stress constant K is available from formulas (2) and (3) by the following formula:

$$K = E_M/ \ (\partial/\partial \varepsilon_a) \tag{4}$$

2.5 Theoretical Computation of X-Ray Elastic Constants by Kroener Model

The X-ray elastic constants are available as follows by the Kroener model. First of all, according to the Reuss model, the following relation exists between strain ε_{ij} and load stress $\sigma_{kl}{}^A$ within a single crystal of a polycrystalline substance with a fixed stress.

$$\varepsilon_{ij} = S_{ijkl} \ \sigma_{kl} \tag{5}$$

Here, S_{ijkl} is the elastic compliance of the single crystal. On the other hand, the Kroener model presents the following model due to the constraint existing mutually among the crystals.

$$\varepsilon_{ij} = (S_{ijkl} + t_{ijkl}) \ \sigma_{kl}{}^A \tag{6}$$

Here, t_{ijkl} is the added item by the constraint among crystals and is available by the single crystal compliance and mechanical elastic constant by using the Eshelby theory. The X-ray elastic constants of various trigonal diffraction planes are given by the following formulas by using the matrix display t_{ij} of t_{ijkl}.

$$
\begin{aligned}
(1 + \nu)/E = {} & S_{11} - S_{12} + (2t_{11} - t_{12} - t_{13})/2 \\
& -5t_{11} - t_{12} - 4t_{13} - t_{31} + t_{33} - 3t_{44})w^2/2 \\
& +3(t_{11} - t_{13} - t_{31} + t_{33} - t_{44})w^4/2 \\
& +3(t_{14} + t_{41})vw(3u^2 - v^2)/2)
\end{aligned}
\tag{7}
$$

$$
\begin{aligned}
-\nu/E = {} & S_{12} + (t_{12} + t_{13})/2 \\
& +(t_{11} - t_{12} - 2t_{13} + t_{31} + t_{33} - t_{44})w^2/2 \\
& -(t_{11} - t_{31} - t_{13} + t_{33} - t_{44})w^4/2 \\
& -(t_{14} + t_{41})vw(3u^2 - v^2)/2
\end{aligned}
\tag{8}
$$

Here, S_{11} and S_{12} are polycrystalline compliances.

$$S_{11} = 1/E \tag{9}$$

$$S_{12} = -\nu/E \tag{10}$$

Moreover, the relation between the direction cosines (u,v,w) of plane normal and diffraction plane index (hkl) is given by the following formula:

$$(u,v,w) = 2/[4\lambda^2(h^2+hk+k^2)+3l^2]^{\frac{1}{2}}$$
$$\cdot (3^{\frac{1}{2}}\lambda h/2,\ \lambda k+\lambda h/2,\ 3^{\frac{1}{2}}\ l/2) \tag{11}$$

Here, λ is the lattice constant ratio c/a of the trigonal c-axis and a-axis.

Values experimentally obtained by the four-point pending method were used for the mechanical elastic constants (E, ν) in this research. Moreover, t_{ii} was obtained by using the mechanical elastic constant and elastic stiffness of alumina single crystal.

2.6 Measurement of Residual Stress

The residual stress of these types of grinding planes and lapping planes was measured. Measurements were made in three directions, the grinding plus direction ($+\psi$), grinding minus direction ($-\psi$), and grinding perpendicular direction for the #200 heavy ground surface and measurements were made in two directions, the grinding plus direction ($+\psi$) and grinding perpendicular direction for other grinding surfaces. Measurement was made only in the longitudinal direction for the lapped surface. Measurement was based on slope angles of 10 points that had been notched at 5° intervals between $\psi = 0°$ to 45°. Moreover, measurements were made three times for each case and the mean diffraction angle was adopted for the value at each slope angle. The residual stress is obtained by the following formula by using the X-ray stress constant K and slope M of $2\theta-\sin^2\psi$ diagram.

$$\sigma_r = K\ (M +\ _\Delta M) \tag{12}$$

Here, $_\Delta M$ is the 68.3 percent confidence limits by t distribution for M where least squares approximation is used.

3. Experiment Results and Discussion

3.1 X-Ray Elastic Constants

Lapped materials were used for the measurement of X-ray elastic constants. Measurement of applied strain ε_a was conducted in five stages of 0, 400, 800, 1,200, 1,600 x 10^{-6}. Measurements were repeated five times in $\varepsilon_a = 0$, 1,600 x 10^{-6} and three times in $\varepsilon_a = 400$, 800, and 1,200 x 10^{-6} and the mean value of measured values in each X-ray incident angle was made the diffraction angle of the incident angle. The $2\theta-\sin^2\psi$ diagram on $\varepsilon_a = 0$, 800, 1,600 x 10^{-6} of zirconia (133) plane has been arranged in Figure 2 and that of alumina (146) plane has been arranged in Figure 3. Linear approximation of these is possible and the regression straight line by the least squares method is shown in the diagram. Moreover, the three straight lines almost crossed at one point. Slope M of these straight lines reduces with the increase of applied stress ε_a. The reason why it does not become M = 0 when $\varepsilon_a = 0$ is because the specimen possesses the initial strain induced at sintering.
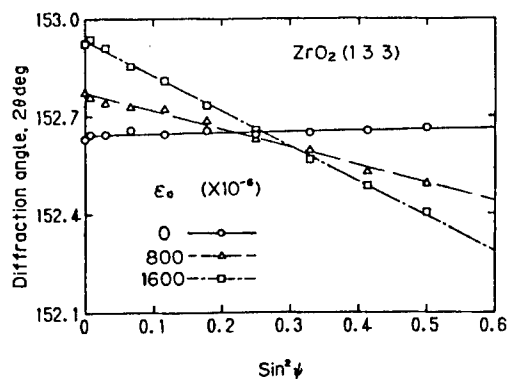
Figure 2. 2θ Versus $\sin^2\psi$ for ZrO_2 (1 3 3)
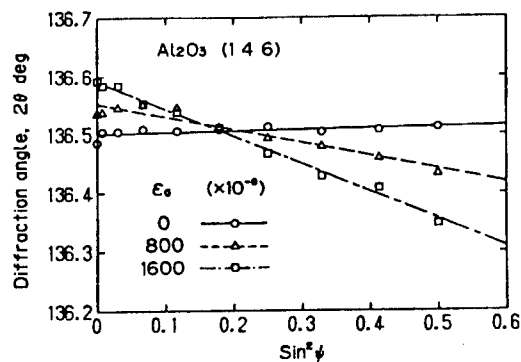
Figure 3. 2θ Versus $\sin^2\psi$ for Al_2O_3 (1 4 6)
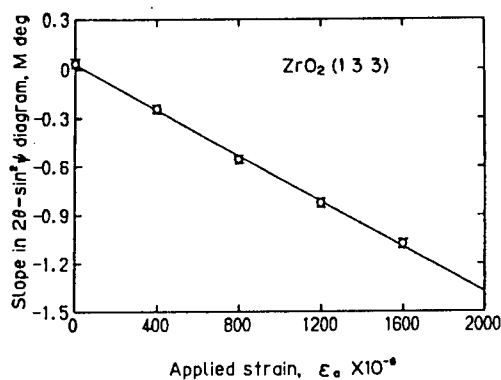
Figure 4. Slope Versus Applied Strain for ZrO_2 (1 3 3)
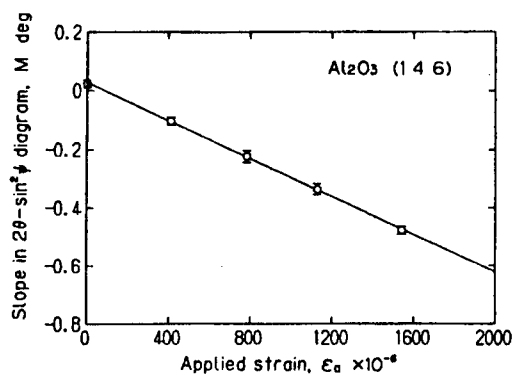
Figure 5. Slope Versus Applied Strain for Al_2O_3 (1 4 6)
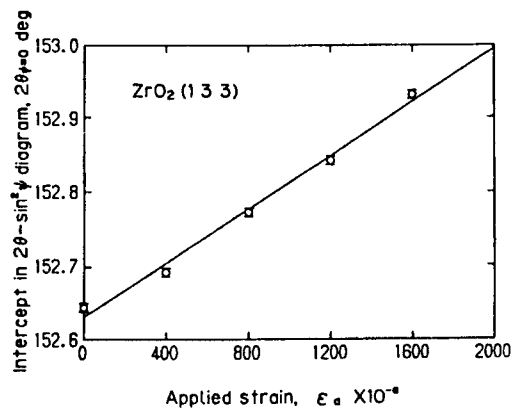
Figure 6. Intercept Versus Applied Strain for ZrO_2 (1 3 3)
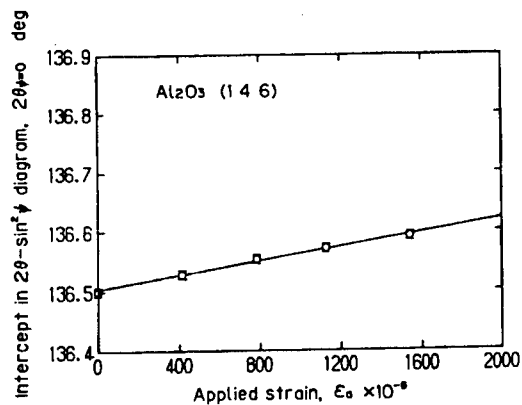
Figure 7. Intercept Versus Applied Strain for Al_2O_3 (1 4 6)

54

The relation between M and ε_a on the (133) and (146) planes is as shown in Figures 4 and 5, respectively. Moreover, the relation between the applied strain ε_a and the intersecting point (2θ ψ = 0) of 2θ axis (y-axis) with the regression straight line in the 2θ-$\sin^2\psi$ diagram is as shown in Figures 6 and 7, respectively.

Linear approximation is possible for both diagrams and the regression straight line was shown in the diagrams. Moreover, the longitudinal rod in the diagram shows the 68.3 percent confidence limits by the minimum squares approximation of the 2θ-$\sin^2\psi$ diagram on each ε_a. It can be said that the confidence limit width is small and the measuring accuracy is high in all cases.

The X-ray stress constant K obtained from the M-ε_a relation slope by using the formula (5.5), $(1 + \nu)/E$ obtained by using the diffraction angle and X-ray stress constant K shown in Table 2 just as in the procedure up to the preceding chapter, ν/E obtained by the rate of change of 2θ ψ = 0 against ε_a and the 68.3 percent confidence limits of $(a + \nu)/E$ and ν/E have been arranged and shown in Table 3. Moreover, results of computing E and ν from this are also shown in Table 3 at the same time.

Table 3. X-Ray Elastic Constants and X-Ray Stress Constants of Composite Ceramics

Diffraction plane	X-ray compliance		X-ray elastic constant			Stress constant
	$(1+\nu)/E$ $(10^{-3}/GPa)$	ν/E $(10^{-4}/GPa)$	$E/(1+\nu)$ (GPa)	E (GPa)	ν	K (MPa/deg)
Al_2O_3 (1 4 6)	4.03±0.05	7.35±0.42	248	304	0.22	-869
Al_2O_3 (1.0.10)	3.85±0.17	6.24±0.85	260	310	0.19	-937
ZrO_2 (1 3 3)	5.36±0.33	13.92±2.39	187	252	0.35	-401

Table 4. X-Ray Elastic Constants and X-Ray Stress Constants of Single Phase Ceramics

Diffraction plane	X-ray compliance		X-ray elastic constant			Stress constant
	$(1+\nu)/E$ $(10^{-3}/GPa)$	ν/E $(10^{-4}/GPa)$	$E/(1+\nu)$ (GPa)	E (GPa)	ν	K (MPa/deg)
Al_2O_3 (1 4 6)	3.08±0.14	7.53±1.43	324	416	0.28	-1132
Al_2O_3 (1.0.10)	3.19±0.62	7.14±1.91	314	405	0.29	-1129
ZrO_2 (1 3 3)	7.76±0.27	18.55±1.06	129	169	0.31	-277

In comparing the numerical values of Table 3 with the mechanical values, we find that the alumina phase is higher and the zirconia phase is lower than the mechanical values on elastic constant E and the alumina phase is lower and the zirconia phase is higher than the mechanical values on Poisson's ratio ν. Moreover, the X-ray elastic constant and Poisson's ratio of single-phase ceramics have been respectively obtained for each diffraction plane and the previously reported experimental values on 99.9 percent Al_2O_3[1,2]

and 3 mole percentage Y_2O_3-ZrO_2[3] subjected to hot isostatic pressing (HIP) have been arranged and shown in Table 4. When comparing with these values, we find that the elastic constant E of ceramics is smaller in the alumina phase than the single phase and it is greater in the zirconia phase than the single phase. On the other hand, the zirconia phase which was greater on Poisson's ratio when comparing the two became slightly greater than the alumina phase became slightly smaller in reverse.

Table 5. Elastic Constants Calculated by Kroener Model

| Elastic constants | Diffraction plane | |
	(1 4 6)	(1.0.10)
Young's modulus, E (GPa)	360	356
Poisson's ratio, ν	0.23	0.24
E/(1 + ν) (GPa)	290	289

Values theoretically computed by substituting the mechanical elastic constants obtained by experiment in the Kroener model are shown in Table 5. The theoretical values of various diffraction planes reached larger values than actual measured values. This fact suggests the necessity of considering the presence of third phases such as vacancy, etc.

3.2 Residual Stress Measurement of Machined Plane

Measurements were made on the #200 heavy ground surface in three directions, the grinding positive direction ($+\psi$), grinding minus direction ($-\psi$), and grinding perpendicular direction. Measurements on other ground surfaces were made in two directions, the grinding positive direction ($+\psi$), and grinding perpendicular direction. Measurements were made in the longitudinal direction for lapped surfaces only. A waviness was observed on the zirconia phase (133) plane of #200 heavy ground and light ground materials in the 2θ-$\sin^2\psi$ diagram.

Then, a linear approximation by the least squares method was conducted on a 2θ-$\sin^2\psi$ diagram of various diffraction planes on various specimens. The straight line slope in all cases was greater in the grinding perpendicular direction than the grinding direction in the ground plane. Moreover, the so-called split phenomenon in which the slope of the 2θ-$\sin^2\psi$ diagram differed by the $+\psi$ and $-\psi$ directions was seen in the zirconia phase (133) plane of #200 heavy and light ground materials. Moreover, the split phenomenon was also observed in the simple substance zirconia.[3] On the other hand, the ψ split phenomenon was not recognized in the 2θ-$\sin^2\psi$ diagram of the alumina phase (146) plane.

A residual stress measurement was conducted on three specimens by using the X-ray stress constant K of Table 3 and taking into consideration the variation among specimens under respective processing conditions. Since it was simple, a linear approximation was also conducted when there was a waviness in the 2θ-$\sin^2\psi$ diagram as mentioned above. The results of residual stress measurement of the alumina (146) plane was shown in Table 6 and that

of the zirconia (133) plane are shown in Table 7. The 68.3 percent confidence limits of various measured values have been shown in the tables at the same time. Moreover, the mean value of the three measured values and the 68.3 percent confidence limits have been shown. Figure 8 shows the 2θ-$\sin^2\psi$ diagram of the zirconia (133) plane for the #200 heavy-ground material in which the ψ split has appeared and Figure 9 shows the 2θ-$\sin^2\psi$ diagram of the alumina (146) plane in which the ψ split was not recognized. The residual stress difference by the surfaced processing condition difference is almost the same for the #200 heavy- and light-ground materials and it becomes smaller in the order of the #600 precise ground material and lapped surface material. It is known from the results mentioned above that the residual stress size is not dependent on cutting depth but is dependent on the particle size of the abrasive grain. The fact that all values of various ground surfaces are smaller for the (146) plane with a deep penetration depth than the (133) and (1.0.10) planes shows that the large residual stress of the surface is attenuated toward the interior. The phase stress can be studied by comparing the residual stress of the Al_2O_3 (1.0.10) plane and ZrO_2 (133) plane.
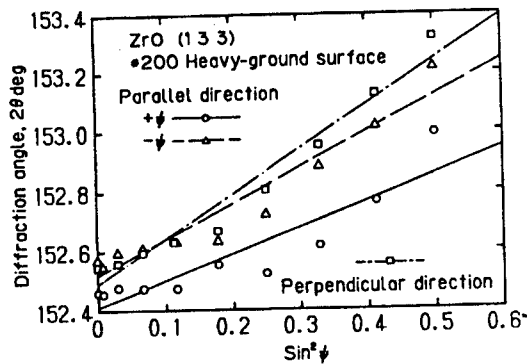
Figure 8. 2θ Versus $\sin^2\psi$ for ZrO_2 (1 3 3)
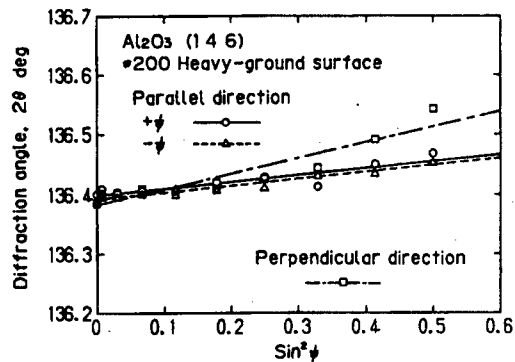
Figure 9. 2θ Versus $\sin^2\psi$ for Al_2O_3 (1 4 6)

Table 6. Residual Stresses on Ground Surfaces Measured for Al_2O_3 (1 4 6)

Specimen number	Surface condition	Residual stress for (1 4 6) plane (MPa)	
		Parallel direction	Perpendicular direction
10 13 14	Heavy-ground (#200)	-74±18 -95±20 -99±19	-233±15 -181±24 -225±15
mean		-89±10	-213±21
15 16 17	Light-ground (#200)	-110±17 -82±19 -104±24	-205±5 -228±17 -215±29
mean		-99±11	-216±9
7 8 9	Fine-ground (#600)	-30±25 -32±15 -51±41	-70±11 -72±39 -85±9
mean		-38±9	-76±6

Table 7. Residual Stresses on Ground and Lapped Surfaces Measured for
ZrO$_2$ (1 3 3)

Specimen number	Surface condition	Residual stress for (1 3 3) plane (MPa)	
		Parallel direction	Perpendicular direction
10	Heavy-ground (#200)	-356±61	-603±98
13		-184±37	-501±80
14		-297±41	-566±120
mean		-279±87	-556±52
15	Light-ground (#200)	-343±59	-691±154
16		-429±169	-561±118
17		-309±65	-714±154
mean		-360±62	-655±82
7	Fine-ground (#600)	-71±17	-176±48
8		-73±19	-163±51
9		-85±18	-164±46
mean		-77±8	-168±7
1	Lapped	-12±14	-----
2		-4±26	-----
4		-18±15	-----
mean		-11±7	-----

4. Conclusion

Measurement for the X-ray elastic and stress constants was conducted first
for measuring the X-ray residual stress of zirconia-alumina composite
ceramics. The CuKα radiation was used as the characteristic X-ray for
measuring the alumina phase (146) plane, CaKα radiation was used as the
characteristic X-ray for measuring the alumina (1.0.10) plane, and the
lapped material was used for measuring the zirconia (133) plane. A
theoretical computation was then conducted by the Kroener model. Moreover,
the residual stress of heavy-ground material, light-ground material,
precise-ground material, and lapped material was measured by using the
X-ray diffraction method. The results available were as follows:

(1) X-ray stress measurement is also possible in composite ceramics and the
X-ray elastic and stress constants of various diffraction angles were
determined. The measuring error was small and the accuracy was high for all
planes. The obtained X-ray elastic constants of composite ceramics became
the intermediate value of elastic constants of the simple substance alumina
and zirconia for both the alumina and zirconia phases but the Poisson's
ratio difference between the two phases inversely became slightly wider than
in the case of a simple substance.

(2) The X-ray elastic constants of the (146) and (1.0.10) planes obtained
by experiment were of smaller values than the X-ray elastic constants of
various diffraction planes obtainable by substituting the mechanical elastic
constants obtained by experiment in the Kroener model.

(3) All residual stress of the heavy-ground plane, light-ground plane,
precise-ground plane, and lapped surface measured by the X-ray diffraction
method are compressions and the compressive residual stress on the ground
surface is greater in the ground perpendicular direction than the ground
parallel direction. The residual stress size by the surface processed
condition difference was dependent on the particle is of the abrasive grain
and not dependent on the cutting depth size. The size of the compressive
residual stress was in the order of heavy-ground surface, light-ground
surface, precise-ground surface, and lapped surface.

(4) Just as in the case of simple substance zirconia, a ψ split phenomenon was observed on the zirconia phase (133) phase of the #200 heavy-ground material in the 2θ-$\sin^2\psi$ diagram.

In conclusion, we express our deep gratitude to the Nippon Tokushu Togyo Co., Ltd., that has offered us materials necessary for this experiment.

References

1.   Tanaka, Matsui, and Akiba, MATERIALS, Vol 35 No 394, 1987, p 749.

2.   Tanaka, Suzuki, and Kurimura, THE SOCIETY OF MATERIALS SCIENCE, JAPAN, Manuscripts of lecture theses for the 24th Symposium on X-Ray Material Strength, 1987, p 196.

3.   Tanaka, Kurimura, Akiba, Suzuki, and Nakagawa, Ibid., p 135.

4.   Kishimoto, Ueno, Kawamoto, and Kondo, MATERIALS, Vol 36 No 407, 1987, p 810.

5.   Ei, Fujiwara, and Fujimoto, Literature 2), 1987, p 219.

6.   Tanaka, Yamamoto, Kurimura, and Akiba, Literature 2), 1987, p 208.

7.   B.D. Cullity, Translated by Gentaro Matsumura, "New Edition X-Ray Diffraction Digest Theory," Agne, 1980.

X-Ray Elastic Constant of Silicon Carbide, X-Ray Measurement of Grinding Residual Stress

[Article by Keisuke Tanaka, Department of Engineering Science, Kyoto University, Kyoto; Yuji Yamamoto and Noriaki Mine, Graduate School, Kyoto University; Kyoto and Kenji Suzuki, Faculty of Education, Niigata University, Niigata; from the 25th Symposium on X-Ray Studies on Mechanical Behavior of Materials held 21-22 July 1988]

[Text]   The elastic constants of silicon carbide for X-ray stress measurement were determined for the diffraction planes (2.0.15), (213), and (203). The X-ray elastic constants of polycrystals of silicon carbide were theoretically determined on the basis of Voight, Reuss, and Kroener models and were compared with the experimental results. The residual stress of silicon carbide were measured on the ground and lapped surfaces.

1. Introduction

It is considered that the residual stress in ceramics exerts a great effect on brittle fracture and the X-ray stress measurement method has been used as the nondestructive measuring method of this residual stress.[1]

The atmospheric sintered silicon carbide had been taken up in this research and the X-ray elastic and stress constants were experimentally determined in the first place. The CuKα, FeKα, and CrKα radiations were used for the characteristic X-rays. Then, an X-ray residual stress measurement was conducted on a silicon carbide surface that was ground by the #200 diamond grindstone and on a silicon carbide surface provided with lapping.

Moreover, the theoretical computation results by the Voight,[2] Reuss,[3] and Kroener[4] models and experimental results in X-ray elastic constants were compared.

2. Experiment Method

2.1 Material and Specimen

The material used is a silicon carbide, it is an atmospheric sintered product that has been sintered for 1 to 2 hours at the temperature of 2,000°C in N_2 gas of 1 atmospheric pressure after forming the silicon carbide powder at the pressure of 1,500 kgf/cm² (147 MPa) in ordinary temperature and it has the density of 3.11 g/cm². The specimen is a square bar of 55.0 mm length having a rectangular section of 9.7 mm width and 3.5 mm height.

Strain gauges were attached to the specimen and mechanical elastic constants were obtained by the applied stress-strain straight line under the four-point bending test. The mechanical Young's modulus was 414 GPa and the Poisson's ratio was 0.146. The mean center line roughness of the specimen surface was Ra = 0.074 μm on the lapped surface, it was Ra = 0.30 μm in the grinding direction of the ground surface and Ra = 0.55 μm in the grinding perpendicular direction of the ground surface.

2.2 Determination of X-Ray Observation Conditions for Stress Measurement and Diffraction Angle

A parallel beam slit for stress measurement was equipped on a diffractometer (Shimadzu XD-3A) and used for the measurement of the X-ray diffraction profile. The X-ray observation conditions for stress measurement are arranged and shown in Table 1.

Table 1. X-Ray Conditions for Stress Measurement

Method		Parallel beam method		
Characteristic X-ray		CuKα	FeKα	CrKα
Diffraction plane		(2.0.15)	(2 1 3)	(2 0 3)
Diffraction angle	(deg)	146.50	156.08	125.16
Filter		Ni	Mn	V
Tube voltage	(kV)	40	40	40
Tube current	(mA)	40	30	40
Divergent angle	(deg)	0.64	0.64	0.64
Irradiated area (mm² rectangle)		4 x 8	4 x 8	4 x 8
Scanning speed	(deg/min)	1	1	1
Preset time	(sec)	2	1	2

The crystal structure of the used silicon carbide was a hexagonal of α-SiC, mainly constituted of 6H, and slightly mixed with 15R in the polymorphism. The lattice constant of this material was determined by the diffraction angles of the (2.0.15) and (129) planes of CuKα radiation by using the step scan method on the material annealed for 2 hours at the temperature of 1,200°C after lapping. The lattice constant was a = 3.083 and c = 15.119 Å. Determination of the diffraction angle for X-ray stress

61

measurement was based on the midpoint of the width at 80 percent height of the profile in the (2.0.15) plane by CuKα radiation, at 75 percent height of the profile in the (213) plane by FeKα radiation, and at 50 percent height of the profile in the (203) plane by CrKα radiation. Ten points notched at 5° intervals between 0° to 45° was adopted for the X-ray incident angle ψ_0 and the 2θ-$\sin^2\psi$ diagram was drawn.

The X-ray penetration depth for various diffraction planes is shown in Figure 1. The greater the X-ray incident angle ψ_0, the shallower the penetration depth and the deepest penetration is CrKα radiation followed by FeKα radiation and CuKα radiation.
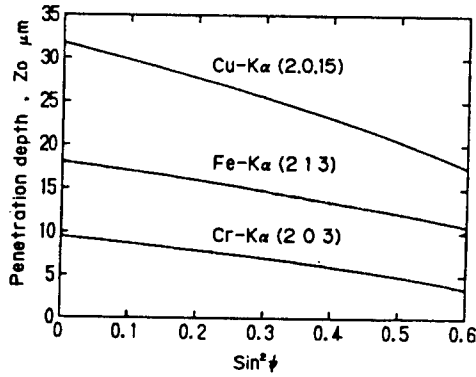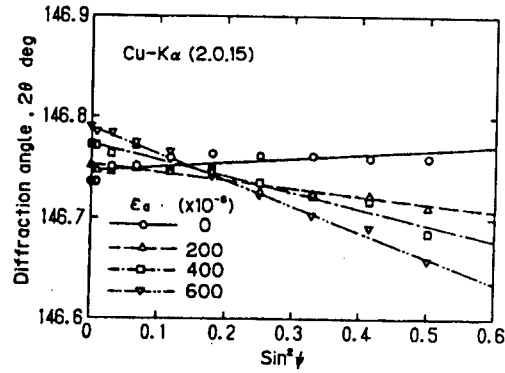
Figure 1. X-ray Penetration Depth   Figure 2. 2θ Versus $\sin^2\psi$

2.3 Measurement Method of X-Ray Elastic Constants

The four-point bending device was used in the measurement of X-ray stress constants. Strain gauges were attached to the specimen in this research, the 2θ-$\sin^2\psi$ diagram was obtained for various set strains and the constants were determined by this diagram. Now, there are the following relations between the stress in the material and slope M of the 2θ-$\sin^2\psi$ diagram[5] as shown in the following formulas (1) and (2)

$$\sigma_x = K \cdot M \tag{1}$$

Here, K is called the X-ray stress constant and is a negative number.

$$K = 1/(\partial M/\partial \sigma_x) = -[E/2(1 + \nu)] \cdot \cot\theta_0 \tag{2}$$

In other words, the stress constants can be determined by the linear relation slope M-σ_x when M is obtained for various stresses σ_x. The X-ray compliance $s_2 = 2(1 + \nu)/E$ is obtainable from the following formula.

$$s_2 = 2(1 + \nu)/E = -\cot\theta_0/K = -\cot\theta_0 \partial M/\partial \sigma_x \tag{3}$$

On the other hand, $-s_1 = \nu/E$ is determined as follows by the rate of change of intersecting point 2θ $\psi = 0$ with the y-axis against σ_x in the 2θ-$\sin^2\psi$ diagram.

$$-s_1 = \nu/E = [\cot\theta_0/2] \, \partial(2\theta_{-0})/\partial\sigma_x \tag{4}$$

The change of the applied stress in the above formula is equal to the product of the applied stress change and mechanical elastic constant.

2.4 Measurement of Residual Stress

The residual stress of the ground and lapped surfaces was measured. Measurements were made in two directions on the ground surface, the ground direction and the direction perpendicular to the ground direction. The residual stress σ was obtained from slope M of the 2θ-$\sin^2\psi$ diagram by using the actually measured X-ray stress constant K.

3. Experiment Results and Discussion

3.1 X-Ray Elastic Constants

The lapped material was used for the measurement of X-ray elastic constants. The applied strain ε_a was measured repeatedly for five times at ε_a = 0, 600 x 10^{-6} and three times at ε_a = 200, 400 x 10^{-6} and the mean measured value at each ε_a was made the diffraction angle at the ψ_0 of the applied stress. Figure 2 shows the 2θ-$\sin^2\psi$ diagram for each ε_a on the (2.0.15) plane. Although a dispersion is seen in the experimental points, an almost linear approximation is also possible for all cases and the regression straight line by the least squares method has been shown in the diagram. The linear slope M reduces with the increase of ε_a. The relation between M and ε_a is shown in Figure 3. Moreover, the relation between applied strain ε_a and intercept 2θ ψ = 0 of y-axis and the regression straight line is shown in Figure 4. Linear approximation is possible in both diagrams and the regression straight line by the least squares method has been shown in the diagrams. Moreover, the longitudinal bar in the diagrams shows the 68.3 percent confidence limits for slope M and 2θ ψ = 0 by the least squares method approximation on ε_a in each 2θ-$\sin^2\psi$ diagram.
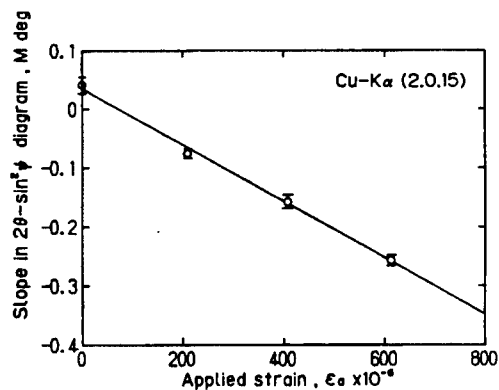
Figure 3. M Versus Applied Strain   Figure 4. Intercept Versus Applied Strain
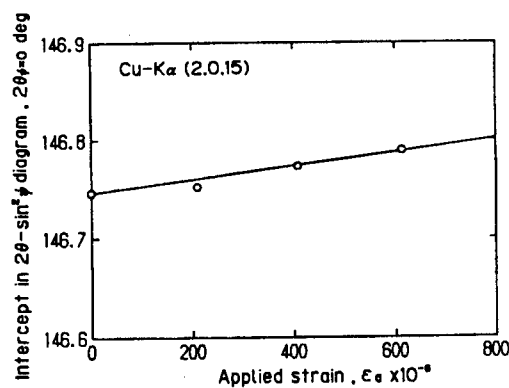
The X-ray stress constant K obtained from the M-ε_a relation slope by using formula (2), (1 + ν)/E obtainable from formula (3) by using the theoretical diffraction angle θ_0, ν/E obtainable from the rate of change for

σ_x of 2θ $\psi = 0$ by using formula (4) and the 68.3 percent confidence limits of $(1 + \nu)/E$ and ν/E are arranged and shown in Table 2. Moreover, results on computing E and ν from these are also shown in Table 2. Various values differ according to the diffraction plane and the so-called diffraction plane dependency was shown. This is because it has become the average of specific crystals for satisfying the diffraction conditions and differs with the values of mechanical elastic constant 414 GPa and Poisson's ratio 0.146.

Table 2. X-Ray Elastic Constant and X-Ray Stress Constant

Diffraction plane	X-ray compliance		X-ray elastic constant			Stress constant
	$(1+\nu)/E$	ν/E	$E/(1+\nu)$	E	ν	K
	$(10^{-3}/GPa)$	$(10^{-4}/GPa)$	(GPa)	(GPa)		(MPa/deg)
(2.0.15)	3.04 ± 0.16	4.65 ± 0.91	329	388	0.18	-864
(2 1 3)	2.58 ± 0.34	4.69 ± 0.77	388	474	0.22	-717
(2 0 3)	2.73 ± 0.97	1.58 ± 3.11	367	389	0.06	-1660

3.2 Residual Stress Measurement of Ground and Lapped Surfaces

The 2θ versus $\sin^2\psi$ diagram of the lapped surface, parallel direction to the ground direction and perpendicular direction to the ground direction of the (2.0.15) plane are shown in Figure 5. A large nonlinearity is not observed on all surfaces in the diagram. A linear approximation by the least squares method has been shown in the diagram. The linear slope has become greater in the order of the lapped surface, ground parallel direction, and ground perpendicular direction for all surfaces and all show a compressive residual stress of a straight line with the right side raised.
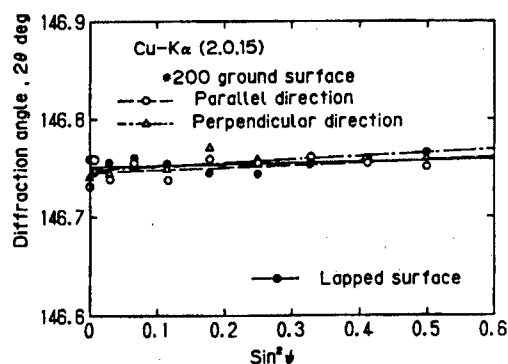
Figure 5. 2θ Versus $\sin^2\psi$

The three types of residual stresses mentioned above were measured by X-ray diffraction by using three specimens. The measured values and standard deviations of the three specimens are shown in Table 3.

Although there is a dispersion in the measured values of each specimen, it was known from the table that the compressive residual stress was reduced in the order of the (203), (213), and (2.0.15) planes. This as shown in Table 3 demonstrates that compressive residual stress on a large surface is

reduced upon entering the interior as the penetration depth to various diffraction planes differs and it deeply penetrates in the order of the (203), (213), and (2.0.15) planes. Moreover, it is shown that the ground surface has a greater compressive strain than the lapped surface and that there is a directional property of residual stress causing a greater compressive residual stress in the ground perpendicular direction than the ground parallel direction. This tendency is also recognized in silicon nitride,[6] zirconia,[7] and zirconia-alumina composite ceramics.[8]

Table 3. Residual Stress on Ground and Lapped Surface

Specimen number	Surface condition	Residual stress (MPa)					
		(2.0.15) plane		(2 1 3) plane		(2 0 3) plane	
		Parallel direction	Perpendicular direction	Paralell direction	Perpendicular direction	Parallel direction	Perpendicular direction
2	Lapped	- 4 ± 20	-----	-30 ± 12	-----	58 ± 28	-----
3		-11 ± 15	-----	-26 ± 15	-----	72 ± 25	-----
5		-10 ± 13	-----	-26 ± 10	-----	- 3 ± 52	-----
Mean	Lapped	- 8 ± 3	-----	-27 ± 2	-----	42 ± 30	-----
7	Ground #200	-37 ± 26	-44 ± 11	-34 ± 13	-45 ± 17	-69 ± 38	-118 ± 31
8		-23 ± 17	-29 ± 12	- 2 ± 13	-42 ± 14	-10 ± 19	-102 ± 25
10		-33 ± 21	-36 ± 9	-11 ± 5	-48 ± 16	-65 ± 42	-146 ± 30
Mean	Ground #200	-31 ± 6	-36 ± 6	-16 ± 13	-45 ± 2	-48 ± 25	-122 ± 17

4. Studies on X-Ray Elastic Constants

4.1 Theoretical Computation of X-Ray Elastic Constants by Reuss and Voight Models

There are the strain-fixed Voight model[2] and stress-fixed Reuss model[3] as the classical models on polycrystalline substance elastic deformation. X-ray elastic constants by the Voight model are equal to mechanical values but X-ray elastic constants by the Reuss model differ according to diffraction planes and they differ from mechanical values. The mechanical and X-ray elastic constants of silicon carbide with a hexagonal structure obtained by the Voight model are given under the following formulas by using the single-crystal stiffness c_{ii}.[9]

$$(1 + \nu)E = 15/(7c_{11}+2c_{33}-5c_{12}-4c_{13}+12c_{44}) \tag{5}$$

$$-\nu/E = 3(4c_{44}-c_{11}-c_{33}-5c_{12}-8c_{13})$$
$$/(2c_{11}+c_{33}+2c_{12}+4c_{13})$$
$$/(7c_{11}+2c_{33}-5c_{12}-4c_{13}+12c_{44}) \tag{6}$$

Whereas, the mechanical elastic constants by the Reuss model are given by the following formulas.

$$(1 + \nu)/E = (2s_{11}-s_{12}-s_{13})/2$$
$$-(5s_{11}-s_{12}-5s_{13}+s_{33}-3s_{44})/6$$
$$+3(s_{11}-2s_{13}+s_{33}-s_{44})/10 \tag{7}$$

$$-\nu/E=(s_{12}+s_{13})/2$$
$$+(s_{11}-s_{12}-s_{13}+s_{33}-s_{44})/6$$
$$-(s_{11}-2s_{13}+s_{33}-s_{44})/10 \tag{8}$$

Here, s_{ii} is the elastic compliance. Moreover, the X-ray elastic constants by the Reuss model are given by the following formulas.

$$(1 + \nu)/E=(2s_{11}-s_{12}-s_{13})/2$$
$$-(5s_{11}-s_{12}-5s_{13}+s_{33}-3s_{44})w^2/2$$
$$+3(s_{11}-2s_{13}+s_{33}-s_{44})w^4/2 \tag{9}$$
$$-\nu/E=(s_{12}+s_{13})/2$$
$$+(s_{11}-s_{12}-s_{13}+s_{33}-s_{44})w^2/2$$
$$-(s_{11}-2s_{13}+s_{33}-s_{44})w^4/2 \tag{10}$$

Here, w is one of the direction cosines (u,v,w) of plane normal and the relationship with the diffraction plane indexes (h,k,l) is given under the following formula by using the lattice constant ratio λ = c/a.

$$w=3^{\frac{1}{2}}\cdot 1/[4\lambda^2(h^2+hk+k^2)+3l^2]^{\frac{1}{2}} \tag{11}$$

4.2 Theoretical Computation of X-Ray Elastic Constants by Kroener Model

The X-ray elastic constants by the Kroener model are available by the following simultaneous equations on x and shear modulus μ.[10]

$$[\{12(6d-b)+10a\}\mu-3c]x^2$$
$$+\{-8(6d-b)\mu^2+(7c-72e)\mu-(3dc+4ea)\}x$$
$$-48e^2+(2dc-4ea)\mu-5ec=0 \tag{12}$$
$$4(18\mu+a)x^2+\{-48\mu^2-6(a-2b)\mu+2c\}x$$
$$-8b\mu^2-3\mu c=0 \tag{13}$$

Here, x is expressed as follows by the modulus of elasticity of volume K and shear modulus μ.

$$x = \mu(9K+8\mu)/6(K+2\mu) \tag{14}$$

a, b, c, d, and e are given under the following formulas by using stiffness.

$$a=2(c_{11}+c_{12}=2c_{13})+c_{33} \tag{15}$$
$$b=c_{11}+c_{12}+2c_{33}-c_{13} \tag{16}$$
$$c=2(c_{11}+c_{12}+c_{13})(c_{33}-c_{13})$$
$$+(c_{33}+2c_{13})(c_{11}+c_{12}-2c_{13}) \tag{17}$$
$$d=c_{44}+(c_{11}-c_{12})/2 \tag{18}$$
$$e=c_{44}(c_{11}-c_{12})/2 \tag{19}$$

Moreover, the X-ray elastic constants by the Kroener model are available in the following manner. Now, when directing attention to a single crystal in a polycrystalline substance, the relationship between strain ε_{ii} and applied stress σ_{kl}^A in the crystal becomes as follows:

$$\varepsilon_{ii}=s_{iikl}\sigma_{kl}^A \tag{20}$$

66

Here, s_{iikl} is the elastic compliance of a single crystal. On the other hand, it becomes as follows in the Kroener model due to the constraint mutually among the crystals.

$$\varepsilon_{ii}=(S_{iikl}+t_{iikl})\sigma_{kl}{}^{A} \tag{21}$$

Here, s_{iikl} is the compliance as a polycrystal, t_{iikl} is the addition item caused by constraint and this value is determined by the single-crystal compliance and mechanical elastic constant as a polycrystal based on the Eshelby theory.[11] The X-ray elastic constants are given under the following formulas by using these matrix displays s_{ii} and t_{ii}.[12]

$$(1+\nu)/E = S_{11}-S_{12}+(2t_{11}-t_{12}-t_{13})/2$$
$$-(5t_{11}-t_{12}-4t_{13}-t_{31}+t_{33}-3t_{44})w^2/2$$
$$+3(t_{11}-t_{13}-t_{31}+t_{33}-t_{44})w^4/2 \tag{22}$$

$$-\nu/E = S_{12}+(t_{12}+t_{13})/2$$
$$+(t_{11}-t_{12}-2t_{13}+t_{31}+t_{33}-t_{44})w^2/2$$
$$-(t_{12}-t_{31}-t_{13}+t_{33}-t_{44})w^4/2 \tag{23}$$

Here, the polycrystal elastic constants have the following relationship with K and μ.

$$S_{11}=(3K+\mu)9K\mu \tag{24}$$
$$S_{12}=(3K-2\mu)/18K\mu \tag{25}$$

The elastic compliance and stiffness of the single crystal silicon carbide are shown in Table 4. Moreover, both $(1 + \nu)/E$ and ν/E of formula (7) become the function of $w^2=\cos^2\varphi$ when the angle formed by c-axis and plane normal of diffraction planes (h,k,l) is made the φ angle. The elastic constants obtained by using the values of Table 4 for diffraction planes of (2.0.15), (213), and (203) which have been actually measured in the preceding chapter are shown in Table 5. By adopting the polar coordinate display in which the axis of ordinates is of c-axis (z-axis) direction, the angle φ is taken in the clockwise direction and $E/(1 + \nu)$ is made the radius vector length, Figure 6 shows the X-ray elastic constants of the Reuss model by a solid line, the mechanical elastic constants by a two-dot chain line, the mechanical elastic constants of the Voight model by a broken line, the X-ray elastic constants of the Kroener model by a single-dot chain line, the mechanical elastic constants by a dotted line, and the experimental values by a black circle. The X-ray $E/(1 + \nu)$ by the Reuss model becomes smaller in the order of the (213), (203), and (2.0.15) planes and the $E/(1 + \nu)$ of (213) and (203) planes are greater than the mechanical values. The computation results by the Kroener model also showed the same tendency as this and an intermediate value between the Reuss and Voight models was computed.

Table 4. Elastic Compliance and Stiffness

Stiffness (10^2 GPa)	c_{11}	c_{12}	c_{13}	c_{33}	c_{44}
	5.00	0.92	0	5.64	1.68

Compliance ($1/10^2$ GPa)	s_{11}	s_{12}	s_{13}	s_{33}	s_{44}
	0.2070	-0.0381	0	0.1773	0.5952
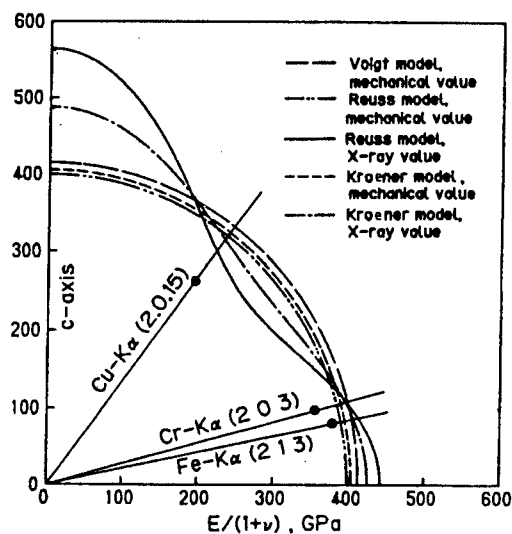
Figure 6. Elastic Constant $E/(1 + \nu)$ for SiC

Table 5. Elastic Constants Calculated on the Basis of Voight, Reuss, and Kroener Models

Elastic constants	Voigt model	Reuss model				Kroener model			
		Mechanical Value	X-ray value			Mechanical Value	X-ray value		
			(2.0.15)	(2 1 3)	(2 0 3)		(2.0.15)	(2 1 3)	(2 0 3)
Young's modulus E (GPa)	457	444	422	468	459	450	439	461	456
Poisson's ratio ν	0.108	0.119	0.132	0.104	0.111	0.114	0.120	0.108	0.111
$E/(1+\nu)$ (GPa)	412	397	373	424	413	404	392	416	411

4.3 Comparison of Experimental Results and Theoretical Computations

First of all, the mechanical elastic constant elastic constant and Poisson's ratio by the Voight, Reuss, and Kroener models showed that E was larger and ν was of a smaller value than those mechanically measured by the four-point bending method. Besides the fact that SiC is a polymorphism and those of 15R and other structures are contained in this specimen mainly consisting of 6H structure, it is considered that the effect of vacancy presence is great. On the other hand, when comparing the experiment and theory especially on $E/(1 + \nu)$ in the X-ray elastic constants, it has become

68

smaller in the order of (213), (203), and (2.0.15) planes in experiment and this coincides with the theoretical estimate. Moreover, the absolute value is slightly smaller just as in the case of mechanical elastic constants.

The ratio of X-ray elastic constants to mechanical values on various diffraction planes was shown at the same time in the theoretical and experimental values of Table 6 and just as in Figure 6, this ratio was shown as the radius vector length by the polar coordinate display in Figure 7.

Table 6. Ratio of X-Ray Elastic Constant to Mechanical Value

Diffraction plane	Experimental data	Reuss model	Kroener model
(2.0.15)	0.91	0.94	0.97
(2 1 3)	1.07	1.07	1.03
(2 0 3)	1.02	1.04	1.02
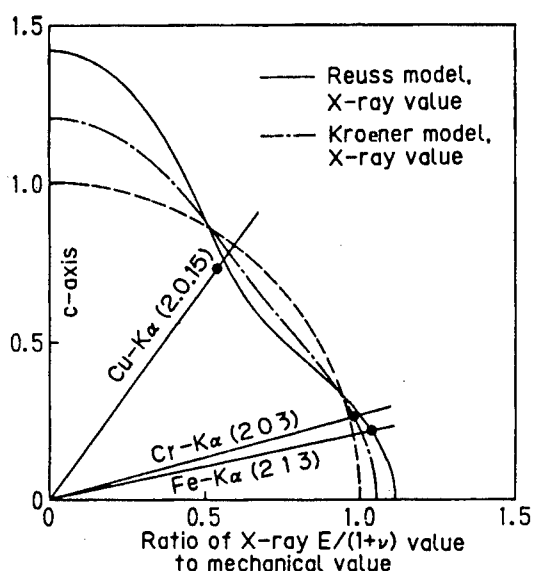
Figure 7. Ratio of X-Ray Elastic Constant to Mechanical Value

Normalization of the Reuss model was made with the mechanical elastic constants obtained by the Reuss model normalization of the Kroener model was made by the theoretically obtained mechanical plastic constants. The theoretical value ratio and experimental value ratio show practically identical values on all diffraction planes. The diffraction plane dependency of the X-ray elastic constants can be estimated by the Reuss or Kroener theory from this fact when the mechanical elastic constants of the material are known.

69

5. Conclusion

The following conclusion has been obtained in this research.

(1)   Measurement of X-ray residual stresses was possible by using the (2.0.15) plane for CuKα radiation, the (213) plane for FeKα radiation, and (203) plane for CrKα radiation, and these X-ray stress and elastic constants were determined. The measurement accuracy of the CrKα radiation (203) plane was slightly inferior.

(2) The X-ray and mechanical elastic constants were theoretically computed by the Reuss, Voight, and Kroener models. The X-ray elastic constant $E(1 + \nu)$ by the Reuss and Kroener models differed according to diffraction planes, it became smaller in the order of the (213), (203), and (2.0.15) planes and experimental results coincided with this tendency.

(3) Residual stresses of the ground and lapped surfaces measured by the X-ray diffraction method were all compressive residual stresses with the exception of the lapped surface of the (203) plane and the shallower the penetration depth of various diffraction planes, a greater compressive residual stress was measured. It can be presumed from this fact that the surface compressive residual strain reduces as it goes into the interior. Moreover, it is known that the compressive residual stress reduces in the order of ground perpendicular direction surface, ground parallel direction surface, and lapped surface. It was known that there was a directional property of the residual stress on the ground surface.

References

1.   Keisuke Tanaka, RESEARCH ON MACHINES, Vol 40 No 2, 1988, p 265.

2.   W. Voight, "Lehrbuch der Kristalphysik," Teubner, Berlin, 1928, p 962.

3.   A. Reuss, Z. ANG. MATH. MECH., Vol 9, 1929, p 49.

4.   E. Kroener, Z. PHYS., Vol 151, 1958, p 504.

5.   "X-Ray Stress Measurement Method," edited by THE SOCIETY OF MATERIALS SCIENCE, JAPAN, 1981, p 54, Yokendo.

6.   Keisuke Tanaka, Takayuki Kurimura, Eiji Matsui, and Yoshiaki Akiba, MATERIALS, Vol 36, 1987, p 817.

7.   Keisuke Tanaka, Takayuki Kurimura, Yoshiaki Akiba, Kenji Suzuki, and Heizaburo Nakagawa, Scheduled for publication in MACHINE LOGIC.

8.   Keisuke Tanaka, Yuji Yamamoto, Noriaki Mine, Takayuki Kurimura, Kenji Suzuki, and Heizaburo Nakagawa, Manuscripts of theses for the 25th Symposium on X-Ray Material Strength, 1988.

9. Keisuke Tanaka, Eiji Matsui, Takayuki Kurimura, and Yoshiyuki Akiba, MATERIALS, No 36, 1987, p 792.

10. G. Kneer, PHYS. STAT. SOL., Vol 3, 1963, p K331.

11. Toshio Mura and Tsutomu Mori, MICROMECHANICS, Baifukan, 1975, p 23.

12. P.D. Evenschor and V. Hank, Z. METALLKDE, Vol 63, p 798.

X-Ray Study on Surface Residual Stress Distributions at Near Interface of Ceramics-to-Metal Joint

[Article by Shunichiro Tanaka, New Material Engineering Laboratory, Toshiba Corp., and Katsuhiko Oguiso, Research and Development Department, Rigaku Corp.; from the 25th Symposium on X-Ray Studies on Mechanical Behavior of Materials held 21-22 July 1988]

[Text] The distribution of residual stresses in the surface near the joining boundary between β-Si_3N_4 and carbon steel was measured by the X-ray diffraction method. The X-ray system employed is a completely computer-controlled system equipped with a position-sensitive proportional counter and a collimator that allows irradiation to a very small limited area. The measurement results were compared with those by the finite element method.

1. Introduction

Development of new materials in recent years have been remarkable, however, there were many cases where the issue of how the arrangement of these new materials should be designed with conventional materials became an important problem when it came to putting these new materials to practical use. It is also the same when joining ceramics and metals and it is said that the concentration of stress and residual stress caused by the thermal expansion and elastic constant difference exerts a great effect on joining strength. The interface neighborhood is especially the singular point and although the residual stress distribution analysis is conducted by the finite element method, demand on actual measurement has become strong. There is the indentation fracture method[2] for simple measurement but the local residual stress release by cracks is also considerable and it is hard to say that it is a perfect method. By the way, the aggregate of fine crystal grains like ceramics is an ideal objective for the X-ray stress measurement method from the point of isotropy. Nevertheless, it is rather normal for conventional X-ray stress measuring devices to use a broad-focus X-ray tube so that the irradiation area can be expanded and a continuous debye ring is available also from a crystal grain of about several tens of microns. Therefore, it is necessary to stop down the incident beam in the stress measurement of a minute section of 2~3 mm and the actual state is that the shortage of incident X-ray strength is caused. Therefore, we stopped down the

fine-focus X-ray tube with a high focal brightness by using a collimater of $\phi 0.3$, irradiated near the joining interface and have already conducted stress measurement by using the position-sensitive proportional counter (PSPC).[3] Since we have studied the relationship between stress distribution and irradiation area and on the joining structure and residual stress distribution, we will report here on these.

2. Specimen

The joining structure and dimensions of specimens submitted for measurement are shown in Figure 1. All joinings are vacuum brazing by the active metal method. A is the specimen that has directly joined the β-silicon nitride (hereinafter called Si_3N_4) and carbon steel S45C, B is the specimen that has inserted a copper plate of 0.2 mm thickness for the purpose of thermal stress relaxation, and C is the specimen that has inserted S45C of 3 mm thickness between the two Si_3N_4 and conducted sandwiching both surfaces by copper plates of 0.2 mm thickness. The measured surface is in the plane ground condition that had been processed on simple substance parts before joining. The brazing flow to the interface neighborhood was within 0.1 mm and the boundary line could be clearly identified.
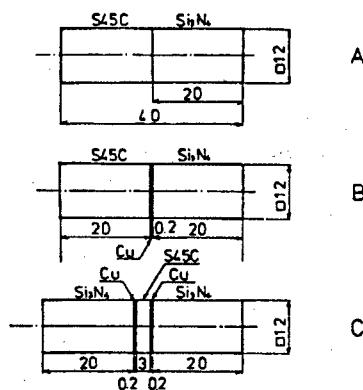
Figure 1. Structure of Si_3N_4/S45C Joined Specimen

3. Outline of X-Ray Stress Analyzer

The characteristics of the PSPC in comparison to the counterscanning method are found in the point that it is not affected by the output fluctuation of the X-ray source in addition to it being a linear detector. It may be said that it is optimum for this measurement which conducts measurement of microscopic parts necessitating the stop down of the incident beam. However, it does not mean that the beam can be stopped down infinitely and it will become spontaneously restricted by the X-ray tube brightness as well as the crystal properties and crystal grading of measured objectives. The panoramic photo of the PSPC system microscopic parts X-ray stress analyzer made by the Rigaku Corp. and used in this measurement has been shown in Figure 2 [not reproduced]. The orientation of measuring places was conducted by a microscope with the magnification of 40X and focal depth of 50 μ. Measurement was conducted by the five incident angle $\sin^2\psi$ side inclination method, the sample holder X and Y stages were

73

computer-controlled and stress distribution measurement as programmed was possible. Various conditions of X-ray stress measurement are shown in Table 1. Moreover, the X-ray elastic constant values measured by Ei, et al.,[4] were used in the stress constant computation.

Table 1. Conditions of X-Ray Stress Measurement

Lattice plane	β-Si_3N_4(212), 2θ = 131.5
X-ray tube	$CrK\alpha$ 30 KV, 45 mA
Collimator	ϕ0.1, 0.3, 0.5, 1.2
Detector	100 mm PSPC
Tilt angle	Side inclination method
	ψ = 0.15, 25, 30, 40°
Stress constant	K = 90.08

4. Studies of X-Ray Irradiated Area

It is assumed that the surface residual stress in the neighborhood of the joining interface has made a sudden change in the microscopic area. Some studies were made on this as there was a fear that the shape of the stress distribution curve became smooth by the X-ray irradiated area in such a case.

Figure 3 shows the relationship between the divergent optical system and irradiated area of this X-ray stress analyzer by the condition of the side inclination method. The collimater diameter was made the pinhole diameter ϕd value, the divergence angle ω was determined by the scatter pinhole and collimator length L_1 and the design values are shown in Table 2. The irradiated area ϕA expands as the incident angle ψ becomes inclined. Formula (1) shows the relationship of irradiated area ϕA and incident angle ψ and computation results have been added in Table 2. However, since the actual irradiated area shows the ellipse with the major axis in the measured stress direction and the minor axis in the right angle direction is fixed, the major axis has been shown as the diameter for convenience' sake.

Figure 4 shows the measurement results of residual stress distribution in the longitudinal direction on the center line of sample A by using the ϕ0.3~1 collimator. The axis of abscissa shows the distance from the joining interface on the center line of the Si_3N_4 surface and the axis of ordinates shows the residual stress. Circles on the center line show the X-ray irradiated area at ψ = 40° for all collimators. Moreover, the sample width value of the same size as the axis of abscissa has been shown for the axis of ordinates for reference. Although it will be the same as Figure 4 for Figures 5 to 7, the width size indication has been omitted. The irradiated area has not overlapped even when there are neighboring measuring points as in the case of ϕ0.3 and ϕ0.5 but approximately one-half of the irradiated area has overlapped in both adjoining measuring points in the case of ϕ0.1. Although it cannot be necessarily said that the result in the case of ϕ0.3 is an accurate distribution, it has become slightly lower when the irradiated area is expanded which probably is due to its becoming averaged by the neighboring stress values. Therefore, the collimator of ϕ0.3 was used after this for all measurements. Moreover, measurement of ϕ0.1 was

also tried but it has not been conducted this time because it required more than 3 hours for a single measurement in addition to strength being weak and measured values lacking reliability.
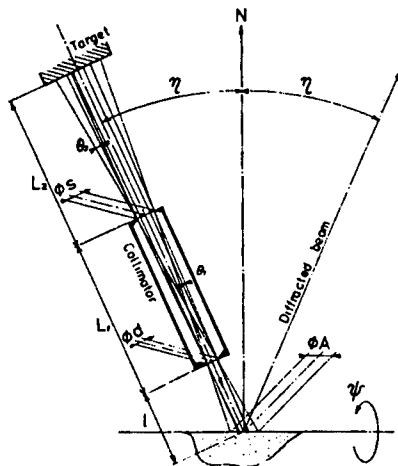
Figure 3. X-Ray Optical System and Irradiated Area A for Residual Stress Measurement by Collimated X-Ray
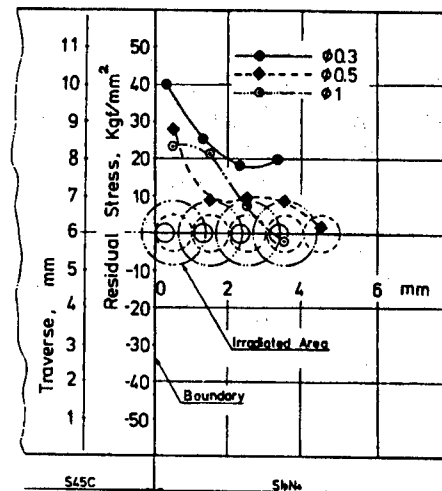
Figure 4. Residual Stress Distributions With Different Irradiated Area on the Same Specimen A

$$A = \left[d - 2t\tan\theta + t\sqrt{\left(\frac{1}{\cos\theta_1}\right)^2 + \left(\frac{1}{\cos\theta_2}\right)^2 - \frac{2\cos(\theta_1+\theta_2)}{\cos\theta_1\cos\theta_2}} \right] \frac{1}{\cos\psi} \qquad (1)$$

Formula (1)   Relationship of Irradiated Area ϕd Value and Incident Angle
Here, $\tan\theta_1 = (S-d)/2L_1$; $\tan\theta_2 = (S+d)/2L_1$

Table 2. Variation of X-Ray Irradiated Area ϕA With Collimated Diameter ϕD and Divergent Angle ω

ϕd	$\omega°$	ϕA (ψ=0)	ϕA (ψ=40)
0.1	0.13	0.15	0.38
0.3	0.40	0.41	0.53
0.5	0.68	0.67	0.88
1	1.32	1.36	1.77

5. Measurement Results

Measured parts are on a straight line distanced 0.3 mm and parallel to the joining interface and on a straight line of the sample, and both measured parts are on the Si_3N_4 side. Figures 5 to 7 show the measured results. All of the (a) diagrams show the residual stress distribution along the boundary line and all of the (b) diagrams show the residual stress distribution along the center line. Figure 5 shows the specimen that has directly joined Si_3N_4 with S45C without using a copper plate as the intermediate material. There is a tendency of tensile residual stress increase in the Z direction and a compressive residual stress increase in the t direction in proportion to
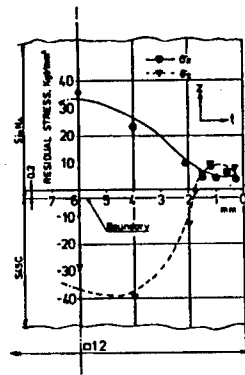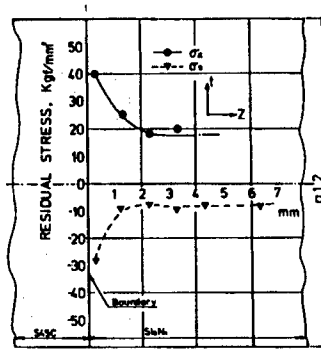
Figure 5. Specimen A
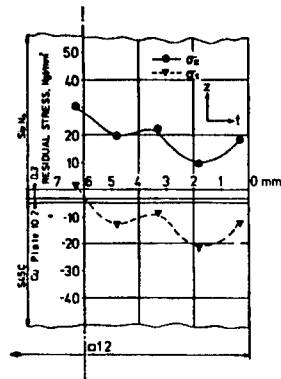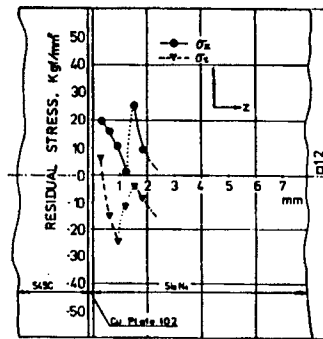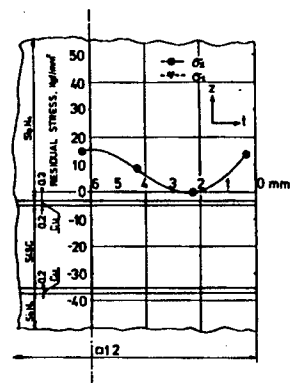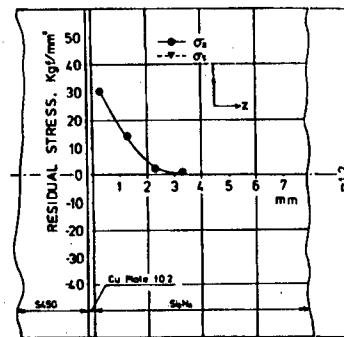
Figure 6. Specimen B

Figure 7. Specimen C

moving toward the center line along the interface, and the end parts are of a tensile residual stress of several kg/mm^2 for both directions. It asymptotically reduces for both directions in the center line upon becoming distanced from the interface and it almost reaches equilibrium at 2 mm. σ_z and σ_t are symmetrical for both diagrams (a) and (b). Figure 7 is the measured results of the σ_z direction only, however, it is considered almost the same as that in Figure 5 from the tendency aspect. However, the residual stress has become lower by 20~30 percent due to the effect of copper plate as a relaxation material of thermal stress. Figure 6 presents a mysterious distribution against these. Although almost the same pattern as Figures 5 to 7 are considerable on σ_z along the interface, the σ_t direction totally differs. Moreover, points of discontinuity exist in places distanced 1 mm from the boundary in observing the distribution on the center line of (b) diagram. The common point of diagrams (a) and (b) is that the σ_z and σ_t directions show a distribution resembling acting in concert. The reason for this is unknown now but it can also be considered as resulting from a complicated elastoplasticity constraint by the microscopic nonadhesion parts at the boundary. Such a thing is an unavoidable fact in brazing and it is considered necessary to increase the measuring examples under the same joining structure and conditions and to cope with the nonadhesion boundary observation by some sort of method. Moreover, the group headed by Kobayashi have conducted a thermal elastoplasticity analysis on the sample B shaped joining structure by using the finite element method[5] and it has been ascertained that the stress distribution in the interface neighborhood of Si_3N_4 almost coincided with diagram (b) of Figures 5 to 7.

6. Conclusion

The following conclusion was obtained as a result of conducting a surface residual stress measurement near the joining part of ceramics and metals by the X-ray diffraction method.

(1) It was known that the X-ray stress measurement of microscopic areas like the joining interface neighborhood was possible by stopping down the irradiated area by collimator of $\phi 0.3$.

(2) The surface residual stress along the joining interface shows a minimum single peak-shaped distribution at a place 1~2 mm from the edges and shows a maximum single peak-shaped distribution at the center.

(3) The surface residual stress on the center line of the joined body generates a large stress concentration toward the interface which results in an inverse direction symmetric distribution in the center line and perpendicular directions.

(4) The residual stress near the interface is reduced when a copper plate is placed between ceramics and metals.

(5) There are cases when it results in an amorphous stress distribution by the interface adhesion condition.

We have merely conducted the X-ray stress measurement only as mentioned above but we have scheduled to comply with analysis by FEM, adhesion interface observation, and bending tests in the future.

References

1. Tadatomo Suga, Manuscripts of lecture theses for the 24th Symposium on X-Ray Material Strength, THE SOCIETY OF MATERIALS SCIENCE, JAPAN, December 1987, p 51.

2. D.B. Marshall and B.R. Lawn, JOURNAL OF AMERICAN CERAMICS SOCIETY, Vol 60, 1977, p 86.

3. Shunichiro Tanaka and Katsuhiko Oguiso, Outline of Great Spring Meeting General Lectures, THE SOCIETY OF MATERIALS SCIENCE, JAPAN, March 1986, p 356.

4. Takao Ei, et al., Manuscripts of lecture theses for the 23d Symposium on X-Ray Material Strength, THE SOCIETY OF MATERIALS SCIENCE, JAPAN, July 1986, p 203.

5. Hideo Kobayashi, et al., private message.

Effect of Grinding Residual Stress on Bending Strength of Ceramics

[Article by Kenji Suzuki, Faculty of Education, Niigata University, Niigata; Keisuke Tanaka, Faculty of Engineering, Kyoto University, Kyoto; Yuji Yamamoto, Graduate School, Kyoto University, Kyoto; and Heizaburo Nakagawa, Japan Fine Ceramics Center, Nagoya; from the 25th Symposium on X-Ray Studies on Mechanical Behavior of Materials held 21-22 July 1988]

[Text] 1. Introduction

Ceramics have been used for structural members in recent years but there are still problems such as brittleness and strength evaluation remaining in ceramics. Engineering ceramics are generally subjected to some sort of mechanical processing, especially grinding after sintering, and are used as machine parts. Although grinding in this case is conducted while paying attention to roughness, etc., sufficient studies have not been made yet on residual stress. It has been reported that residual compressive stress is induced on the processed surface of ceramics by various grindings.[1-4] It can be fully considered that this residual stress exerts an effect on the strength of ground ceramics.

On the other hand, the X-ray stress measurement method of ceramics has been remarkably developed in the past several years.[5] Based on the results of these X-ray stress measurements, together with clarifying the generation of residual stress by grinding of ceramics and its distribution form in this research, studies were made on how the residual stress and damages formed on the occasion affected the strength of ceramics by conducting bending tests. Moreover, studies were also made on the strength evaluation model when a compressive residual stress existed.

2. Experiment Method

2.1 Specimens and Material

Two types of specimen materials, atmospheric sintered alumina and atmospheric sintered silicon nitride with a purity of 99 percent were used in this research. The mechanical properties of both materials are shown in Table 1. The grinding condition on these materials are shown in Table 2.

These grindings are those that have provided an up-cut and one-way heavy grinding by grindstones with the particle size #80 and #200 (these grindings are hereafter called 80HG and 200HG, respectively) along the longitudinal direction of the specimen. Besides these, those annealed after lapping and those annealed after 200HG have been, respectively, prepared by processing for both materials as standard samples without residual stress. Moreover, precrack materials that have been annealed after inducing the precrack to the lapped materials have also been prepared by Vickers indenter. Since examples where the corners of specimens chipped by 80HG were observed in case of alumina, those that were ground on both surfaces after 80HG (80HG-SG) were also prepared. Specimens annealed after 80HG were prepared in case of silicon nitride. Moreover, the annealing of specimens for both alumina and silicon nitride was conducted in vacuum for 2 hours at 1,200°C.

Table 1. Mechanical Properties of Test Specimens

Material	Bulk density ρ (g/cm^3)	Young's modulus E (GPa)	Poisson's ratio ν
Al$_2$O$_3$	3.80	359	0.220
Si$_3$N$_4$	3.25	272	0.259

Table 2. Grinding Conditions for Test Specimens

Material		Grinding wheel	Setting depth Δ (μm)	Normal force F_n (N/mm)	Tangential force F_t (N/mm)
Al$_2$O$_3$	80HG	#80	40	25.5	5.8
	200HG	#200	25	10.5	2.8
Si$_3$N$_4$	80HG	#80	40	56.3	14.3
	200HG	#200	25	16.9	5.3

#80=SDC80R100B   #200=SDC200N100B

The size of these specimens was ultimately made of a shape with the height of 3.4 mm, width 4 mm, and length 54 mm, and a four-point bending test was conducted after the X-ray residual stress measurement.

2.2 X-Ray Stress Measurement

The X-ray stress measurement conditions of specimens are shown in Table 3. The X-ray stress measurement was conducted for sintered alumina by using the (2.1.10) plane by means of the FeKα characteristic X-ray and for silicon nitride by using the (411) plane by means of the CrKα characteristic X-ray. The parallel inclination method by the parallel beam slit system was the stress measuring method and it was in accordance with the ψ fixed method. The 5° intervals from 0° to 45° were made the standard for ψ setting.

Table 3. X-Ray Conditions for Stress Measurement

Method	Parallel beam method	
Material	Al_2O_3	Si_3N_4
Characteristic X-ray	FeKα	CrKα
Diffraction plane	(2.1.10)	(4 1 1)
Diffraction angle	152.34 deg	125.58 deg
Filter	Mn	V
Tube voltage	40 kV	50 kV
Tube current	30 mA	30 mA
Divergent angle	0.64 deg	0.64 deg
Irradiated area	4 x 4 mm^2	4 x 4 mm^2
Scanning speed	1 deg/min	1 deg/min
Preset time	2 sec	2 sec

The X-ray stress measurement device that had built a prototype of the ψ controller for the general purpose X-ray diffractometer (Shimadzu XD-3A) controlled the diffractometer and ψ controller from the personal computer (NEC PC-9801) through W-BUS and recorded the diffraction angle and diffraction strength on the floppy disk of the personal computer. This diffraction strength data was smoothing treated by the Savitzky-Golay method[6] (secondary and tertiary treatments of nine points) and nine-point moving mean method. Moreover, a background treatment and Lorentz bias factor treatment were provided.
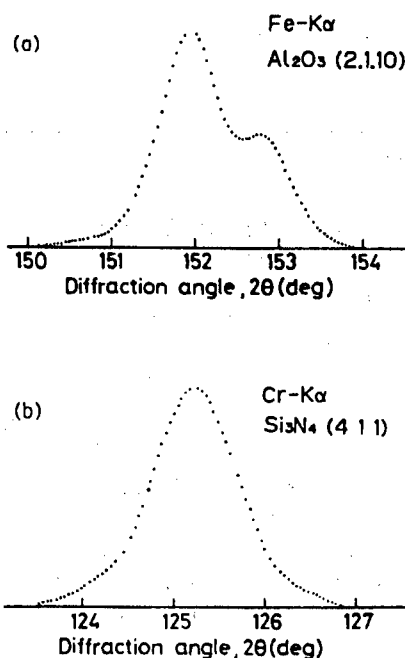
Figure 1. X-Ray Diffraction Profile (a) Al_2O_3 (b) Si_3N_4

The X-ray diffraction profile of silicon nitride and sintered alumina annealed after lapping is shown in Figure 1. This profile is one that has been background treated after smoothing the diffraction data. As known from this diagram, the two-fifth value breadth midpoint method has been used in the peak determination as the diffraction line is separated into $K\alpha_1$ and $K\alpha_2$ in case of alumina. The slope of 2θ-$\sin^2\psi$ diagram was obtained from the diffraction angle 2θ in each ψ and the residual stress was obtained by multiplying the stress constant to this. Moreover, measurement of the residual stress was conducted in the longitudinal direction stress. The stress constants used for X-ray stress measurement in this research are those obtained by the previous experiment. The stress constant of sintered alumina is -601 MPa/deg[7] and that of silicon nitride is -1106 MPa/deg.[2]

2.3 Stress Intensity Factor

As shown in Figure 2, the interior, surface, and corner were made the starting point of flaws and the flaw shape was approximated by an ellipse in the computation of the stress intensity factor. In other words, the stress intensity factor was obtained by approximating the semielliptic surface crack, including the flaw in case of surface defect, by approximating the elliptic crack including the flaw in case of interior defect and by approximating the one-fourth elliptic crack in the case damaged from the corner. The stress intensity factor was obtained by the following formula:

$$K = \sigma \sqrt{\pi a} \, F_0 \tag{1}$$

Figure 2. Approximation of Flaw in Shape of Ellipse
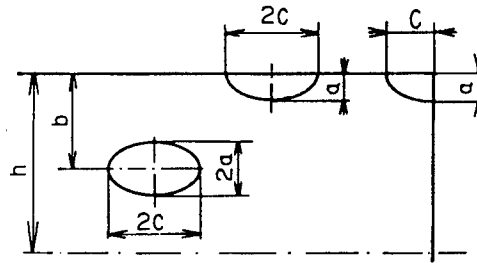
Here, the correction coefficient F_0 was determined as follows by the fracture shape of the defect.[8,9]

Case of elliptic interior crack

$$F_0 = \frac{1}{\Phi_0(k)}\left\{\frac{a+b}{h} M_1 + \frac{a}{h} M_L\left[1 + \frac{k^2 \Phi_0(k)}{(1+k^2)\Phi_0(k)-(k')^2\Phi_1(k)}\right]\right\} \tag{2}$$

Case of semielliptic surface crack

$$F_0 = \frac{1}{\Phi_0(k)} M_R \tag{3}$$

Case of one-fourth elliptic crack

$$F_{\theta} = \frac{1}{\Phi_1(k)}\sqrt{\frac{a}{c}} \ \frac{1.3\sigma_1 + 0.4\sigma_b}{\sigma} \tag{4}$$

Here, $k = \sqrt{1-(a/c)^2}$, $k' = \sqrt{1-k^2}$, and $\Phi_1(k)$ is the perfect elliptic integral of the first kind and $\Phi_2(k)$ is the perfect elliptic integral of the second kind.

3. Experimental Results and Discussion

3.1 Surface Residual Stress and Bending Strength of Ground Materials

The residual stress, two-fifth value breadth and bending strength of alumina are shown in Table 4. The 68.3 percent confidence limits is shown for the surface residual stress values. Moreover, the mean values and standard deviations under various conditions are also shown. The bending strength was obtained by the four-point bending test, the crosshead speed was 0.5 mm/min and the span interval was 22 mm.

Table 4. Residual Stress Measured on 80HG, 200HG, and Annealed Surface of Al$_2$O$_3$

Material	Al$_2$O$_3$			
Condition	Specimen number	Residual stress σ_R(MPa)	2/5 value breadth (deg)	Bending strength σ (MPa)
Annealed	9-1	7.2± 9.2	1.609	353
	9-2	-4.1±13.5	1.623	328
	16-1	-21.2±16.9	1.625	326
	16-1	-13.2± 6.8	1.632	352
	16-2	9.9±17.2	1.620	327
	mean	-4.3± 5.3	1.622±0.0034	337± 5.6
200HG	41-2	-66.8±20.7	1.702	388
	42-1	-65.1±13.9	1.703	354
	42-2	-63.9±10.5	1.699	396
	44-1	-40.6±14.5	1.730	352
	45-1	-79.1±11.6	1.697	404
	mean	-63.1± 5.6	1.706±0.0054	379± 9.7
80HG	11-1	-117.5±20.7	1.746	358
	11-2	-103.5±15.2	1.772	347
	13-2	-83.6±11.4	1.739	313
	14-2	-105.5±12.6	1.767	306
	15-1	-106.0±16.0	1.756	356
	mean	-103.2± 6.9	1.756±0.0055	336± 9.9
Side-ground after 80HG	12-1	-115.0±16.6	1.772	330
	12-2	-101.4±17.8	1.742	312
	14-1	-69.7±13.2	1.740	344
	15-2	-79.5±10.4	1.749	378
	mean	-90.4± 9.3	1.751±0.0064	341±11.7
Annealed after 200HG	43-1	-1.1±13.6	1.584	332
	43-2	-32.2± 7.6	1.594	342
	44-2	-4.9± 6.9	1.594	360
	45-2	-12.6±13.1	1.600	308
	mean	-12.6± 6.0	1.593±0.0029	321± 6.6
Vickers indented	16-2	10.9± 4.5	1.564	211
	17-1	-15.7± 9.2	1.563	215
	17-2	2.3±10.7	1.560	177

It was known that residual stress practically does not exist in annealed specimens of alumina. Moreover, the surface compressive residual stress becomes larger from 200HG to 80HG. It has been confirmed that the residual stress value is also not affected when changing the cutting depth at grinding by a grindstone of the same particle size.[4,10] It is known that the annealed 200HG material has lost its residual stress by annealing. the value of two-fifth value breadth shown here is the mean value obtained from 10 profiles at 5° interval from 0° to 45°. The surface of Vickers indented specimen has been buffer ground after lapping. The size of the two-fifth value breadth value is almost in proportion to the size of the residual compressive stress. With the exception of those inducing the Vickers indentation, we find that the 200HG material with a greater compressive residual stress has a greater bending strength when comparing the bending strength of the annealed material and 200HG material. However, the bending strength of 80HG does not become greater than that of the annealed material despite the fact that it has a greater compressive residual stress. The bending strength has resulted in a smaller value than the annealed material on specimen numbers 13-2 and 14-2. This fact suggests the induction of a large defect when subjected to strong grinding even though the compressive residual stress itself may be great in the 80HG material.

Table 5. Residual Stress Measured on 80HG, 200HG, and Annealed Surface of Si_3N_4

Material	Si_3N_4			
Condition	Specimen number	Residual stress σ_R(MPa)	Half value breadth (deg)	Bending strength σ (MPa)
Annealed	11-2	-31.2±41.6	1.128	601
	15-1	-46.1±23.2	1.102	590
	15-2	-21.9±33.8	1.106	509
	16-1	-55.2±19.7	1.102	534
	16-2	-62.5±15.4	1.141	514
	mean	-39.4±5.2	1.116±0.0072	550±17.2
200HG	1-2	-209.7±50.6	1.304	605
	2-1	-196.9±40.7	1.286	638
	2-2	-157.7±37.6	1.292	628
	3-1	-234.8±79.7	1.330	619
	3-2	-162.2±29.4	1.321	609
	mean	-192.2±13.0	1.307±0.0075	620±5.4
80HG	4-1	-483.9±59.7	1.476	618
	4-2	-522.0±50.7	1.488	587
	6-1	-504.2±59.6	1.503	561
	7-1	-667.3±86.9	1.601	561
	8-1	-525.9±49.1	1.602	585
	mean	-540.7±29.1	1.534±0.0249	582±9.4
Annealed after 200HG	9-1	-38.3±21.6	1.229	666
	9-2	-32.6±17.5	1.233	575
	10-1	-23.3±35.0	1.238	609
	10-2	-55.4±40.6	1.194	567
	mean	-40.0±4.6	1.224±0.0087	609±17.5
Annealed after 80HG	5-2	-41.2±29.6	1.271	528
	6-2	-256.6±37.2	1.307	470
	7-2	-165.6±18.1	1.297	558
	8-2	-193.8±27.0	1.326	275
	mean	-164.8±39.3	1.300±0.0099	458±55.1
Vickers indented	17-1	-25.8±26.1	1.129	340
	17-2	17.3±19.5	1.113	304

The residual stress, half value breadth and bending strength of silicon nitride are shown in Table 5. Practically the same tendency seen in the alumina case is also observed in these values. When comparing the residual stress and half value breadth of annealed materials with those of annealed 80HG materials, it seems that the residual stress could be made to completely disappear by annealing at 1,200°C for 2 hours. Here too, compressive residual stress increases when the particle size of the grindstone becomes larger. The effect of the residual stress has appeared in the improvement of the bending strength for the 200HG material but since an improvement is not seen in the bending strength for the 80HG material, it is believed that the size of the defect has become greater in the same manner as in the case of alumina.

3.2 Undersurface Distribution of Grinding Residual Stress

We have already mentioned the surface residual stress caused by grinding in the preceding chapter and what kind of distribution the residual stress has in the depth direction is important when considering the fracture strength of ceramics. Therefore, the surface layers were gradually removed and an X-ray stress measurement was conducted to check the depth direction distribution of the residual stress value. Moreover, the values of the measured residual stress were corrected by the redistribution effect of residual stress by the removal from the surface.[11] The residual stress σ_R which has been corrected of the residual stress change by the surface removal is expressed by the following formula:

$$\sigma_R(z_1) = \sigma_{Rm}(z_1) + 2\int_{z_1}^{H} \frac{\sigma_{Rm}(z)}{z}dz - 6z_1 \int_{z_1}^{H} \frac{\sigma_{Rm}(z)}{z^2}dz \tag{5}$$

The coordinates and variables are as shown in Figure 3. z_1 is the height from the surface not removed, H is the height of the surface before removal and σ_{Rm} is the measured residual stress. The depth direction residual stress distribution was obtained by using the following formula which has approximated the right side second and third terms that are the correction terms of formula (1) by the first term of Taylor's expansion.

$$\sigma_R(z_1) = \sigma_{Rm}(z_1) - 4\sigma_{Rm}(H)\frac{H-z_1}{H} \tag{6}$$
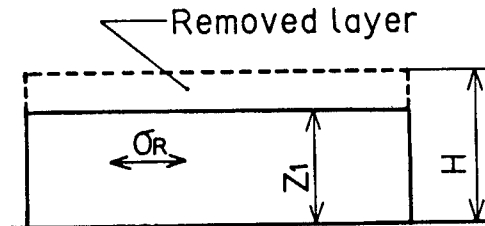
Figure 3. Flat Plate After Surface Removed

The depth direction distribution of 80HG and 200HG residual stresses of alumina is shown in Figure 4(a). Figure 4(b) similarly shows the case of silicon nitride. Both alumina and silicon nitride have a roughly matched tendency. The maximum compressive residual stress is shown at the depth of 5 μm and the residual stress by grinding disappears around the depth of 25 μm. This tendency coincides regardless of the material being 80HG or 200HG. However, the 200HG material shows a lower residual stress distribution than that of the 80HG material. The X-ray penetration depth in alumina is 14~21 μm in case of the (2.1.10) plane by Fekα radiation, and it is 11~16 μm in silicon nitride in case of the (411) plane by CrKα radiation. Since the residual stress becomes the mean stress in the X-ray penetration depth, the different diffraction planes, materials, and residual stress values of X-ray is not simply comparable. The 80HG material of silicon nitride shows an especially large value and the compressive residual stress of two to three times is shown in comparison to the case of 200HG. The compressive residual layer is not affected much by the processing difference and it is 20~30 μm.

(a) Al$_2$O$_3$

(b) Si$_3$N$_4$

Figure 4. Residual Stress Distribution of Ceramics Ground

The change of two-fifth value breadth toward the grinding depth direction of alumina and the change in the half value breadth toward the grinding depth direction of silicon nitride are shown in Figures 5(a) and 5(b), respectively. The diffraction profile spreading becomes smaller as it becomes deeper from the surface for both alumina and silicon nitride and the

86

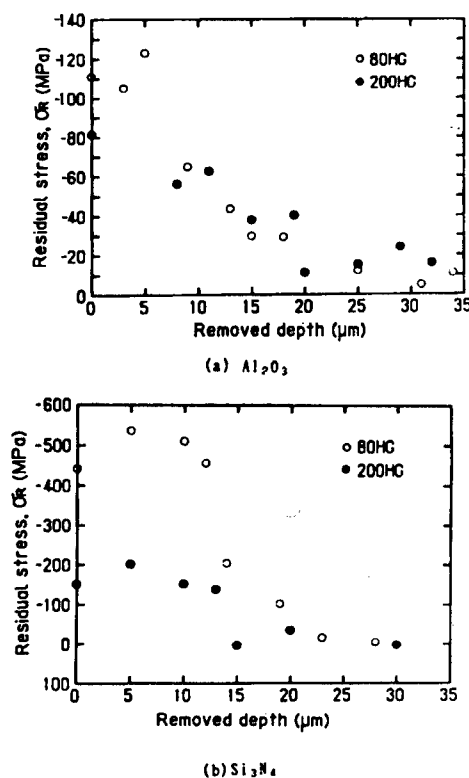profile spreading converges in the neighborhood where the residual stress becomes nil. The diffraction profile spreading has practically the same tendency as the residual stress. However, it also has the characteristic of showing the maximum residual stress in a place with the depth of 5 μm.

3.3 Identification of Fracture Origin by Fractography

Examples of scanning electron microscope (SEM) photos of alumina are shown in Figure 6 [not reproduced]. Figure 6(a) [not reproduced] is a general image of an alumina fracture of annealed materials. A radial pattern spreads toward the fracture advancing direction from the photo upper tensile side. The fracture origin is known by tracing this radial pattern to the tensile side.
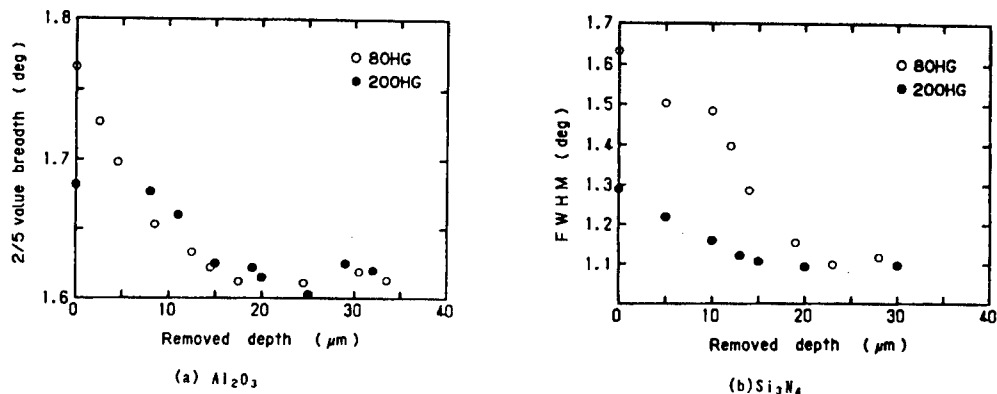
Figure 5. Change in Breadth of X-Ray Diffraction
Profile of Ceramics Ground

Blow holes as shown in Figure 6(b) [not reproduced] exist in sintered alumina and there are many cases when these blow holes became the origin of fractures. Most fracture patterns in the neighborhood of fracture origins were transgranular fractures and they changed to intergranular fractures as they were distanced from the origins. The fracture origins were dominant on the surface in annealed materials. Both surface and internal origin fractures were seen in the 200HG material and all annealed 200HG materials were of surface fractures. One example of the surface origin fracture was seen in the 80HG material and others were of internal origin fractures and those that were cracked due to the corner of the specimen receiving a flaw at grinding and becoming fractured from this flaw.

Examples of scanning electron microscope photos of silicon nitride are shown in Figures 7(a) and (b) [not reproduced]. This fracture is that of silicon nitride annealed after 200HG. The position relation of the fracture shape and fracture origin seen in alumina was also the same as in silicon nitride. Moreover, the mean particle diameter measured from the scanning electron microscope photos of fractures was 2.8 μm for alumina and 0.42 μm for silicon nitride.

3.4 Relationship Between Bending Strength and Flaw Size

Since the crack size and fracture stress are not comparable with the position and shape of the fracture origin remaining different, the fracture origin was identified from the scanning electron microscope photos and the equivalent crack length a_e was computed from K obtained in Chapter 2.3. Equivalent crack length means the crack length in an infinite plate under a uniform stress σ that is equal to K of the specimen fractured in the bending test. In this case, the relationship between the representative flaw size a and the equivalent crack length a_e is as follows:

$$a_e = a \cdot F_0^2 \tag{7}$$

(a) Al_2O_3

(a) Al_2O_3

(b) Si_3N_4

(b) Si_3N_4

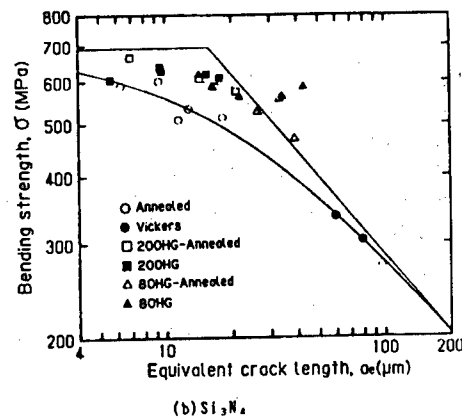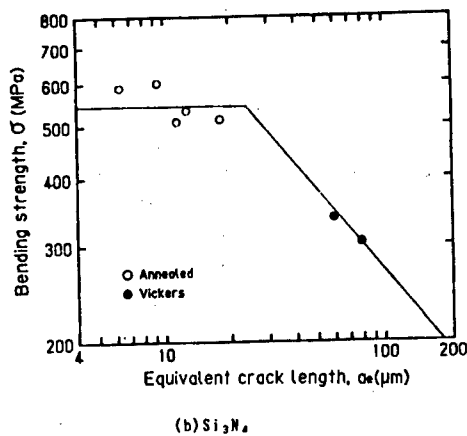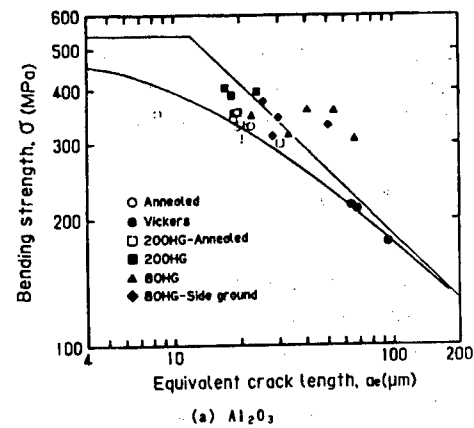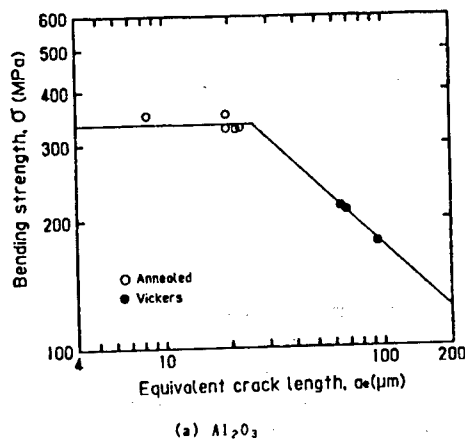Figure 8. Relation Between Equivalent Crack Length and Bending Strength for Specimens Annealed and Precracked

Figure 9. Relation Between Equivalent Crack Length and Bending Strength

The relationship between the equivalent crack length a_e and bending strength obtained from formula (7) are, respectively, shown in Figures 8(a) and (b) for alumina and silicon nitride. The results of annealed and precracked

specimens were used in the diagram for observing the relationship between the equivalent crack length a_e and representative flaw size σ based on specimens free from the effect of residual stress. The line according to the mean value of annealed specimen bending strength and fracture toughness value Kc obtained from the precracked specimen is shown in the diagram. Kc of alumina was 3.06 MPa and Kc of silicon nitride was 4.07 MPa. It can be said that the fracture mechanical arrangement using the equivalent crack length of alumina and silicon nitride is effective from this diagram.

3.5 Strength Evaluation Model

Diagrams that have arranged the relation between the equivalent crack length and bending strength by also including the results of specimens with a residual stress are shown in Figures 9(a) and (b).

Moreover, since the ceramics interior is not free from faults, it can be considered that potential flaws exist. Therefore, the fictitious crack length a_0 expressed by the following formula and the curve by the fracture toughness value Kc are shown together in Figure 9.

$$\sigma = \frac{Kc}{\sqrt{\pi (a_e + a_0)}} \tag{8}$$

The fictitious crack length a_0 and fracture toughness value Kc were obtained by the minimum squares method from the results of the precracked specimen by Vickers indentation. Moreover, A_0 was 12.2 μm and Kc was 3.29 MPa $\sqrt{m}$ for alumina and a_0 was 18.8 μm and Kc was 5.31 MPa $\sqrt{m}$ for silicon nitride. Since the size of a_0 is considerably greater than the mean particle diameter of both alumina and silicon nitride, it is considered that the physical meaning of a_0 is closer to the blow hole diameter than the crystal particle diameter.

Figure 9(a) shows the relationship between the bending strength and equivalent crack length of alumina. The 200HG specimen is positioned at a place of higher bending strength than the annealed specimen due to the compressive residual stress effect. Moreover, the annealed 200HG material is positioned in a similar place as the annealed specimen due to the loss of the residual stress. Although the flaw size has become larger by the intense grinding effect in case of 80HG, it is known that the fracture stress has been improved more for the 80HG specimen by the compressive residual stress than that of the precracked specimen by Vickers indentation.

Figure 9(b) shows the relationship between the bending strength and equivalent crack length of silicon nitride. It can be considered that the flaws of heavy grinding by 200HG were small from the fact that the equivalent crack length a_e did not move as much in the 200HG specimen of silicon nitride as compared to alumina.

A good coincidence was seen between the experiment results of annealed alumina and silicon nitride and the fracture mechanical concept of the fictitious crack length and equivalent crack length. Therefore, an estimation model of the bending strength when stress existed was introduced and studies were made on how the residual stress affected the bending

strength. To put it concretely, the semicircular crack bending strength was analyzed when compressive residual stress existed on the surface layer as shown in Figure 10.

When the stress intensity factor by the applied stress is made K_{aDD} and the stress intensity factor by residual stress is made K_{res}, the condition is expressed as follows when supposing that the fracture occurs when the sum of the stress intensity factors become Kc at the fictitious crack tip:

$$K_{aDD} = Kc - K_{res} \tag{9}$$

Moreover, it becomes as follows when expressing concretely the stress intensity factor K_{aDD} including the fictitious crack:

$$\sigma = \frac{Kc}{\sqrt{\pi (a+a_0)}\ F(a+a_0)}\ (1- \frac{K_{res}}{Kc}) \tag{10}$$
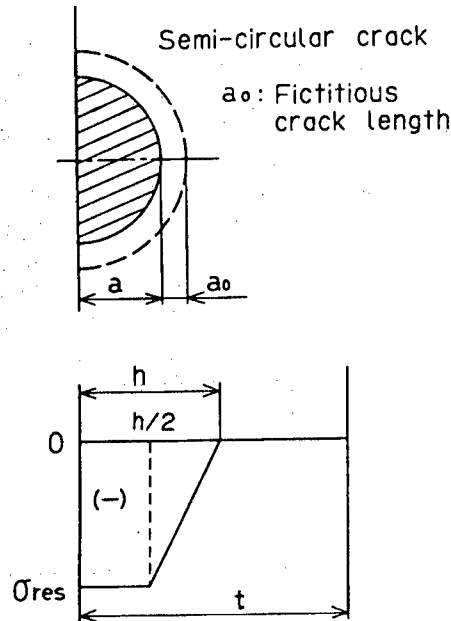
Figure 10. Semicircular Crack and Residual Stress Distribution
for Strength Estimation Model

It further becomes as follows when the fracture stress is made σ_T in case cracks do not exist and fictitious cracks only are contained in the material:

$$Kc = \sigma_T \sqrt{\pi\ a_0}F(a_0) \tag{11}$$

The strengthening ratio σ/σ_T of the bending strength by the residual stress is available by the following formula when substituting this in formula (10) and arranging the formula:

$$\frac{\sigma}{\sigma_T} = \sqrt{\frac{a_0}{a+a_0}}\ \frac{F(a_0)}{F(a+a_0)}\ (1- \frac{K_{res}}{Kc}) \tag{12}$$

The following formula by weight function was used as the analysis method of the stress intensity factor by residual stress:

$$K_{res} = \frac{E/(1-\nu^2)}{K_0} \int_a^\cdot \sigma_R \frac{\partial u}{\partial a} \cdot dx$$

(13)

Here, K_0 and u_0, respectively, apply to the stress expansion factor and crack opening displacement by using uniform tension.[12] When supposing the trapezoid residual stress distribution shown in Figure 10 and expressed by the following formulas as the residual stress value σ_R, the residual stress value σ_R is made zero in places where x is deeper than the residual stress layer h.

$$\sigma_R (x) = \sigma_{res} \qquad (0 \leq x < h/2) \tag{14}$$

$$\sigma_R (x) = 2\sigma_{res} (1-x/h) \qquad (h/2 \leq x < h) \tag{15}$$

Parameters that determine the problem are the fictitious crack length a_0, residual stress layer ratio h/t, residual stress value ratio R ($= \text{Al2res}/\sigma_T$), sectional shape ratio t/w and ratio a_0/h between the fictitious crack length and residual stress layer thickness. The computation result of the bending strength strengthening ratio when $a_0 = 20$ μm, $h/t = 6.7 \times 10^{-3}$, R = 0--1, $t/w = 1$, and $a_0/h \doteq 0.5$ is shown in Figure 11. It is known from this diagram that the bending strength becomes higher as the compressive residual stress becomes larger and improvement of the bending strength is seen especially for the crack length that is equivalent to the residual stress layer depth. Moreover, the effect reduces when the crack becomes longer than the residual stress layer. It can be said from this that the compressive residual stress contributes to the improvement of bending strength but the degree of contribution is controlled by the size and depth of the compressive residual stress.
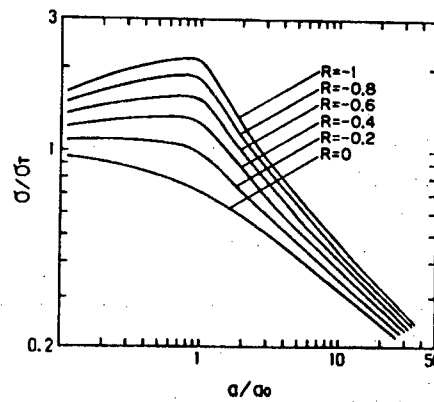

Figure 11. Relation Between Bending Strength Ratio σ/σ_T and Crack Length Ratio a/a_0 for Various Residual Stress Ratio R

4. Conclusion

The surface and depth direction residual stresses were measured by the X-ray stress measurement by inducing the grinding residual stress of atmospheric sintered alumina and silicon carbide. Moreover, a bending test was conducted, identification of cracks was conducted by fractography after measuring the bending strength, and fracture mechanical studies were conducted. The results obtained by conducting these are as follows:

(1) A compressive residual stress was formed on the surface of ceramics by grinding and the grinding depth was about 20~30 μm.

(2) The compressive residual stress by grinding improves the bending strength of ceramics, however, the flaw size is increased and the bending strength is sometimes lowered inversely when the processing is too intense. An improvement of bending strength was seen in those of 200HG for both alumina and silicon nitride in this research.

(3) Upon using the equivalent crack length and fictitious crack from the fracture mechanical standpoint in the arrangement of the bending strength and fracture flaw, they showed good coincidence with these concepts.

(4) A strength estimation model using a fictitious crack for the semicircular surface crack when there was a compressive residual stress has been proposed.

References

1. Keishi Tanaka, Eiji Matsui, and Yoshiaki Akiba, MATERIALS, Vol 35, 1986, p 794.

2. Keisuke Tanaka, Takayuki Kurimura, Eiji Murai, and Yoshiaki Akiba, Ibid., Vol 36, 1987, p 817.

3. Hidehiro Kishimoto, Akira Ueno, Yo Kawamoto, and Shini Kondo, Ibid., p 810.

4. Kenji Suzuki, Keisuke Tanaka, and Heizaburo Nakagawa, Manuscripts of lecture theses for the 24th Symposium on X-Ray Material Strength, 1987, p 41.

5. Keisuke Tanaka, RESEARCH OF MACHINES, Vol 40, 1988, p 265.

6. A. Savitsky and M.J.E. Golay, ANALYTICAL CHEMISTRY, Vol 36, 1964, p 1627.

7. Kenji Suzuki and Keisuke Tanaka, MATERIALS, Vol 37, 1988, p 586.

8.   R.C. Shah and A.S. Kobayashi, ASTM STP 513, 1972, p 3.

9.   A.S. Kobayashi and A.N. Enetanya, ASTM STP 590, 1974, p 477.

10.   Takayuki Kimura, Keisuke Tanaka, Yoshiaki Akiba, Kenji Suzuki, and
      Heizaburo Nakagawa, Manuscripts of lecture theses for the 24th
      Symposium on X-Ray Material Strength, 1987, p 35.

11.   "Residual Stress Measurement by X-Ray Diffraction," SAEJ784a, 1971,
      p 62.

12.   C. Mattbeck, P. Morawietz, and D. Munz, INTERNATIONAL JOURNAL OF
      FRACTURE, Vol 23, 1983, p 201.

Neural Network Learning Algorithms

[Article by Takashi Kimoto, Shigemi Nagata, Minoru Sekiguchi, Hideki Yoshizawa, Nobuo Watanabe, and Kazuo Asakawa of Fujitsu Laboratories, Ltd.]

[Text] The neurocomputer is a "flexible" data processing element modeled on the human brain. It consists of a network of many interrelated neuron elements that operate in parallel and is able to learn.

We will focus on a multihierarchical neural network model based on the stratified structure of the human brain. We have developed a network learning algorithm, pseudo impedance control, and evaluated this learning algorithm. This paper describes the principles of operation and this learning algorithm model.

1. Preface

The human brain is an information processing unit consisting of 14 billion neurons or more. An enormous number of these neurons are complexly combined with each other, form a neuron network, and can realize advanced parallel distributed processing.

The neurocomputer is an approach to realizing a truly "soft" information processing unit by regarding the brain as a model. Learning functions equivalent to those of human beings can be realized by automatically adjusting the strength (weight) of the neuron elements-high speed movement combination of the neurocomputer having a structure in which many neuron elements moving in parallel are combined.

This manuscript describes learning algorithms and the principle of operation of a neural network model, which will become the core of a neurocomputer, while giving attention to a hierarchical network.

2. Neural Network and Learning

2.1 Model of Neuron

Figure 1 shows an engineering model in which the operation of neurons is regarded as an information processing functional element. The unit processes signals emitted from the input side on the basis of weighted majority logic, and emits an output signal. This output signal is used as an input signal for many other units. In this model, two processing methods, i.e., a product and sum operation of input signals and weight and a threshold processing method, are regarded as basic characteristics of neurons. As shown below, the use of a sigmoid function will formulate the input and output characteristics of the units.

$$x_j(t) = \sum_i y_i(t) w_{ji}(t). \tag{1}$$

$$y_j(t) = 1/(1 + \exp\{-x_j(t) + \theta_j(t)\}) \tag{2}$$

Where,

- x_j : Total input
- y_j : Output of unit j
- θ_j : Bias value of unit j
- y_i : Output of unit i combined at the input side of unit j
- W_{ji}: Weight of unit i and unit j combination
- t : Number of learned items (renewal only of weight)

$$x_j = \sum y_i W_{ji}$$

$$y_j = \frac{1}{1 + e^{(-x_j + \theta_j)}}$$
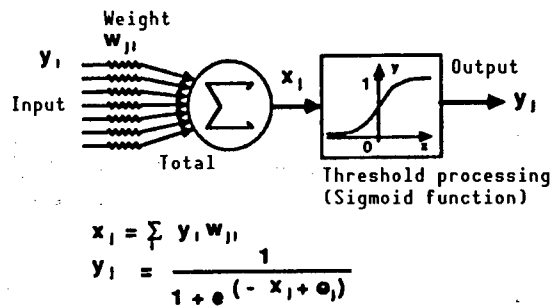
Figure 1. Model of Neuron

2.2 Neural Network

The neural network is a calculation model in which the above-mentioned units are combined. Now, we will briefly explain the operational principle of a hierarchical network made by imitating the lamellar structure of cerebral cells.

Figure 2 shows a hierarchical network structure consisting of the input layer, intermediate layer, and output layer. Respective units in the hierarchical network are combined, in order, from the input layer to the intermediate layer and from the intermediate layer to the output layer, with

no combinations in this network occurring within layers or from the output layer to the input layer.

When an input pattern is given to the input layer, each unit of the input layer will transfer its input signal to the intermediate layer. Each unit of the intermediate layer will operate on the basis of equations (1) and (2), and will transfer an output signal to each unit of the output layer, and finally, output patterns of the network will be output from each unit of the output layer.
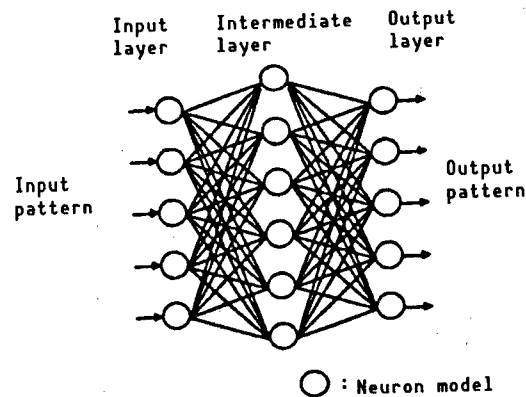
Figure 2. Hierarchical Network

2.3 Learning Algorithm

●   **Method of Controlling Virtual Impedance**

With regard to a learning algorithm involving rapid convergence, we have devised a method for handling the network's behavior as a secondary forced vibration system from the analogy with a mechanical vibration system. This is called the "virtual impedance controlling method." The network learning task is to ascertain which desirable output patterns (instructor signals) of W aggregate coincide with (or closely resemble) the output patterns actually output by the network against individually given input patterns. The "back propagation method," proposed by Rumelhart, et al.,[1] is well known as a learning method for such a hierarchical network. In this method, the error feedback shown in Figure 3 is introduced into the hierarchical network, and the weight of combination, w, and bias value, θ, are adaptively and automatically adjusted based on this error feedback. As a result, the network will learn a combination of input and output patterns, and will be able to realize adaptive data processing.

The virtual impedance controlling method is a system succeeding the basic philosophy of the back propagation method and adopts the establishment of a parameter by noting the analogy with the mechanical vibration system. As a result, it is possible to carry out learning at a higher speed.
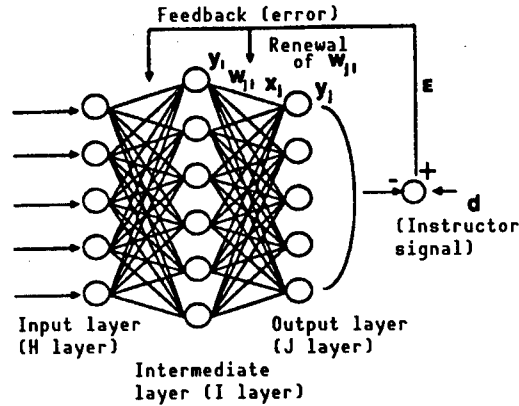
Figure 3. Neural Network Learning

When a certain input pattern c is given to the network, an error between the actual output value y_j, c(t) and the preferred output value $d_{j,c}$ is defined below.

$$E_c\,(t)=\tfrac{1}{2}\Sigma\,(\ y_{j,c}\,(t)-d_{j,c}\,)^2. \tag{3}$$

Where,

    c: Index of a pair of input and output patterns
    j: Index of output unit

Then, the total error E(t) of the network against all input and output patterns is expressed by the following equation:

$$E(t)=\tfrac{1}{2}\Sigma_c\Sigma_j\,(\ y_{j,c}\,(t)-d_{j,c}\,)^2. \tag{4}$$

In the virtual impedance controlling method, w is renewed in sequence so as to reduce the above error, and finally, when the error between the output value of the output layer units and the preferred output value becomes the specified value or less, the learning will be finished.

As shown below, the algorithm of the virtual impedance controlling method can be definitely explained with reference to Figure 3. The relationship between the input and output of each unit of the network can be expressed by equations (1) and (2).

$$x_{i,c}\,(t)=\Sigma_h\,y_{h,c}\,(t)w_{ih}(t). \tag{5}$$

$$y_{i,c}\,(t)=1/\,[1+\exp\,\{-x_{i,c}\,(t)+\theta_i\,(t)\}\,]. \tag{6}$$

$$x_{j,c}\,(t)=\Sigma_i\,y_{i,c}\,(t)w_{ji}(t). \tag{7}$$

$$y_{j,c}\,(t)=1/\,[1+\exp\,\{-x_{j,c}\,(t)+\theta_j\,(t)\}\,]. \tag{8}$$

Where,
- $y_{i,c}$: Output of units
- $x_{i,c}$: Total input to units
- w_{ih} : Weight of combination of hth unit and i^{th} unit

Where, h, i, and j are indexes which express the hth, i^{th}, and j^{th} of, respectively, the H layer (input layer), I layer (intermediate layer), and J layer (output layer). c is an index of input and output pattern pairs.

In the case of the virtual impedance controlling method, partial differentiation of error (E)t for the respective w(t)s is calculated to minimize this error by using the steepest descent method. The following equations hold from equations (3) and (4):

$$\partial E(t) / \partial w_{ji}(t) = \sum_{c} \partial E_c(t) / \partial w_{ji}(t). \tag{9}$$

$$\partial E(t) / \partial w_{ih}(t) = \sum_{c} \partial E_c(t) / \partial w_{ih}(t). \tag{10}$$

These equations express the rate of change of (E)t against the change of w(t) between the output and intermediate layers and that between the intermediate layer and input layer. Therefore, (E)t can be set asymptotically to zero by changing w(t) so that it is always negative. In the virtual impedance controlling method, the change of time is applied to network behaviors, $-\partial E(t)/\partial w(t)$ is regarded as the following secondary forced vibration system which is an external force, and the learning (weight renewal) number is reduced.

$$M \Delta \ddot{w}(t) + D \Delta \dot{w}(t) + K \Delta w(t) = - \partial E(t) / \partial w(t). \tag{11}$$

Where,
- M : Virtual mass of network
- D : Virtual viscosity damping coefficient
- K : Virtual stiffness of network
- t : Learning (weight renewal) number
- W(t): Weight of combination
- $\Delta w(t)$: Minute change of combination weight w at t
- E(t): Error

Discretely approximating this quadratic differential equation and solving it with respect to $\Delta w(t)$, gives the following equation:

$$\begin{aligned} \Delta w(t) = & \{- \Delta t^2 \partial E(t) / \partial w(t) \\ & + (2M + D\Delta t) \Delta w(t - \Delta t) \\ & - M \Delta w(t - 2\Delta t)\} / (M + D + K\Delta t^2). \end{aligned} \tag{12}$$

This equation is regarded as a quadratic system, but can also be regarded as a more general n system.

Setting $\Delta t = 1$, $M = 0$, $1/(D + K) = \varepsilon$, $D/(D + K) = \alpha$ in equation (12), the virtual impedance controlling method is equivalent to the back propagation method, in which the following learning constant ε and learning speed constant α are introduced.

$$\Delta w(t) = -\varepsilon \, \partial E(t) / \partial w(t) + \alpha \Delta w(t-1). \tag{13}$$

That is, the use of the virtual impedance controlling method will be able to raise the learning convergence speed, because an appropriate combination of ε and α can be selected in consideration of correlation between ε and α as well as the learning acceleration term.

In order to deduce the rate of change $\partial (E)t/\partial w(t)$ of error $(E)t$ against the change of weight $w(t)$ of the combination, all that is necessary is to propagate the differential value of the error from the output layer to the input layer.

First, partially differentiating equation (3) with respect to $y_{j,c}(t)$ to find the relation error $E_c(t)$ and output value of the output layer (J layer) gives the following equation:

$$\partial E_c(t)/\partial y_{j,c}(t) = y_{j,c}(t) - d_{j,c}$$
$$= \delta_{j,c}(t). \tag{14}$$

Then, partially differentiating error $E_c(t)$ with respect to $x_{j,c}(t)$ to determine how the error is affected by the change of total input to output units gives the following equation:

$$\partial E_c(t)/\partial x_{j,c}(t)$$
$$= \delta_{j,c}(t) y_{j,c}(t) \{1 - y_{j,c}(t)\} . \tag{15}$$

Therefore, the relationship between the change of error $E_c(t)$ and that of weight $w_{ji}(t)$ of the combined I and J layers can be expressed by the following equation:

$$\partial E_c(t)/\partial w_{ji}(t)$$
$$= \delta_{j,c}(t) y_{j,c}(t) \{1 - y_{j,c}(t)\} \, y_{i,c}(t). \tag{16}$$

Next, finding the change of error $E_c(t)$ against output value $y_{i,c}(t)$ of the intermediate layer (I layer) gives the following equation:

$$\partial E_c(t)/\partial y_{i,c}(t) =$$
$$\sum_j \delta_{j,c}(t) y_{j,c}(t)$$
$$\cdot \{1 - y_{j,c}(t)\} \, w_{ji}(t). \tag{17}$$

In addition, calculating the change of error $E_c(t)$ against the change of total input $x_{i,c}(t)$ to units of the I layer gives the following equation:

$$\partial E_c(t) / \partial x_{i,c}(t)$$
$$= [\Sigma \, \delta_{j,c}(t) y_{j,c}(t) \{1-y_{j,c}(t)\} \, w_{ji}(t)]$$
$$j$$
$$\cdot y_{i,c}(t) \{1-y_{i,c}(t)\} . \tag{18}$$

Therefore, the relationship between the change of error $E_c(t)$ and that of weight $w_{ih}(t)$ of the combined H and I layers can be expressed by the following equation.

$$\partial E_c(t) / \partial w_{ih}(t)$$
$$= [\Sigma \, \delta_{j,c}(t) y_{j,c}(t) \{1-y_{j,c}(t)\} \, w_{ji}(t)]$$
$$j$$
$$\cdot y_{i,c}(t) \{1-y_{i,c}(t)\} \, y_{h,c}(t). \tag{19}$$

Accordingly, the rate of change of error $E_c(t)$ against the change of weight $w(t)$ of combinations among each layer can be found from equations (9), (10), (16), and (19).

2.4 Simulation

The learning process can be understood as a phenomenon similar to that in which a ball rolls down in the direction of the lower error on a hyperplane which expresses the distribution of E in w space. However, this hyperplane has local minima, which means many minimal values as well as a minimum error value.

The problem involving these local minima has not yet been analyzed theoretically. For this reason, learning convergence has been simulated by appropriately changing each parameter of the network to verify the effectiveness of the virtual impedance controlling method. As a result, it was confirmed that learning converged into the minimum value in almost all trials only when these parameters were set appropriately.

An experimental example is shown below. This is a case in which the exclusive "or" is learned by the three-layer network consisting of two inputs and one output, where, $\Delta t = 1$, virtual mass M of the network = 0, $1/(D + K) =$ learning constant ε, $D/(D + K) =$ learning speed constant α. Actually, the three-layer network consists of three input layers and one output layer, because its input layer has a bias value unit which outputs 1 at all times. Results of this experimental example are shown in Figure 4. In the example, equation (13) was adopted as a learning rule (renewal rule for the weight of combination), and learning constant ε and the number N h of units of the intermediate layer were changed in the state in which the learning speed constant α was fixed at 0.8. The lateral axis shows the value of learning constant ε for every 0.4 pitch. The longitudinal axis shows the number of average learnings in 10 trials carried out for the values of the respective learning constants ε. After four pairs of input and output patterns in the exclusive "or" relationship were indicated in the

network, the procedure for renewing the weight of combination once was regarded as a learning. Therefore, the number of learnings indicates that the number of times the above process is repeated until the total error of the network becomes 10^{-1} or less. Learnings were converged into the minimum value of errors in all trials of the above experiment. Also, the learning speed constant α was established as 0.8, which is quite a large value in this experiment, but it has been confirmed that if the number Nh of units of the intermediate layer is increased and learning constant ε is established appropriately, the learning convergence speed can be increased.
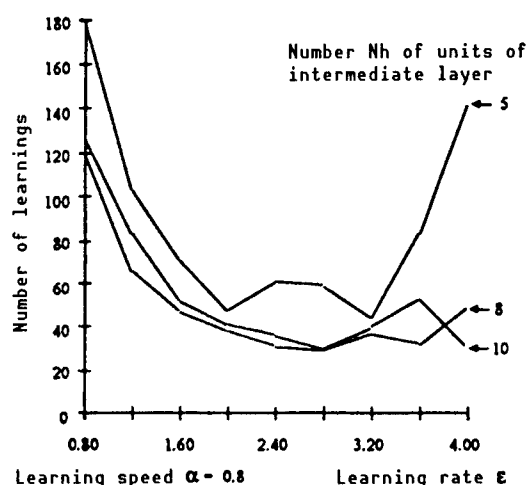
Figure 4. Number of Learnings Required Up to Convergence

However, the optimum values of the learning constant ε and learning speed constant ε greatly depend on the number of units of the input and output layers and the input and output patterns. Accordingly, establishing optimum values for these parameters is an important subject which should be solved in the future.

4. Conclusion

The principle of operation of the neuron network model as a core for neurocomputers has been described, while paying attention to the hierarchical network. In addition, the validity of neurocomputers has been demonstrated by studying learning methods and by carrying out computer simulations.

In the future, we will carry out basic research, such as studying learning methods, and research on applying these learning methods to kinematic control, pattern understanding, etc.

References

1.   D.E. Rumelhart, J.L. McClelland, and the PDP Research Group, "Parallel Distributed Processing: Explorations in the Microstructure of Cognition. Volume 1: Foundations," MIT Press, Cambridge, 1986, pp 318-362.

Neural Network Control of Mobile Robot

[Article by Shigemi Nagata, Minoru Sekiguchi, Hideki Yoshizawa, Nobuo Watanabe, Takashi Kimoto, and Kazuo Asakawa of Fujitsu Laboratories, Ltd.]

[Text] Abstract: A neurocomputer is an experimental device to develop a truly flexible computer by referencing the cerebrum. Neurocomputers are comprised of a number of parallel working neuron elements bound together, and can offer a learning function that behaves similarly to that of human beings in regard to high-speed performance and automatic adjustment of the strength of bonds between neural elements.

A neural network accomplishes a type of processing well adapted to external environments without requiring the network construction to be changed. Accordingly, the adoption of a neurocomputer enables a system to be erected that provides very flexible functions. Various application fields can be considered, for example, motion control, pattern recognition, knowledge treatment, etc.

This paper describes a multilayered network, analogous to the cerebral strata, as a neural network model to serve as the nucleus of the neurocomputer, and an example of its application to robot control will also be described.

1. Preface

The neurocomputer made by modeling a human brain is a flexible information processing unit which can realize advanced parallel distribution processing and learning functions by the network in which many neural elements are combined in parallel. Research on various matters, such as motion control, pattern understanding, and knowledge processing, is being carried out, because it is expected that the use of such neurocomputers will bring about systems offering extremely flexible functions. The validity of these neurocomputers has been demonstrated by using a neural network to control a compact locomotive robot. This manuscript reports on this validity.

2. Neural Network and Learning

2.1 Hierarchical Network Model

The hierarchical network is a neural network model made by lamellately combining many neuron models, called "units." Figure 1 shows a hierarchical network structure consisting of three layers--the input layer, intermediate layer, and output layer. In the hierarchical network, a constant conversion rule (data processing method), depending on the weight of combination among units, is applied to an input pattern by conducting forward processing, proceeding from the input layer to the output layer at all times and, after the conversion, a pattern is output from the output layer.

One feature of the neural network is that various data can be processed by adaptively and automatically adjusting the above-mentioned weight of combination. Network learning involves adapting the weight, and is an important key in making the network flexible.

2.2 Learning Algorithm

● **Virtual Impedance Controlling Method**

The purpose of the learning algorithm is to determine the aggregation of the weight of combination which minimizes the error between the target pattern (instructor signal) and the pattern actually output by the network against respectively given input patterns. Then, the weight of combination is automatically adjusted by using the error feedback shown in Figure 1, and by conducting a backward processing which proceeds from the output layer to the input layer. As a result, the network can learn a corresponding relationship between the desired input patterns and the output ones, and can process data adaptively. The authors have treated the renewal algorithm of weight of combination as the secondary forced vibration system below which shows the network behavior as analogous to a mechanical vibration system, and have proposed a learning algorithm called the virtual impedance controlling method.

$$M \Delta w(t) + D \Delta w(t) + K \Delta w(t)$$
$$= - \partial E / \partial w(t) \tag{1}$$

$$\Delta w(t) = -(1/M + D + K) \partial E / \partial w(t)$$
$$+ (2M + D/M + D + K) \Delta w(t-1)$$
$$- (M/M + D + K) \Delta w(t-2) \tag{2}$$

Where,
- M : Virtual mass of network
- D : Damping coefficient of viscosity of network
- K : Stiffness of network
- w : Weight of combination
- E : Square sum of error
- Δw: Degree of change of weight
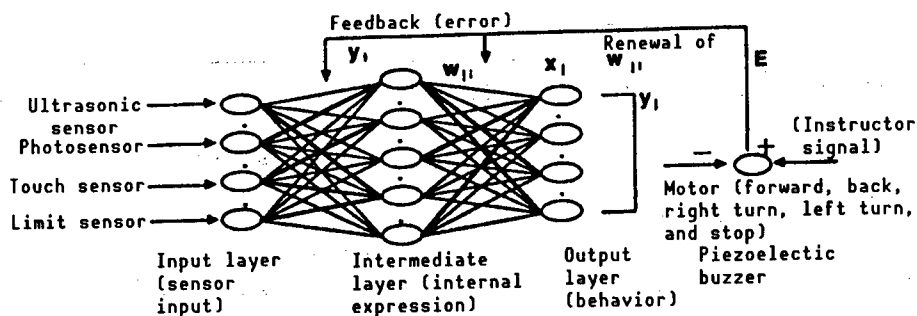- t : Number of learnings (renewal of weight)

Figure 1. Hierarchical Network Model

3. Motion Learning Control of Robot

3.1 Compact Locomotive Robot "Satoru-kun"

A compact locomotive robot, "Satoru-kun," has been developed to demonstrate the "flexibility" of the neural network. The following system has been developed, i.e., a neural network is mounted on such robots, various behavior patterns are memorized in them, and they chase each other. Figure 2 [not reproduced] shows a diagram of the above-mentioned compact locomotive robot, Satoru-kun, and Table 1 presents its main data. Satoru-kun has four wheels and two motors (one is for propelling and the other for steering), and can locomote while simultaneously steering the four wheels in the same direction. It is also equipped with various sensors, such as a photosensor and ultrasonic sensor, to recognize the external environment and its internal situations. There are two purposes for developing this demonstration system. One is to demonstrate the learning ability of the neural network. In order to do so, Satoru-kun must learn its behavior patterns through the neural network on the basis of information from various sensor inputs, and must show that it can take actions appropriately in accordance with the external environment. The other is to demonstrate the flexibility of the neural network. In order to do so, it is necessary to change the corresponding relationship between the sensor input information and behavior patterns and to produce another robot with the same structure as that of Satoru-kun, but with different habits (behavior patterns).

3.2 Demonstration System--Chasing of Robots

Figure 3 [not reproduced] shows a photograph in which robots equivalent to Satoru-kun are chasing each other. Satoru-kun can become a chasing robot and an escaping robot by learning different behavior patterns. The chasing robot and escaping robot have been named "Holmes" and "Lupin," respectively. Holmes searches and chases the escaping Lupin by using its ultrasonic sensor and photosensor. The head of the Lupin is equipped with an ultrasonic transmitter with a frequency of 40 kHz and four light emitting diodes [LED] in four directions at 90-degree intervals. The Lupin detects light emitted from an LED installed on the abdominal region of the Holmes by using a photosensor installed in its abdominal region, and therefore is able to escape. That is, the behavior involving being attracted to light and

Table 1. Main Data on Satoru-kun

Maximum acceleration	0.9 m/s^2	LED		16
Maximum speed	1.0 m/s	Mounted sensors	Photosensors	4
Steering speed	142°/s		Ultra sonic sensors	23 kHz	1
MPU	MB89702		40 kHz	2
Power source section	2 batteries 6 V in series each		Tactile sensors	2
			Limiting sensors	3
Travel steering system	ON-OFF control by DC motor		Total	12
Dimensions	$\phi260$ x 315 mm	Others	Piezoelectric buzzer and lamp	
Weight	5.4 kg			

ultrasonic waves with a frequency of 40 kHz is memorized in the Holmes, and that involving being repelled by light are memorized in the Lupin. When a number of Holmeses, Lupins, and obstacles exist, it is necessary to determine which is the caught subject. A tactile sensor is installed in the front and rear of the rigid robot body. When these tactile sensors detect a collision with another robot, the robot will stop immediately, will direct its body toward the collision side, and will determine what is the other robot by using the difference between lighting state of the photosensor and that of the LED. When Lupin is caught by Holmes, it will sound its buzzer. Also, Lupin can find its own refuge (hideout) by using its ultrasonic sensor with a frequency of 23 kHz that is installed in its abdominal region. Lupin can escape from Holmes while searching for the hideout, because ultrasonic waves of 23 kHz are generated from the hideout.

As mentioned above, Holmes chases Lupin and Lupin escapes from Holmes based on the behavior they select while generating everchanging sensor information to correspond to the behavior patterns they have memorized.

3.3 Reason and Instinct Network

Satoru-kun is equipped with two kinds of three layer-neural networks called "Reason and Instinct Networks," as shown in Figure 4. The reason network is a short-term memory-type which learns corresponding relationships between behavior patterns and momentary sensor input information. For example, when the photosensor on the head detects light, the "Go Ahead" behavior pattern will be processed in the reason network. On the other hand, the instinct network is a long-term memory type which learns corresponding relationships between behavior pattern series and sensor input information at certain time intervals. For example, the instinct network can process the following
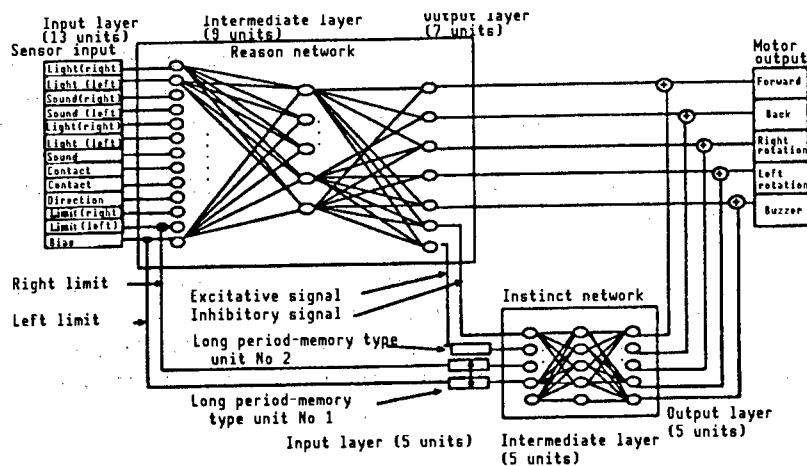
Figure 4. Reason and Instinct Network

series of behavior patterns. "Repeat right rotation and left rotation until the photosensor on the head detects light."

When such a network is used, a certain series of output patterns (now, behavior patterns) can be incorporated inherently within the neural network. In addition, we have introduced the philosophy of long-term memory type units forming a mutually inhabitable combination with long-term memory type units, a network, and have devised a network form which combines the three layer-network through these long-term memory type units. Due to this system, it has become possible to treat a series of output patterns when the "flexibility" of the original hierarchical network is left as it is.

In the above demonstration system, two kinds of behavior pattern series, called "Searching Behavior" and "Escaping Behavior," were handled by using the reason and instinct network. The searching behavior refers to the behavior pattern series in which Satoru-kun looks around for its opponent. On the other hand, the escaping behavior refers to the pattern series in which, when Satoru-kun collides with an obstacle, etc., it will retreat while rotating. As shown in Figure 4, the interval between the output unit of the reason network and the input unit of the instinct network is linked by two kinds of signals, inhibition and excitability, and the switching of the operation of both networks is controlled by inhibitory signals. Excitatory signals output by the reason network are transmitted to the instinct network through the long-term memory type unit No 2, and are turned to triggers for escaping behaviors. In addition, a trigger for searching behaviors has been made by combining limit sensor signals and the input layer unit of the instinct network through the long-term memory type unit No 1 with an inhibiting combination. Searching behaviors are realized when the instinct network learns to generate signals for controlling a motor rotating right of left in accordance with the output of two long-term memory type No 1 units in mutually inhibiting combinations. Also, escaping behaviors are realized when inhibitory signals generated from the reason network are released, excitatory signals are input through the long-term memory type unit No 2 into the instinct network, and the instinct network learns to generate signals for controlling the rotating and backing motor.

106

Satoru-kun is designed to release inhibitory signals generated from the reason network to the instinct network when none of its sensors show any reaction or when only its tactile sensor shows a reaction. In other words when sensor information is abundant, Satoru-kun will take actions on the basis of the reason network, and when it is insufficient, Satoru-kun will take actions on the basis of the instinct network.

Satoru-kun can independently learn the respective reason and instinct networks with high efficiency and high speed, because they consist of a relatively small number of units. The networks converge at about 100 learnings by giving about 50 learning patterns to the reason network and about 10 learning patterns to the instinct network.

Also, the real-time control of Satoru-kun can be realized, because "Forward" processing of the reason and instinct networks can be carried out at a high speed by using an 8-bit microprocessor unit [MPU] made by us and adopted as a brain in Satoru-kun.

4. Conclusion

We have applied a hierarchical network model to the control of a compact locomotive robot, and have demonstrated the validity of the application. In the future, we will carry out applied research on neurocomputers involving the control of locomotive robots equipped with a redundantly large number of sensors and the control of manipulators with a redundant degree of freedom.

References

1.   D.E. Rumelhart and J.L. McClelland, "Parallel Distributed Processing," MIT Press.

Central Nervous System Simulation

43065003c Tokyo JINKO CHINO GAKKAI ZENKOKU TAIKAI (DAINIKAI) RONBUNSHU [PROCEEDINGS OF THE 2ND ANNUAL CONFERENCE OF JSAI 1988] in Japanese Jul 88 pp 131-134

[Article by Maki Adachi of Ichikawa Central Hospital, Tokyo Dental College]

[Text] This paper describes a simulation model of essential parts in the central nervous system for AI research. The system was suggested by the characteristics of the real nervous, neuromuscular and homeostatic control system, such as localization of the functions, automatism, competition in synapse formation, acceleration of the synaptic conduction, down regulation, various feedback loops, etc. The model is composed of three kinds of structures: 1) local structures such as an operation control part, a register and a long-term memory; 2) buses to conduct information; and 3) a network to operate the buses, the long-term memory and the register. This model will be useful in integrating the results of fundamental AI research.

1. Preface

Human intellectual activities are directed by signals based on a neural network. It is said that the number of nerve cells which constitute this neuron network is about 10 billion, and the number of combinations of nerve cells is several thousand. Simulating these nerve cells, assuming that all of these combinations are equivalent, would necessitate a large amount of resources and time. Incidentally, when the aggregation of nerve cells is regarded as a three-structure aggregation consisting of a bus, which transmits the minimum unit of sensation and motion, the devices riding on this bus, and the net which executes the operations on the bus and on each device in accordance with commands from a separate device which executes operations, and when memories are regarded to be held in nerve cells combined in this bus in a slot state, it is unnecessary to simultaneously calculate all combinations and the possibility exists for the simulation to be carried out readily.

This manuscript describes combinations of nerve cells which seem to be capable of realizing some intellectual activities, based on the above idea, and characteristics of nerve cells currently known and their peripheral tissues.

2. Outline of Nervous System and Its Peripheral Tissue

The number of transmitters discharged from nerve endings is increased in synapses among nerve cells by repeatedly exciting these nerve endings for long and short periods of time. Also, the synapses between nerves and muscle cells exhibit the following two phenomena: One is that when a new synapse is formed and a number of axons are competitive, some axons will preferentially form synapses in the order of arrival and other axons will not be able to form any new synapses, while the other is that the number of receptors corresponding to stimulative transmitters increases and decreases in accordance with the decrease and increase in the amount of these stimulative transmitters in the vicinity of the synapses. There is a possibility of the same phenomenon occurring as that mentioned above, even in synapses among nerve cells.

The formation of preferential synapses demonstrates the possibility of the existence of bus structures, and other phenomena show characteristics possessed by individual nerve cells. When general characteristics possessed by living bodies are combined with them, for example, when many regulatory mechanisms forming loops are combined with structures apparently necessary in order to realize cognitive activities, the following hypothetical nervous system can be studied as a model.

3. Entire Structure of Hypothetical Nervous System

As previously mentioned, this model includes three kinds of structures (Figure 1). The first is a bus structure. This bus transmits signals only in one direction, because it consists of nerve cells combined with chemical synapses. The bus has three systems. One is an arithmetic bus which circulates in the order of register, arithmetic unit, long-term memory type unit, and the register, and does not join with any other bus. The bus transmits instructions output from the arithmetic unit, and when the arithmetic unit itself receives such instructions, the bus will construe their signals as operating instructions generated from the outside to the arithmetic unit, and will execute the signals through an arithmetic net. The remaining two systems are sense and motion buses. The former is equivalent to a reflex arc, and goes straight from a sense organ to an effector, and the latter circulates the register and long-term memory unit. In addition, there is a connecting path which branches from the side of the sense organ of the former system, enters the register, joins the latter system, again separates from the latter system, and joins the bus to the effector of the former system. The second is an arithmetic net, which separates from the arithmetic unit and makes the bus, register, cells in the long-term memory unit, and small net (connected to the bus in the same way) perform operations. The third refers to units, i.e., the arithmetic unit, long-term memory unit, and register, as a field in which short-term memory and operations are performed.

In the register, sense signals are stored in sequence as input in the shape of a locally small net, and operations which form the foundation of recollection and cognition are performed between that small net and another

small net formed by signals emitted from the long-term memory unit. When the contents of the small net derived from sense signals and those of the other small net resulting from operations are first determined, they will be transferred to the long-term memory unit to be registered, and when they have been determined previously, they will be transferred to the long-term memory unit for completion.
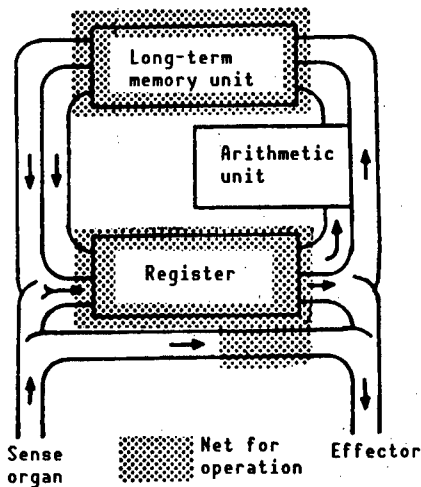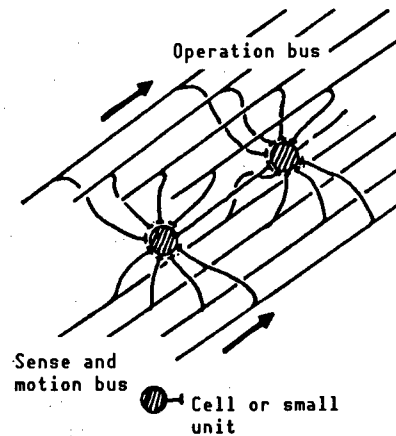

Figure 1.

Figure 2.

The long-term memory unit memorizes signals output from the register and arithmetic unit. It is possible for the long-term memory unit to memorize these signals, similarly to a conditioned reflex, because it can memorize them without distinguishing sense and operation (Figure 2). The long-term memory unit receives input and output instructions through a net for operations, and transfers the contents memorized by the unit to the register.

Instructions output from the arithmetic unit refer to the promotion and inhibition involving the bus, and the excitation and inhibition of the small net, adjustment of threshold, comparison of data on the small net, separation, integration, etc., for the register. Operations are performed by combining them, and the excitation and inhibition of the small net and the adjustment of the threshold are carried out for the long-term memory unit.

The arithmetic unit includes many cells (groups) exhibiting spontaneity (after excitation, when a certain constant time elapses, it will excite by itself without requiring any other stimulation), and involving some basic algorithms. For example, the following matters can be cited as such algorithms. When signals emitted from the sense organ reach the register, they will be sensed and will connect a bus between the register and the long-term memory unit. When the same signals as those emitted from the sense organ are in the long-term memory unit, the small net which holds these signals will be excited by itself, and the past sense signals accompanying the small net and the operation history of the arithmetic unit will be transferred to the register. When the memory of the operation history of the arithmetic unit exists, the past operation history of this

unit will be regenerated, and when it does not exist, a new operation history will be stored in the arithmetic unit or an operation history similar to the new operation history will be searched by lowering the threshold of the long-term memory unit. Spontaneous cells work in such an alternative case, i.e., when the algorithm is in a straight line, spontaneity will be inhibited, and when selection occurs, inhibition will be released, some spontaneous cells will fire, and subsequent algorithms will be executed. This operation history is stored in the long-term memory unit, and when an identical sense input occurs the next time, there is a strong possibility that the processing work will be carried out along with this operation history. The arithmetic unit has some of these algorithms, and they are continuously executed with the excitation of spontaneous cells or signals emitted from outside the arithmetic unit.

4. Characteristics of Small Net

The register and the long-term memory unit have cells which form small nets (Figure 2). There is the possibility of these cells receiving signals from all buses, and the cells possess a characteristic whereby they increase the transmission efficiency of paths in which input has existed and decrease that of other paths. The change in these efficiencies is continued for a short time in the small net of the register, and is continued for a long time in the small net of the long-term memory unit. This phenomenon can be explained by the following philosophy (Figure 3). Assuming that the number of stimulus transmitters per signal of each path (1 to i) from buses is S_1 to S_i, somata convert the total ΣS_i of the number of stimulus transmitters according to the number of signals input within a constant time into the secondary signal SII. At this time, ΣS_i and SII are proportional, and the coefficient is K. When $k \cdot \Sigma S_i$ exceeds threshold T, cells will be excited. At this time, when the difference between $k \cdot \Sigma S_i$ and T is large, K will be changed to reduce the difference. In addition, the only path through which input signals pass at this time increases the number of stimulus transmitters per signal. As a result, cells of the small net react only to the combination of specific stimuli. In addition, these cells can be turned to AND or OR, depending on the order of transmission of the stimuli (Table 1). A bus which transmits signals to the small net, i.e., a mechanism which transmits those in the reverse direction, is required simultaneously with the generation of the small net. This is termed a "reversely small net
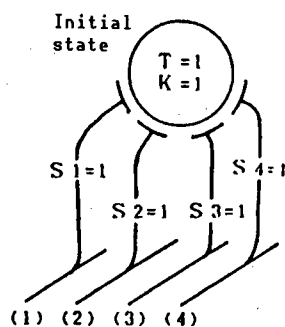

Figure 3.

Table 1. Initial values are S1~4, K = 1, T = 1. S_i, to which signals are transmitted, is increased by 1, and K of excited somata is changed to $T/\Sigma S_i$

Generation of AND

Stimulus	ΣS	SII	S1	S2	S3	S4	State	K
(1.3)	2	2	2	1	2	1	Excitation	.5
(1.3)	4	2	3	1	3	1	Excitation	.25
(1.3)	6	1.5	4	1	4	1	Excitation	.16
(1.3)	8	1.3	5	1	5	1	Excitation	.12
(2.4)	2	.2	5	2	5	2	---	.12
(2.4)	4	.5	5	3	5	3	---	.12
(2.4)	6	.7	5	4	5	4	---	.12

*After stimulus of 1 AND 3, no reaction occurs at 2 AND 4.

Generation of OR

Stimulus	ΣS	SII	S1	S2	S3	S4	State	K
(1)	1	1	2	1	1	1	Excitation	1
(3)	1	1	2	1	2	1	Excitation	1
(1)	2	2	3	1	2	1	Excitation	.5
(3)	2	1	3	1	3	1	Excitation	.5
(3)	3	1.5	3	1	4	1	Excitation	.33
(1)	3	1	4	1	4	1	Excitation	.33
(2)	1	.3	4	2	4	1	---	.33
(4)	1	.3	4	3	4	2	---	.33
(2)	2	.6	4	3	4	2	---	.33
(4)	2	.6	4	3	4	3	---	.33

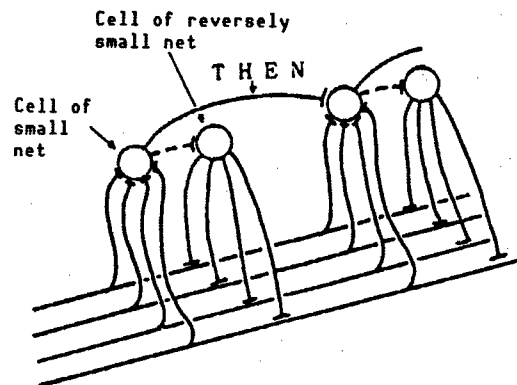*After stimulus of 1 OR 3, no reaction at 2 OR 4.

Figure 4.

(Figure 4). Due to the existence of this reversely small net, it is possible to ride the memory contents on lines. While both small nets are being generated, the arithmetic net inhibits the generation of another small net. Cells of the small net transmit signals to cells of the reversely small net corresponding to the small net, and transmit those to cells of the

next small net. The transmission of the latter is equivalent to THEN (Figure 4).

A delayed-circuit is combined with the final small nets of the long-term memory unit, and when a constant time elapses after the emission of signals, inhibitory signals will be transmitted to other delayed-circuits, and excitatory signals will be transmitted to a couple reversely small nets. When inhibitory signals are transmitted from others during this time, this circuit's activities will stop. This construction is equivalent to NOT, and is used to distinguish between AB and ABC, i.e., NOT AB (Figure 5).
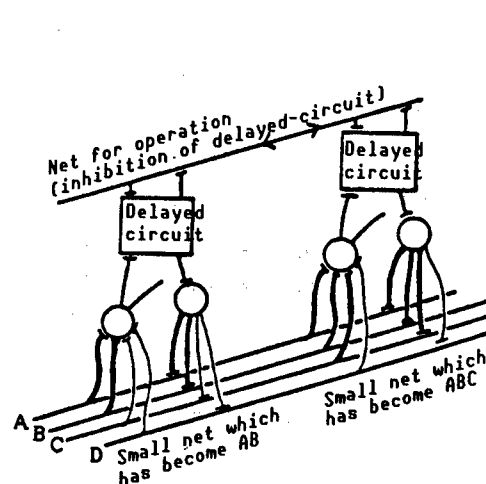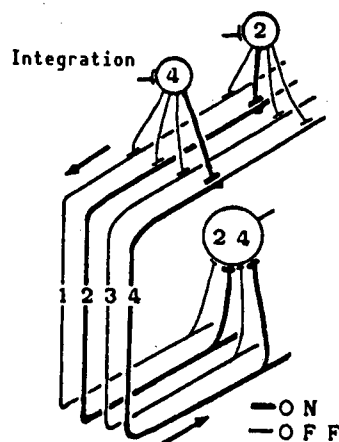

Figure 5.

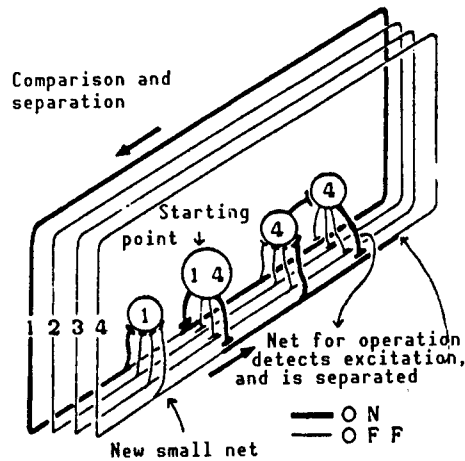* (24) is obtained by integrating (2) and (4)

Figure 6.

5. Operation

All operations executed for other structures by the arithmetic unit are termed "operations" in this manuscript. One such operation controls the threshold of cells of the small net in the long-term memory unit, and enables it to carry out associations. The integration of small nets, as shown in Figure 6, means that buses in the register are excited through memories of reversely small nets of past memories, and new small nets are produced. The comparison and separation of small nets shown in Figure 7 means that a portion of the memories of the small nets becomes a memory of a new small net. Operations for small net couples can be carried out in the same way. These operations are conducted for memories of operations as well as for those of sense and motion. It is thought that cognitive operations, like ratiocination, are formed with such integration, comparison, and separation of memories.

6. Postface

This manuscript covers a portion of the operations and structure of a hypothetical nervous system formed with a partial simulation and an analogy from characteristics of the nervous system and its peripheral tissues. When small nets on the long-term memory unit corresponding to those on the register are searched in this system, signals are transmitted almost

Comparison and separation

Starting point ↓

Net for operation detects excitation, and is separated

New small net

1 2 3 4

━━ O N
── O F F

*(1) is separated by making a comparison between (14) and (4)

Figure 7.

simultaneously to all small nets on the bus. All the small nets process the respective signals, and finally one small net excites a reversely small net and transmits it to the bus. This operation is a kind of parallel processing. This system memorizes the history of operations together with sense information, and carries out operations in accordance with the memory. This fact can bring about the learning of behaviors. In addition, the natural generation of AND and OR can be cited as a concept apparently necessary for research on artificial intelligence. The possibility exists that some such concepts hold naturally with this system. In the future, we are scheduled to explore the simulation of this entire system, as well as details of various structures and operations.

References

1. Ohmura, Shimazu, and Itoh, "Cerebral Structure and Function," Vols 1-2, Igaku-Shoin Co., Ltd., 1985.

Development of New Single-Mode Multiplexer/Demultiplexer

[Article by H. Yanagawa, T. Ochiai, H. Hayakawa, and H. Miyazawa of the Furukawa Electric Company]

[Text] Single-mode wavelength division multiplexers/demultiplexers (M/Ds) have been trial manufactured using a design in which a filter made of multi-layered dielectric film is embedded in a fiber (Filter Embedded Fiber Design) in various configurations (basic type, single-core two-wavelength type, hybrid type with fused taper type, multi-wavelength type, multi-core type, etc.). It was found that optical M/Ds based on this design possess excellent characteristics such as low loss, low crosstalk, temperature stability, and easier development of multi-wavelength and multi-core devices. More specifically, two techniques were used to embed the filters inside the fibers. The first is the filter insertion technique in which filters are inserted into the fibers by slitting the fibers. The second is the filter deposition technique in which fibers with filters deposited directly on the end surfaces are joined together. This resulted in a low insertion loss of about 1 dB for a device with a single-core and two wavelengths. Further, using the hybrid configuration with the fused taper type produced a very high isolation between wavelengths greater than 50 dB, which in turn pro-vided a high degree of crosstalk attenuation for both the near-end and far-end. Moreover, the breadth of the applicability of this design was demon-strated by trially manufacturing optical M/Ds intended for three wavelengths and for five-core tape fiber.

1. Introduction

Optical wavelength multiplex transmission makes it possible to simultaneously transmit multiple pieces of information by passing different optical signals with plural wavelengths through a single optical fiber. The advantages of this arrangement are that:

a. It is possible to increase transmission capacity when similar kinds of information are to be transmitted;

b. It is possible to transmit independently a mixture of different kinds of information (for instance, a mixture of analog and digital information); and

c. It is possible to carry out two-way transmissions.

This technique will make it possible to create optical communication systems and optical sensor systems that are highly economical as well as flexible.

An optical M/D is a key device that combines (multiplexes) and branches (demultiplexes) light beams with different wavelengths in a multiplex wavelength transmission. Various types of M/Ds have been developed to handle multi-mode transmission, and a full-scale experiment using a model system that simulates an optical communication system for subscribers is also in progress.

Optical communication systems and optical sensor systems that use a single-mode optical fiber are rapidly being put into service, and the development of a single-mode M/D that can handle these fibers is awaited earnestly. However, it is not an easy task to achieve low insertion loss and high temperature stability for single-mode optical M/Ds that require highly accurate axis matching. This must be done by using micro-optical parts like those used for multi-mode devices. By adopting a new design in which a filter made of multi-layered dielectric film is embedded within a fiber, we trially manufactured optical fiber M/Ds for single mode, which require fewer parts and are easy to manufacture, and are low cost, low loss and highly reliable. The results of our study on the characteristics of these products will be described below.

2. Comparison of Constitutions of Various Optical M/Ds

In general, optical parts can be classified into three categories:

a. Micro-optical type: Structure that utilizes optical elements such as a micro-lens. These are obtained by miniaturizing bulky conventional optical parts.

b. Fiber type: Structure obtained by directly processing optical fibers.

c. Waveguide type: Structure in which various functions are realized by making optical waveguides on a substrate.

Of these, many of waveguide-type parts are still in the development stage. Thus those that are under consideration for single-mode optical M/Ds are of the micro-optical type (see Figure 1) and the fiber type. Further, the fiber type can be classified into two types, the melt taper type (Figure 2), which makes use of the distributed coupling between the modes for the principle of optical multiplexing/demultiplexing by taking advantage of the characteristics of single-mode fibers, and the filter embedded type (Figure 3) in which a multi-layered dielectric filter is introduced between optical fibers. This will be discussed below.
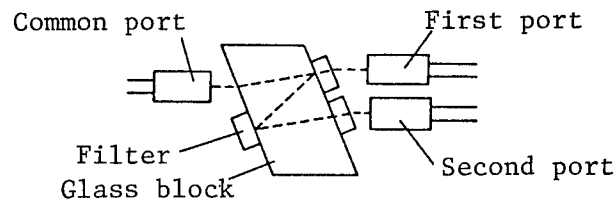
Common port   First port

Filter
Glass block   Second port

Figure 1. Micro-Optical Optical Multiplexer/Demultiplexer

λ_1, λ_2 λ_1

SM fiber λ_2
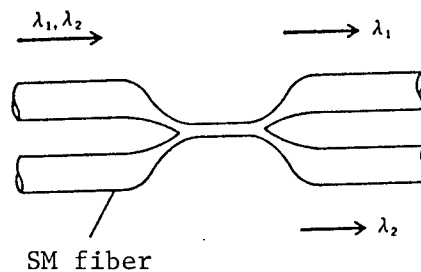
Figure 2. Fused Taper Optical Multiplexer/Demultiplexer

λ_2

Interference filter

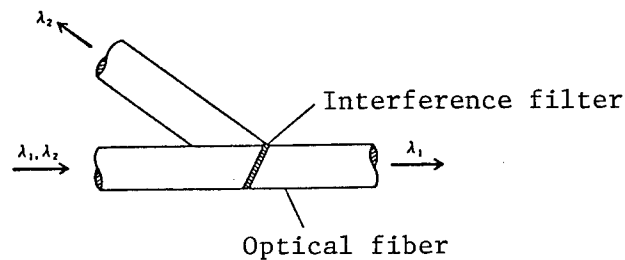λ_1, λ_2 λ_1

Optical fiber

Figure 3. Embedded Filter Optical Multiplier/Demultiplier

In general, an optical M/D must have:

a. A low insertion loss;

b. A low degree of crosstalk (which means that isolation between channels with different wavelengths is high);

c. A pass bandwidth, considering, for instance, that a light source has a wavelength dispersion; and

d. High reliability.

In meeting the requirements for insertion loss and reliability, the fused taper type and the filter embedded type, which use a smaller number of component parts, are advantageous. Meanwhile, with regard to crosstalk and pass bandwidth, the embedded filter type, which makes use of a multi-layered dielectric film filter, and the micro-optical type are superior to the fused taper type, which uses distributed coupling as the underlying principle for

optical multiplexing/demultiplexing. Further, as to productivity, the fused taper and the embedded filter type, which use a smaller number of component parts and are easier to manufacture, appear to offer a lower cost.

Table 1 shows a summary of what has been said above by considering the degree of difficulty in extending a particular type toward multi-wavelength and multi-core devices.

Table 1. Comparison of Various Multiplexers/Demultiplexers

Item	Fused taper	Embedded filter	Micro-optical
Insertion loss	Low	Low	High
Near-end crosstalk	Low	Low	Low
Far-end crosstalk	High	Medium/low	Medium/low
Flatness of pass band	Not good	Good	Good
Temperature range	Wide	Wide	Narrow
Conversion to multi-channel	Hard	Easy	Hard
Conversion to multi-core	Hard	Easy	Hard
Cost	Low	Low	High

3. Embedded Filter Single-Core Optical M/D for Two Wavelengths

3-1 Constitution

The structure and a photograph showing the appearance of a trially manufactured embedded filter single-core optical M/D for two wavelengths are shown in Figure 4 and Figure 5 [not reproduced], respectively.
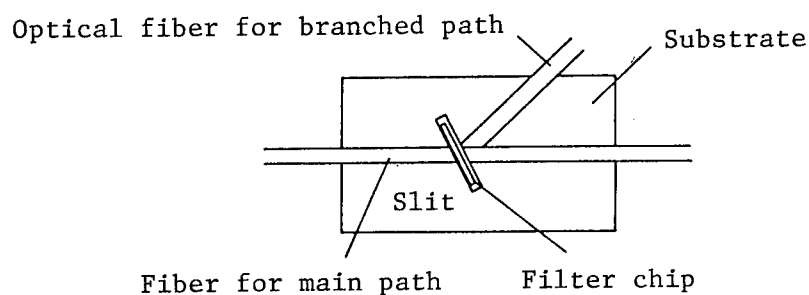

Figure 4. Structure of Single-Core Optical Multiplexer/ Demultiplexer for Two Wavelengths

On a substrate with guide grooves for optical fibers, are placed an optical fiber for the main path and an optical fiber for the branch path with an inclined end face. A filter chip with an evaporated filter made of a multilayered dielectric filter having the desired wavelength selectivity is inserted and fixed to a slit formed at the intersection of the two fibers.

The present trial manufacture run aimed at securing low loss through the use of a single-mode optical fiber as the optical fiber for the main path and an

SI optical fiber with a large core diameter (85 μm) as the optical fiber for the branched path, thereby anticipating use in two-way transmission systems. The branching angle between the main-path optical fiber and the branched-path optical fiber was set at 40°. Further, a filter chip with thickness of 30 μm was incorporated.

3-2 Manufacturing Method

The manufacture of M/Ds consists of the following four processes:

a. Polishing the end face of the optical fiber. The end face of the optical fiber for the branched path is polished to obtain a prescribed angle (40°). Figure 6 [not reproduced] is a photograph of the polished surface.

b. Mounting the optical fibers. The optical fibers for the main and branched paths are mounted on a substrate marked with guide grooves for the optical fibers. The mounting operation is observed through a microscope. The optical fibers are fixed in place using an optical bonding agent (Figure 7).
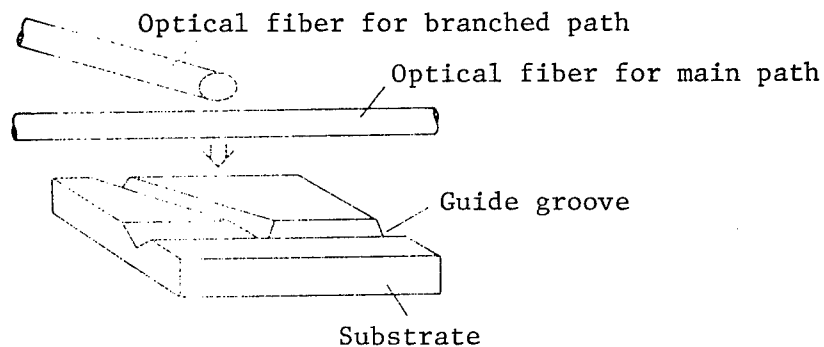
Optical fiber for branched path

Optical fiber for main path

Guide groove

Substrate

Figure 7. Installation of Optical Fibers

c. Formation of a slit. A slit is formed at the intersection of the two optical fibers, which includes the main optical path (Figure 8).
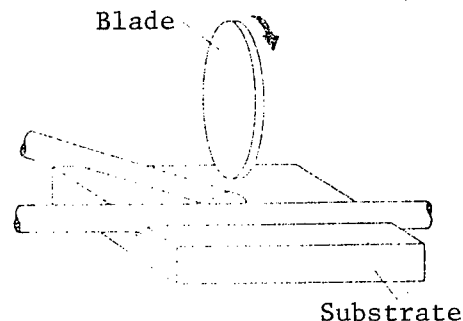
Blade

Substrate

Figure 8. Slit Formation Process

d. Fixing the filter chip. A filter is inserted into the slit and is fixed with an optical bonding agent (Figure 9).
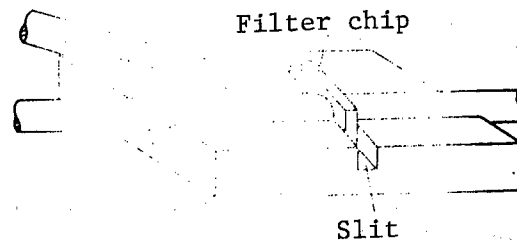
Filter chip

Slit

Figure 9. Filter Chip Insertion Process

As this description indicates, two pieces of the optical fiber for the main path are obtained by separating the original single fiber. Thus there is no need to match the cores of both fibers. In addition, core matching between the optical fibers for the main and branched paths can be drastically simplified because matching their axes can be accomplished by simply installing them in the guide grooves that are precision worked.

3-3 Characteristics

Anticipating two-way transmission systems using the present structures, two kinds of optical M/Ds were produced. These are optical M/Ds using filter chips with center transmission wavelengths of 1.3 and 1.55 μm, intended for use at wavelengths of 1.3 and 1.55 μm.

The wavelength characteristics of the two optical M/Ds are measured by using a white light source and an optical spectral analyzer, which are shown in Figure 10. In addition, the results of point measurement of insertion loss and crosstalk characteristics measured by using a laser diode are shown in Table 2. The insertion loss for single facing was about 1 dB at both 1.3 and 1.55 μm. The near-end crosstalk was less than -40 dB (measurement limit), while the far-end crosstalk was about -25 dB.
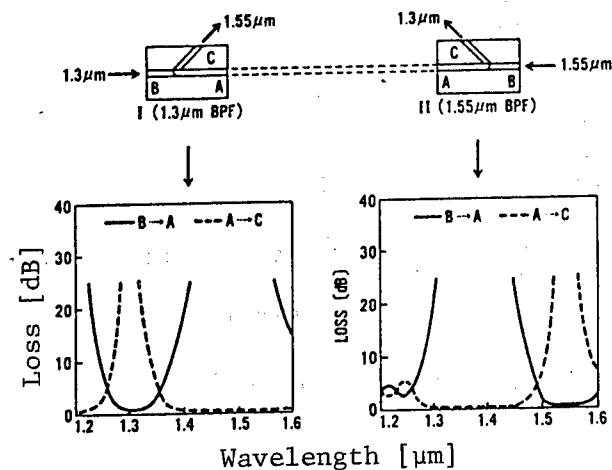
Figure 10. Wavelength Characteristics of Single-Core Optical Multiplexer/Demultiplexer for Two Wavelengths

Table 2. Characteristics of Single-Core Optical Multiplexer/
Demultiplexer for Two Wavelengths

Wavelength	Insertion loss (one facing)	Near-end crosstalk	Far-end crosstalk
1.3 μm	0.96 dB	<-40 dB	-25.6 dB
1.55 μm	1.09 dB	<-40 dB	-28.0 dB

It is thought that insertion loss originates primarily at the gap in the slit and at the gap between the optical fibers for the main and branched paths. Near-end crosstalk should not be present when viewed from purely structural standpoint, but far-end crosstalk is determined by the filter that is being used. Therefore, it should be possible to reduce the amount of crosstalk by improving filter characteristics. As will be described later, it is relatively easy to reduce the amount of crosstalk to about -40 dB. Further, it is thought that the loss-wavelength characteristic shown in Figure 10 corresponds to the sum of losses due to misalignment of the axes and the wavelength characteristic of the optical filter; thus optical M/Ds having wavelength characteristics that correspond to the wavelengths used can be obtained. In this manner, optical M/Ds with the structure described here can be applied in cases where an optical M/D of the fused taper type cannot be used. This is due to the following reasons:

a. By using cut-off filters such as a long wavelength pass filter (LWPF) or a short wavelength pass filter (SWPF), it is possible to deal with systems that utilize light sources such as an LED that have a wide wavelength spectrum.

b. By using a 0.8 μm band SWPF and a 1.3 μm band LWPF, it is possible to deal with systems that use single-mode fibers to multi-mode regions such as 0.8/1.3 μm (Figure 11).
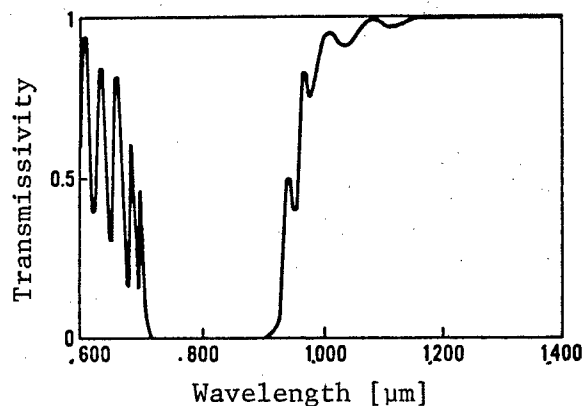

Figure 11. Example of Wavelength Characteristic of LWPF

c. By using a band-pass filter with a narrow pass bandwidth, it is possible to carry out wavelength multiplexing within a single window on a 1.3 μm band or a 1.55 μm band (Figure 12).
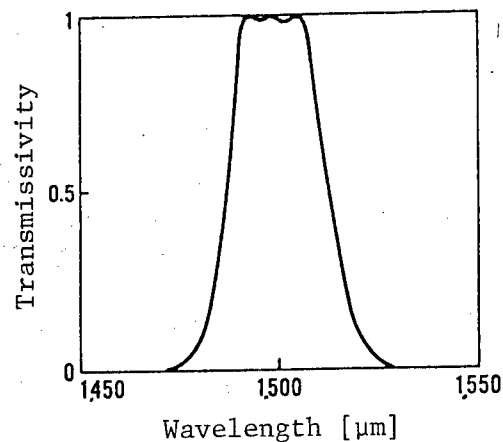

Figure 12. Example of Wavelength Characteristic of Narrow Band Pass Filter

In addition, after evaluating the initial characteristics as described above, various kinds of reliability tests (heat cycle test, wet heat test, and vibration test) were carried out. The heat cycle test was given across a temperature range of -30 to +60°C and an output variation within ±0.1 dB. No residual loss was observed after the test. Further, no output variations in the wet heat test and the vibration test were observed either.

Table 3. Reliability Tests

Type	
Heat cycle	Temperature range: -30 to +60°C Cycle number: 100 cycles (4 cycles/day)
Weat heat	Humidity: 95% RH Temperature: 60°C Time: 100 hr
Vibration	Frequency: 10 → 55 → 10 Hz Cycle: 1 min Amplitude: 1.5 mm Time: 6 hr (2 hr each for 3 directions)

4. Fused Taper Optical Multiplexer/Demultiplexer With Built-in Filter

4-1 Structure

As discussed in Section 2, the fused taper optical M/D has a high level of far-end crosstalk at about -20 dB.

The fused taper optical M/D has a structure which is a hybrid between the fused taper and the embedded filter types in which slits are formed in the optical fibers on the output side of a fused taper, and multi-layered dielectric film filters are inserted and fixed to the slits in order to improve the crosstalk characteristic of the fused taper optical M/D, as shown in Figure 13.
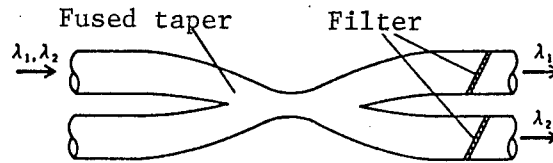

Figure 13.   Fused Taper Optical M/D With Built-in Filter

The wavelength transmissivity characteristic of this optical M/D can be obtained as the product of the characteristic of the fused taper device and the characteristic of the filter, so that unwanted light (crosstalk light) outside the desired wavelength band is greatly reduced, as shown in Figure 14.
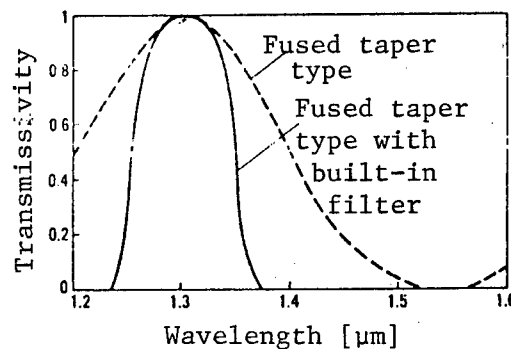

Figure 14.   Wavelength Characteristic of Two Optical M/D

4-2 Characteristics

An optical M/D was constructed by incorporating a 1.3 μm band pass filter with a crosstalk light level of about −40 dB and a 1.55 μm LWPF in a fused taper optical M/D for 1.3/1.55 μm. A photograph showing its appearance is given in Figure 15 [not reproduced]. The size of this device is 8 mm x 9 mm x 75 mm.

The results of the evaluation of pass loss characteristics from ports A and B for both states of fused taper parts only (before insertion of the filters) and for the completed product (after the insertion of the filters) by the use of laser diodes having wavelengths of 1.3 and 1.55 μm are shown in Tables 4 and 5.

Table 4. Pass Loss Characteristic of Fused Taper Part

	1.3 µm	1.55 µm
Port A	0.96 dB	16.8 dB
Port B	22.4 dB	1.11 dB

Table 5. Pass Loss Characteristic of Completed Product

	1.3 µm	1.55 µm
Port A	1.44 dB	58.1 dB
Port B	61.4 dB	1.51 dB

Although the insertion loss increased by about 0.5 dB for both ports A and B as a result of embedding the filters, attenuation of the crosstalk light was improved markedly (by about 40 dB) to be around 60 dB.

5. Optical M/D for Multi-Wavelengths

5-1 Constitution

So far, we have described the optical M/D for two wavelengths. As one example of a practical application, we will now examine a multi-wavelength version of the filter insertion optical M/D. As shown in Figure 16, by increasing the number of optical fibers for branched paths it is possible to develop this device into one usable for multiple wavelengths.
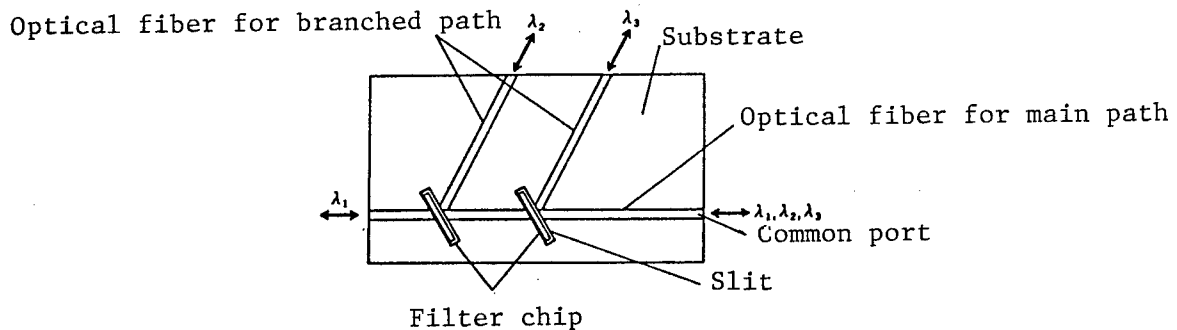

Figure 16. Optical M/D for Three Wavelengths

A three-wavelength M/D (Figure 18 [not reproduced]) was trially manufactured for use in the three-wavelength division multiplex transmission system shown in Figure 17. This system uses wavelengths of 1.2, 1.3 and 1.55 µm. It is expected that lights with 1.2 and 1.3 µm wavelengths will be used for two-way image transmission and that a 1.55 µm light will be used for line monitoring, which makes use of OTDR.

1.3μm O/E 1.55μm OTDR 1.2μm O/E

II III SM FIBER IV SI FIBER

A B

1.2μm E/O I 1.3μm E/O V
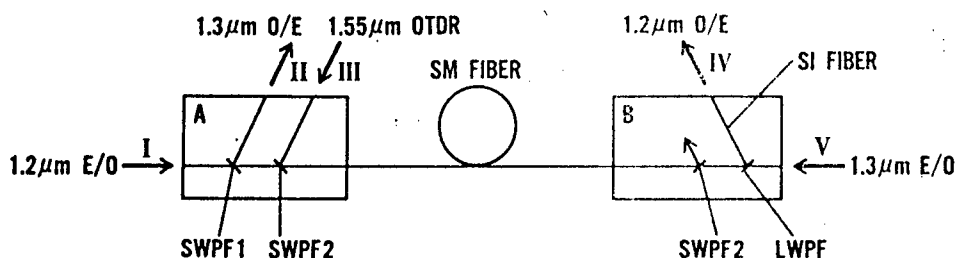
SWPF1 SWPF2 SWPF2 LWPF

Figure 17. Example of Three-Wavelength Multiplex Communication
System

Accordingly, the structure of the optical M/D to be used in this system
employs single-mode optical fibers for the main path (constituting an
incident), common ports and for branched path for port III, and SI optical
fibers with large core diameter (core diameter of 85 μm) for branched paths
for ports II and IV (constituting light-receiving ports). Further, as the
filters for multi-layered dielectric film, three kinds of film were used.
These are SWPFs with cut-off wavelengths of 1.25 and 1.42 μm and an LWPF
with a cut-off wavelength of 1.25 μm.

5-2 Characteristics

The characteristics of insertion loss for single facing and crosstalk in the
trially manufactured three-wavelength optical M/D are shown in Table 6.
Insertion losses were 4.3 dB for light with a wavelength of 1.2 μm, 3.7 dB
for light with a wavelength of 1.3 μm, and 3.1 dB for light with a wavelength
of 1.55 μm. It was possible to limit crosstalk to a value smaller than
-40 dB through the use of filters with improved characteristics.

Table 6. Characteristics of Optical M/D for Three Wavelengths

Wavelength	I	II	III	IV	V
1.2 μm	IN	47.0	65.0	4.3	44.3
1.3 μm	40.2	3.7	41.5	47.8	IN
1.55 μm	71.9	63.4	IN	62.4	52.4

Further, using the trially manufactured three-wavelength optical M/D in the
three-wavelength multiplex transmission system shown in Figure 17 made it
possible to confirm that two-way image transmission and optical line moni-
toring can be accomplished simultaneously and independently. This is
possible thanks to the low crosstalk nature of the optical M/D.

6. Optical M/D for Multi Cores

6-1 Structure

In recent years, the construction of a cable that uses multi-core tape
fibers as fundamental elements has been under examination. Such a cable
would be particularly suited for use in subscribers' optical systems.

125

However, there are few reports available on an optical M/D that is compatible with such multi-core tape fibers. In fact, to the authors' knowledge, there exists just one report, by the present authors, that discusses a multi-core optical M/D. This M/D has a structure in which five sets of optical fibers are arranged on a common substrate and where a filter made of multi-layered dielectric film is embedded at each of the branching points.

The structure and a photograph showing the appearance after packaging of a trially manufactured multi-core single-mode optical M/D--designed to further reduce loss--are shown in Figure 19 and Figure 20 [not reproduced], respectively.
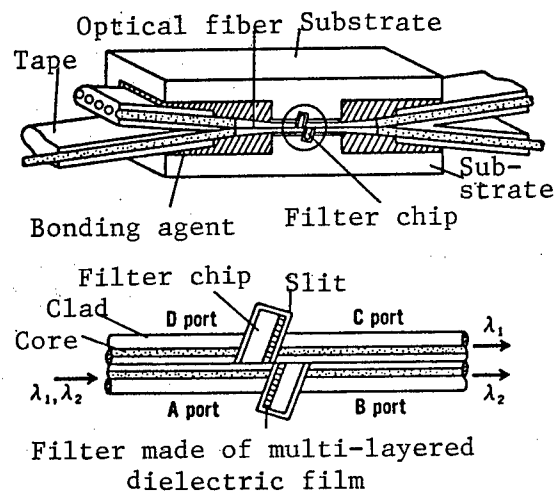

Figure 19. Optical M/D for Multi-Core Use

In this structure, a pair of blocks are formed at the central part of each of the tape fibers, which are fixed to the multi-core guides on a substrate. A filter made of multi-layered dielectric film is embedded into these blocks, and the blocks are axially matched via an engaging pin, and their relative positions are fixed. Therefore, the axis matching within the fiber cross section, which requires a high degree of accuracy, is accomplished by the engagement of the pin so that the alignment process is simplified drastically. Moreover, in this structure, the transmission characteristics and tilt angles of the filters are arranged so that light with a wavelength λ_1 incident upon port A exits from port B by going through a filter chip, and, similarly, light with a wavelength λ_2 incident upon port A is reflected by two filter chips and exits from port C.

6-2 Characteristics

The wavelength characteristics of a five-core optical M/D trially manufactured using a 1.3 μm band pass filter (BPF) is shown in Figure 21. Pass loss in the point wavelength measurements is shown in Table 7.

Table 7. Pass Loss Characteristics of Five-Core Optical M/D [dB]

Wave-length	Fiber Input \ Output	No. 1			No. 2			No. 3			No. 4			No. 5		
		A	B	C	A	B	C	A	B	C	A	B	C	A	B	C
1.3 μm	A		1.26	42.0		1.18	43.7		1.12	43.8		0.97	44.2		1.23	43.8
1.55 μm	A		48.3	1.88		48.2	2.26		49.9	2.00		48.4	2.45		49.4	2.27
1.3 μm	B	1.09		>66	1.27		>66	1.28		>66	1.05		>66	1.19		>66
1.55 μm	C	1.90	>68		2.37	>68		2.00	>68		2.32	>68		2.12	>68	

127
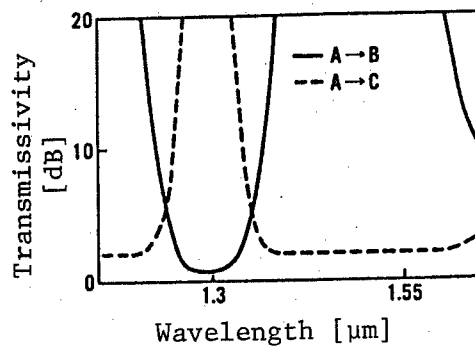
Figure 21. Wavelength Characteristics

The mean loss due to passing light (light with a wavelength of 1.3 μm) is 1.2 dB. The principal factor here is radiation loss at the slits for filter chip insertion. In addition, the mean loss due to the reflection of light (light with a wavelength of 1.55 μm) is 2.2 dB. The principal factors here are radiation loss at the gap between two filter chips and the loss due to axis misalignment. Further, the amount of crosstalk was sufficiently small, with a value less than −42 dB.

7. Evaporated Filter Optical M/D

7-1 Structure

In the filter insertion optical M/D, which has been discussed above, filter chips made by evaporating filters of multi-layered dielectric films on glass substrates are inserted and fixed to slits formed in the optical fibers. Consequently, no core exists at the portion corresponding to the slit with S, and there is generated a radiation loss α, as given by the following equation.

$$\alpha = 10 \log \left[1 + \left(\frac{\lambda S}{2\pi n\omega^2} \right)^2 \right],$$

where λ: wavelength [μm]
     n: refractive index at the gap
     ω: spot size of the fiber [μm]

Thus, for example, if S = 50 μm, then a loss on the order of 0.3 dB is inevitable.

One device designed to reduce radiation loss is an evaporated filter optical M/D. As shown in Figure 22, an unwanted gap is eliminated by directly evaporating a multi-layered dielectric film on the end face of a fiber, which is given an oblique polishing.

7-2 Characteristics

In manufacturing multi-layered dielectric films, use was made of the ion assisted deposition (IAD) technique, which makes it possible to carry out

128

evaporation at low temperatures so as not to affect the covered portion of the optical fiber.
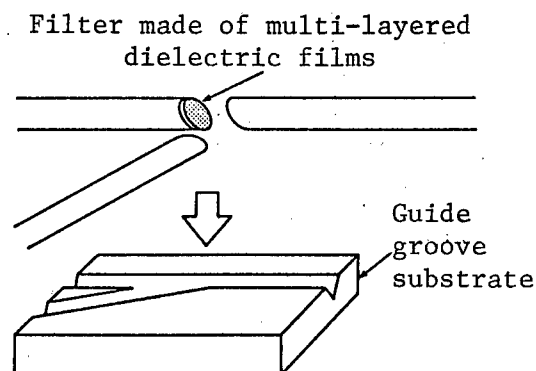

Figure 22.   Filter Evaporation Optical M/D

A loss measurement for point wavelength using a laser diode revealed extremely low losses of 0.52 dB (for light with a wavelength of 1.3 μm) for pass loss and 0.11 dB (for light with a wavelength of 1.55 μm) for reflection loss.   In addition, both near- and far-end crosstalk showed sufficiently low values of -45 dB and -34 dB, respectively.

8.   Conclusion

The trial manufacture of single-mode optical M/D using a new design method in which multi-layered dielectric filters are embedded in the optical fibers showed that:

a.   Optical axis alignment requires less effort and the manufacture of the device is made easier;

b.   The product has low loss;

c.   It has low crosstalk;

d.   It is highly reliable;

e.   It is easy to modify the device to become a multi-wavelength element; and

f.   It is easy to modify the device to become a multi-core element.

In addition, actual trial manufacture of optical M/Ds was carried out using a number of different techniques, including a method of embedding filters in optical fibers, the application of two insertion systems in which filters are inserted and fixed to slits in optical fibers, and an evaporation technique in which filters are evaporated directly onto the tilted surfaces of optical fibers.

END

Foreign Broadcast Information Service (FBIS) and Joint Publications Research Service (JPRS) publications contain political, economic, military, and sociological news, commentary, and other information, as well as scientific and technical data and reports. All information has been obtained from foreign radio and television broadcasts, news agency transmissions, newspapers, books, and periodicals. Items generally are processed from the first or best available source; it should not be inferred that they have been disseminated only in the medium, in the language, or to the area indicated. Items from foreign language sources are translated; those from English-language sources are transcribed, with personal and place names rendered in accordance with FBIS transliteration style.

Headlines, editorial reports, and material enclosed in brackets [ ] are supplied by FBIS/JPRS. Processing indicators such as [Text] or [Excerpts] in the first line of each item indicate how the information was processed from the original. Unfamiliar names rendered phonetically are enclosed in parentheses. Words or names preceded by a question mark and enclosed in parentheses were not clear from the original source but have been supplied as appropriate to the context. Other unattributed parenthetical notes within the body of an item originate with the source. Times within items are as given by the source. Passages in boldface or italics are as published.

SUBSCRIPTION/PROCUREMENT INFORMATION

The FBIS DAILY REPORT contains current news and information and is published Monday through Friday in eight volumes: China, East Europe, Soviet Union, East Asia, Near East & South Asia, Sub-Saharan Africa, Latin America, and West Europe. Supplements to the DAILY REPORTs may also be available periodically and will be distributed to regular DAILY REPORT subscribers. JPRS publications, which include approximately 50 regional, worldwide, and topical reports, generally contain less time-sensitive information and are published periodically.

Current DAILY REPORTs and JPRS publications are listed in *Government Reports Announcements* issued semimonthly by the National Technical Information Service (NTIS), 5285 Port Royal Road, Springfield, Virginia 22161 and the *Monthly Catalog of U.S. Government Publications* issued by the Superintendent of Documents, U.S. Government Printing Office, Washington, D.C. 20402.

The public may subscribe to either hardcover or microfiche versions of the DAILY REPORTs and JPRS publications through NTIS at the above address or by calling (703) 487-4630. Subscription rates will be

provided by NTIS upon request. Subscriptions are available outside the United States from NTIS or appointed foreign dealers. New subscribers should expect a 30-day delay in receipt of the first issue.

U.S. Government offices may obtain subscriptions to the DAILY REPORTs or JPRS publications (hardcover or microfiche) at no charge through their sponsoring organizations. For additional information or assistance, call FBIS, (202) 338-6735,or write to P.O. Box 2604, Washington, D.C. 20013. Department of Defense consumers are required to submit requests through appropriate command validation channels to DIA, RTS-2C, Washington, D.C. 20301. (Telephone: (202) 373-3771, Autovon: 243-3771.)

Back issues or single copies of the DAILY REPORTs and JPRS publications are not available. Both the DAILY REPORTs and the JPRS publications are on file for public reference at the Library of Congress and at many Federal Depository Libraries. Reference copies may also be seen at many public and university libraries throughout the United States.